University of KwaZulu-Natal
College of Agriculture, Engineering and Science
School of Chemistry and Physics

Investigation of IBMQ Quantum Device Hardware Calibration with Markovian Master Equation

A thesis submitted in fulfilment of the academic requirements for the degree of Master of Science (MSc) in the School of Chemistry and Physics, University of KwaZulu-Natal Durban

by Dean Brand
Student Number: 221119787
Supervisors: Prof. Ilya Sinayskiy & Prof. Francesco Petruccione
2022

Author: ..... Date: 13/06/2022

As the candidate's supervisors, we have approved this thesis for submission:

Supervisor: ..... Date: 2022-06-13

Co-supervisor: ..... Date: 2022-06-15

Investigation of IBMQ Quantum Device Hardware Calibration with Markovian Master Equation

Dean Brand

2022

Abstract

In the design of quantum technology, it is crucial to account for the quantum system interacting with its environment to understand the influence of thermal processes and design the devices to avoid effects of relaxation and decoherence of quantum states deteriorating the system beyond use. To accomplish this, a broadening of ideal isolated quantum mechanics is required, namely the theory of open quantum systems. This is most prevalent in the research of quantum error correction, which ensures that the initial quantum state remains intact when it is received and doesn't decay into a different state which would change the information carried by the qubit. To investigate the intersection of all these phenomena, open-access cloud-computing services offer the ideal experimental environment. One such test-bed is offered by IBM in their Quantum Experience platform which allows for remote access to quantum devices. The IBMQ quantum processors, which make use of superconducting qubit technology, are openly accessible through a cloud service. As such, they have been the focus of a lot of research into the evolution of quantum states while interacting with the environment. In the study of open quantum systems, an assumption is often made that the system and environment share no memory of the interaction of individual quantum states, which simplifies the analysis of the system's evolution while also being effectively true for large enough systems. Systems that obey this assumption are known as Markovian. New research has devised methods of error correction and tomography of quantum processors when this assumption no longer holds. Additionally, the calibration of the IBMQ processors performed by IBM to provide hardware parameters is performed through a set of techniques that are not guaranteed to yield cohesive results. These primary factors, among others, give rise to the research discussed in this dissertation, and pose the question of how accurate the hardware calibrations are when compared to results obtained through experiments performed on the devices. Furthermore, the approach uses the theory of open quantum systems to assess the hardware calibration while also testing whether the Markovian assumption of a memoryless system holds for the IBMQ quantum devices. This gives insight into the current state of superconducting quantum computers while providing a possible new avenue for quantum error correction from the perspective of the theory of open quantum systems.

Preface & Acknowledgements

This thesis represents original work by the author and has not otherwise been submitted in any form for any degree or diploma to any tertiary institution. Where use has been made of the work of others it is duly acknowledged in the text.

The work described in this thesis was carried out in the School of Chemistry and Physics, University of KwaZulu-Natal, Westville Campus, Durban, from April 2021 to February 2022, under the supervision of Professor Ilya Sinayskiy and Professor Francesco Petruccione, to whom I express my sincerest gratitude for their consistent help throughout this project. I would like to extend that gratitude to the members of the Quantum Research Group who have also taught me a lot through this research and welcomed me encouragingly to the field of research.

The financial assistance of the National Research Foundation (NRF), The Council for Scientific and Industrial Research (CSIR), and the National Integrated Cyber Infrastructure System (NICIS) towards this research is kindly acknowledged. Opinions expressed and conclusions arrived at, are those of the author and are not necessarily to be attributed to the NRF, CSIR, or NICIS.

I acknowledge the use of IBM Quantum services for this work. The views expressed are those of the author, and do not reflect the official policy or position of IBM or the IBM Quantum team.

Declaration 1 - Plagiarism

I, Dean Brand, declare that

1. The research reported in this thesis, except where otherwise indicated, is my original research.
2. This thesis has not been submitted for any degree or examination at any other university.
3. This thesis does not contain other persons' data, pictures, graphs or other information, unless specifically acknowledged as being sourced from other persons.
4. This thesis does not contain other persons' writing, unless specifically acknowledged as being sourced from other researchers. Where other written sources have been quoted, then:
   (a) Their words have been re-written but the general information attributed to them has been referenced
   (b) Where their exact words have been used, then their writing has been placed in italics and inside quotation marks, and referenced.
5. This thesis does not contain text, graphics or tables copied and pasted from the Internet, unless specifically acknowledged, and the source being detailed in the thesis and in the References sections.

Signed

Author: ..... Date: 13/06/2022

Supervisor: [redacted] Date: 2022-06-13

Co-supervisor: [redacted] Date: 2022-06-15

Declaration 2 - Publications

The work presented in this thesis was the basis for the recent research article submitted for preprint,

- D. Brand, I. Sinayskiy, and F. Petruccione, *Markovian Modelling and Calibration of IBMQ Transmon Qubits*, Feb. 2022, [Online]. Available: http://arxiv.org/abs/2202.04474

Signed

Author: ..... Date: 13/06/2022

Supervisor: .... [redacted] ..... Date: 2022-06-13

Co-supervisor: .... [redacted] .... Date: 2022-06-15

List of Symbols

For the convenience of the reader, this section contains a list of mathematical symbols used throughout the thesis to be used for reference and to improve readability. In certain cases some symbols may be used several times with different meaning, however this confusion should be mitigated by the context in which the symbol is used.

- $|\psi\rangle$ - Quantum state in Dirac notation, known as a *ket*, in this case of an arbitrary wave function ψ.
- $|\cdot|$ - Absolute value/complex conjugate
- σ^i - Pauli operator, for $i = x, y, z, +, -$. Represented by capitalised form, X, Y, Z, in context of quantum gates.
- $\vec{r}$ - Bloch vector.
- U - Unitary operator.
- $\mathbb{I}_n$ - Identity operator of n dimensions.
- H - Hadamard operator.
- $\oplus$ - Tensor sum/addition modulo two.
- $\otimes$ - Tensor/Kronecker product.
- CNOT - Controlled NOT gate, also referred to as CX.
- $|\psi_{xy}\rangle$ - Bell states for combinations of $x, y \in (0, 1)$.
- S - Phase gate/operator.
- R - Rotation gate/operator, with subscripts generally indicating the axis of rotation.
- U_i - Generalised rotation operator for $i = 1, 2, 3$ dimensions/parameters.
- $\mathscr{H}$ - Classical Hamilton function/quantum Hamiltonian.
- t - Time.
- i - Imaginary unit.
- $\hbar$ - Reduced Planck constant.
- e - Euler constant.
- e - Elementary charge.
- V - Voltage.
- I - Current.
- L - Inductance.
- C - Capacitance.
- ω - Angular/qubit frequency.

- E - Energy.
- $a^\dagger, a$ - Creation/annihilation operators, respectively.
- k_B - Boltzmann constant.
- β - Inverse temperature.
- T - Temperature.
- n - Number of dimensions, or number of Cooper Pairs in a system.
- α_q - Anharmonicity.
- J - Inter-qubit coupling strength.
- $\vec{E}$ - Electric field vector.
- $\vec{d}$ - Dipole operator.
- Ω - Dipole field strength.
- ρ - Density operator/matrix.
- $\mathbb{H}$ - Hilbert space.
- e_k - Orthonormal basis elements.
- K_α - Kraus operator.
- $T_\leftarrow$ - Time-ordering operator.
- $\mathscr{L}$ - Liouville/Lindblad operator.
- τ - Time integrand.
- Λ - Dynamical map.
- Π - Eigenspace projector.
- Γ - Emission coefficient.
- $\mathscr{E}$ - Quantum channel.
- γ - Decay rate.
- f - Frequency.
- χ - Coherence function.
- Q - Charge.
- Ω_R - Rabi frequency.
- T_1 - Relaxation time.
- T_2 - Decoherence time.
- T_φ - Dephasing time.
- q_i - Qubit index.

Contents

1 Introduction

Modern computers are increasing in performance rapidly every year, as has been predicted by Moore's Law [1], which observes that the number of transistors in an integrated circuit doubles roughly every two years. This progress necessarily will hit a boundary, as integrated circuits cannot carry on being made more compact indefinitely, and for most practical use the circuits cannot be made much larger without inconvenience to the users. This limit comes firstly in the form of the transistors themselves which have currently been engineered down to the scale of $\sim 5\,\text{nm}$, with 2 nm process architectures on the horizon, and are approaching the size scale of a few atoms, roughly 0.1 nm. At this scale it is impossible to avoid quantum effects which would significantly impact the performance of transistors through processes such as quantum tunneling. This limit is rapidly approaching and this threshold will most likely be reached within the next few decades, which would bring the annual performance increase of computers to an asymptotic halt.

This problem is not, however, of immediate concern. Manufacturers of these processors have many other areas which can be improved upon before the transistor size limit halts their progress, although these areas are a lot harder to improve than just squeezing smaller transistors into a circuit. These problems include aspects such as the efficiency of the communication between the circuit components, the thermal performance, the stability of high clock speeds, and the power efficiency of the chips, especially when designing versions for laptops with increasing performance at a fixed battery capacity.

Nonetheless, this optimisation is approaching the point where these solutions will also be exhausted and the transistor-size bottle-neck problem will bring progress in increased performance to a standstill. Analysis of this problem leads to the natural transition to a quantum based system of computation which would circumvent this problem of classical transistors being impacted by quantum effects, as a natively quantum system would depend on these effects to begin with, and thus take advantage of the quantum realm.

Furthermore, in the study of quantum mechanics, many powerful frameworks and theoretical concepts have been developed since its birth more than 100 years ago. However the numerical evaluation of many of these ideas, such as quantum chemistry of complicated molecules, has proven to be very demanding and in some cases intractable on modern computers. This was the motivation behind the work of Feynman [2] describing the natural approach of using quantum systems to calculate other quantum phenomena, rather than the limited approach of attempting to adapt and project quantum dynamics to digital binary outputs. This further reinforces the need for a paradigm shift in computation, as this forms another ceiling which will eventually be approached by modern computers and requires computational methods which are better suited to the underlying rules of the universe. This brings about the concept of Quantum Computing (QC) which is the field of study and research to rebuild a system of computation based on quantum postulates, similarly to how classical computation was built nearly 100 years ago.

The idea of quantum computers has been around since the time of Feynman's discussions, and since then many algorithms specialised for quantum computing, such as those of Deutsch, Shor, Grover, and many more [3–7]. Many of these quantum algorithms are designed for many-qubit *fault-tolerant* devices, in which the issues of noise and short-scale computations are mitigated allowing for consistent and accurate computation of all quantum algorithms which are conceptualised, while some are less demanding and can be used with the current quantum processing units (QPUs) available today. In more recent research, many of these noisy devices have been designed and constructed, under many different architectures, however they remain relatively small in their computational volume, and remain very susceptible to quantum noise which destroys the states being used in computation. Such devices are said to be Noisy Intermediate Scale Quantum (NISQ) devices [8], and define the current era of the devices available while working towards fault-tolerance.

This issue of quantum noise and calculation errors is a very active field of current research in pursuit of engineering more stability in QPUs, and is the focus of this work which will investigate the decay processes of quantum states used in computation within conventional metrics such as relaxation and decoherence times of controlled states from the perspective of the theory of open quantum systems, along with discussions about the extent of the influence of quantum noise on the computational processes and methods to avoid these problems in future designs.

Before all of this can be discussed, however, it is necessary to introduce all of the background concepts upon which this work is based, for a full picture of the fundamental ideas which are used, as well as a survey of the current state of the literature comprising recent research to show the gap and necessity for the work done in this project. The background and theoretical concepts are the focus of the following sections, which will be followed by the review of current literature.

2 Quantum Computing

The fundamentals of a computer is quite different from the common perception of computers, and is based rather on algorithms and logical processes to deal with binary digits, *bits*, which have a state of being either 0 or 1, and the string of these bits determines how the computational circuits process the information to produce the high level computation most people are familiar with. This provides the easy transition to the quantum formalism with the introduction of *qubits*, which are the quantum states of computation given by

$$|0\rangle = \begin{pmatrix} 1 \\ 0 \end{pmatrix} \qquad \& \qquad |1\rangle = \begin{pmatrix} 0 \\ 1 \end{pmatrix}. \tag{1}$$

This provides the significant advantage that, unlike classical bits, qubits can be in a state other than $|0\rangle$ or $|1\rangle$, through states being in linear combinations (superpositions) of these basis states,

$$|\psi\rangle = \alpha\,|0\rangle + \beta\,|1\rangle\,. \tag{2}$$

Here α and β are complex numbers which are the associated *probability amplitudes* of each state and satisfy the normalisation requirement

$$|\alpha|^2 + |\beta|^2 = 1. \tag{3}$$

This concept of a probability amplitude speaks to the fundamental nature of quantum mechanics in that it is probabilistic: when measuring the final quantum state one can only obtain one of the two basis qubit states, with the probability amplitude $|\alpha|^2$ or $|\beta|^2$ determining how likely the associated basis state is to be measured.

This probability function of the possible outputs of a qubit has a far more significant character than might first be apparent, as it is very unintuitive in that it alters the classical image of, for example, a coin landing on either heads or tails to now being a continuum of states in between these two possibilities until it is observed and the wave function collapses to being one state or the other. This continuous state before measurement is also where the magic of quantum computation happens in that it offers a new realm of possibility making use of strange quantum properties such as entanglement and super-dense coding, both of which will be discussed soon.

Typically, the *computational basis* of $|0\rangle$ and $|1\rangle$ are the eigenstates of the Pauli Z-matrix,

$$\sigma^z = \begin{pmatrix} 1 & 0 \\ 0 & -1 \end{pmatrix}. \tag{4}$$

The other two common bases are the eigenstates of the Pauli X and Y matrices, respectively,

$$\sigma^x = \begin{pmatrix} 0 & 1 \\ 1 & 0 \end{pmatrix} \Longrightarrow \begin{cases} |+\rangle = \frac{1}{\sqrt{2}} \left(|0\rangle + |1\rangle \right) \\ |-\rangle = \frac{1}{\sqrt{2}} \left(|0\rangle - |1\rangle \right) \end{cases} , \tag{5}$$

$$\sigma^y = \begin{pmatrix} 0 & -i \\ i & 0 \end{pmatrix} \Longrightarrow \begin{cases} |+i\rangle = \frac{1}{\sqrt{2}} \left(|0\rangle + i\,|1\rangle \right) \\ |-i\rangle = \frac{1}{\sqrt{2}} \left(|0\rangle - i\,|1\rangle \right) \end{cases} . \tag{6}$$

This representation of bases can be extended to a *Bloch sphere*. Any normalised state can be expressed as

$$|\psi\rangle = \cos\left(\frac{\theta}{2}\right) |0\rangle + e^{i\varphi} \sin\left(\frac{\theta}{2}\right) |1\rangle , \tag{7}$$

where $\theta \in [0, \pi)$ and $\varphi \in [0, 2\pi]$ are the polar and azimuthal angles, respectively. These states can be represented on the surface of a sphere with a radius of $|r|^2 = 1$ and coordinates

$$\vec{r} = (\sin\theta\cos\varphi, \sin\theta\sin\varphi, \cos\theta) , \tag{8}$$

as depicted in Figure 1.

2.1 Gate-based Qubit Operations

Now, with this representation in mind, the Pauli matrices offer additional information. They can be seen as rotations of the quantum state about the respective axis in the sphere by an angle of π. These matrices are therefore the first example of an operator, or *gate*, on a qubit state, which performs the elementary computations and can be used in creating larger algorithms. This also provides insight into the necessary properties of these quantum gates. Mainly, that they must be *unitary*[1], following the definition

$$U^\dagger U = \mathbb{I}_n, \tag{9}$$

where $\mathbb{I}_n$ is the identity operator in n dimensions, which is consistent with the Dirac formalism which has been used thus far. As an example of intuitive representation on the Bloch sphere, the application of two sequential unitary gates is equivalent to rotating the state vector about an axis by π twice which puts it back in the same position as if it were never rotated. This is expressed by $(\sigma^z)^\dagger \sigma^z = \mathbb{I}_2$. In the terminology of quantum gates, the Pauli operators are typically represented as X, Y, Z, rather than the σ-notation which is more often used in the formalism of open quantum systems.

Beyond these three elementary quantum gates, another very useful operator in quantum computing is that of the Hadamard gate,

$$H = \frac{1}{\sqrt{2}} \begin{pmatrix} 1 & 1 \\ 1 & -1 \end{pmatrix} , \tag{10}$$

which is the operator used to create a superposition of states from basis input states. This clearly differentiates it from classical computation logical processes. It can be used to change between the X and Z bases:

$$H\,|0\rangle = \frac{1}{\sqrt{2}} \begin{pmatrix} 1 & 1 \\ 1 & -1 \end{pmatrix} \begin{pmatrix} 1 \\ 0 \end{pmatrix} = \frac{1}{\sqrt{2}} \begin{pmatrix} 1 \\ 1 \end{pmatrix} = |+\rangle \Longrightarrow \begin{cases} HZH = X, \\ HXH = Z. \end{cases} \tag{11}$$

The Hadamard gate creates a superposition of states and allows for effects such as quantum interference to be utilised in algorithms, as well as for the construction of states required for

[1] The operation $A^\dagger$ is the complex conjugate and transpose of an operator A.

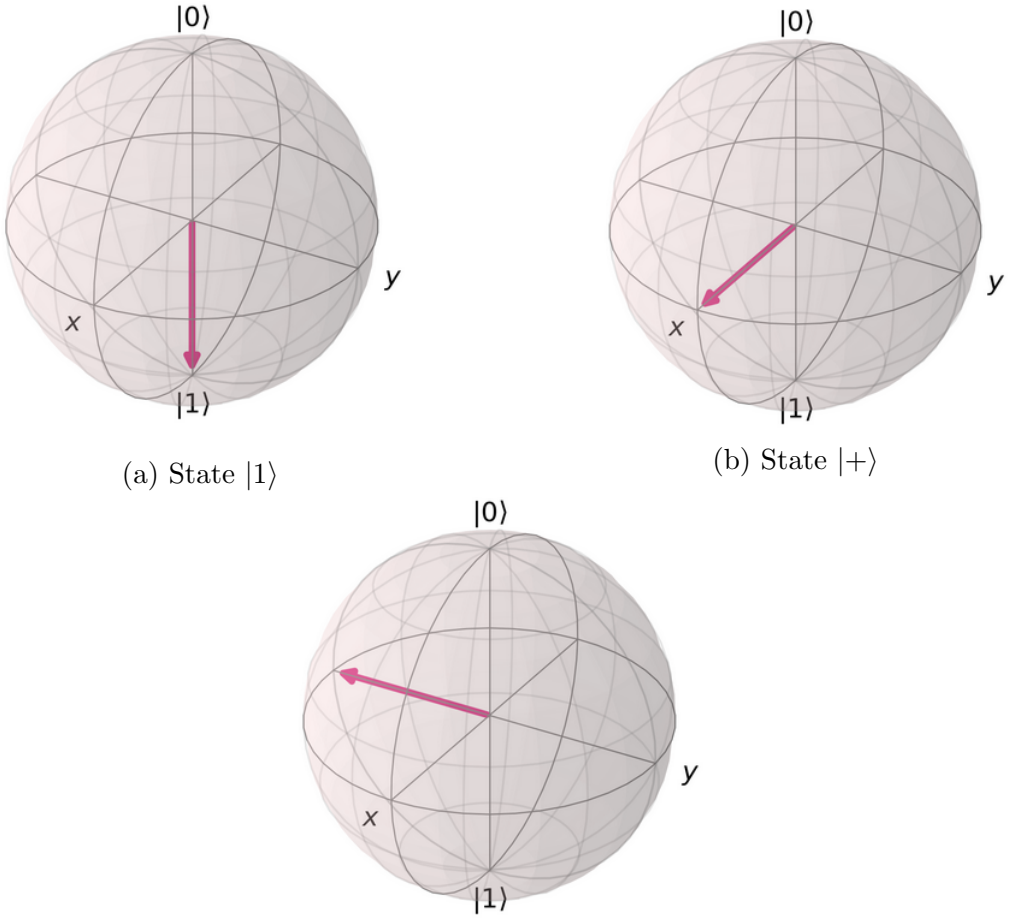

(a) State $|1\rangle$

(b) State $|+\rangle$

(c) State $|-i\rangle$

Figure 1: A Bloch sphere representation of the states $|1\rangle$ (a), $|+\rangle$ (b), and $|-i\rangle$ (c).

entanglement, which in turn are used for faster calculations, cryptography, and quantum teleportation. The collection of these gates, along with many other unitary operators, form the foundation of quantum circuits which are the processes behind the computation. These come into power when moving beyond single-qubit operations, to two-qubit gates. The first of these is analogous to the classical XOR gate,

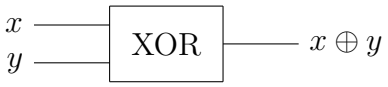

where the notation $\oplus$ means addition modulo two, as the states are in binary. The quantum version of this operation requires the definition of the *tensor product*. This product is defined as

$$|ab\rangle = |a\rangle\,|b\rangle = |a\rangle \otimes |b\rangle = \begin{pmatrix} a_1 \\ a_2 \end{pmatrix} \otimes \begin{pmatrix} b_1 \\ b_2 \end{pmatrix} = \begin{pmatrix} a_1 b_1 & a_1 b_2 \\ a_2 b_1 & a_2 b_2 \end{pmatrix}. \tag{12}$$

The quantum version of the XOR circuit is created through the unitary controlled-not, or CNOT (also called CX in gate terminology), gate. The CNOT gate flips the qubit of the target qubit depending on the value of the control qubit, through an addition modulo two, and is given in matrix form by

$$\text{CNOT} = |00\rangle\langle 00| + |01\rangle\langle 01| + |10\rangle\langle 11| + |11\rangle\langle 10| = \begin{pmatrix} 1 & 0 & 0 & 0 \\ 0 & 1 & 0 & 0 \\ 0 & 0 & 0 & 1 \\ 0 & 0 & 1 & 0 \end{pmatrix}. \tag{13}$$

Its diagrammatic form is

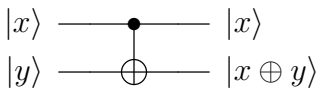

with the dimension of the CNOT operator being attributed to the multipartite quantum states which are formed through the tensor/Kronecker product.

Looking into this a little bit deeper, it can be seen that applying two CNOTs leaves the circuit in its initial state, so the circuit is reversible through a process of un-computation, which is not a commonly used feature in classical computation, due to the abundance of 'garbage bits' which doesn't require the recycling of bits because of the capacity and speed of classical processors, but quantum algorithms can make good use of this feature. This is to be expected due to the unitary nature of quantum gates which are norm-preserving by definition.

An additional quantum feature of the set of operations discussed thus far is *entanglement*. Entanglement is a crucial feature in the power of quantum circuits and is an entirely quantum feature. It is defined as follows: if a pure state $|\psi\rangle_{AB}$ on systems A and B cannot be separated into $|\phi\rangle_A \otimes |\phi\rangle_B$, then the state is entangled. The Bell states are maximally entangled two-qubit states which make up an orthonormal basis

$$\begin{aligned} |\psi_{00}\rangle &= \frac{1}{\sqrt{2}}\left(|00\rangle + |11\rangle\right), & |\psi_{01}\rangle &= \frac{1}{\sqrt{2}}\left(|01\rangle + |10\rangle\right), \\ |\psi_{10}\rangle &= \frac{1}{\sqrt{2}}\left(|00\rangle - |11\rangle\right), & |\psi_{11}\rangle &= \frac{1}{\sqrt{2}}\left(|01\rangle - |10\rangle\right). \end{aligned} \tag{14}$$

These entangled states can be created by using the Hadamard and CNOT gates described before. They have the property that entangled states can have an effect on each other indirectly, typically mediated through *local operations and classical communication* (LOCC). This means that if something happens to one qubit in an entangled pair then the other will also be affected although there is no direct operation on it to do this. This also allows for quantum interference effects to take place which act constructively and destructively to amplify the desired results, if the circuit is designed in the right way. These effects allow for the quantum teleportation of information which is a very unintuitive process in the classical realm.

The final quantum gates worth introducing here are those which perform more general rotations of the Bloch vector. One such gate is the *phase gate*, which applies a rotation about the Z-axis of the Bloch sphere, by an angle of $\pi/2$,

$$S = \begin{pmatrix} 1 & 0 \\ 0 & i \end{pmatrix}. \tag{15}$$

The next rotation gate is more general in its scope of Bloch sphere rotations, as it performs the rotation to any point on the Bloch sphere dependent on the polar and azimuthal parameters, θ and ϕ,

$$R(\theta, \phi) = \begin{pmatrix} \cos\frac{\theta}{2} & -ie^{-i\phi}\sin\frac{\theta}{2} \\ -ie^{i\phi}\sin\frac{\theta}{2} & \cos\frac{\theta}{2} \end{pmatrix}. \tag{16}$$

As this is a more general form of the gate, it can be constrained to rotations about individual axes, as part of the SU(2) group, represented by R_X, R_Y, R_Z, for the respective anchorage,

$$R_\sigma(\theta) = \exp\left(-i\frac{\theta}{2}\sigma\right) \qquad \sigma = X, Y, Z. \tag{17}$$

For example a rotation about the Y-axis is given by

$$R_Y(\theta) = \exp\left(-i\frac{\theta}{2}Y\right) = \begin{pmatrix} \cos\frac{\theta}{2} & -\sin\frac{\theta}{2} \\ \sin\frac{\theta}{2} & \cos\frac{\theta}{2} \end{pmatrix}. \tag{18}$$

All-together these form a set of universal basis gates, specifically the set used by the IBMQ devices, $\left\{CX, \mathbb{I}, R_Z, \sqrt{X}, X\right\}$, which are used to create linear combinations to construct more complex and powerful gates. One such gate is the U_3 gate, which is an extension of the generalised rotation gate (16) to encapsulate all of its variations, which are expressed in the U_2 and U_1 subsets with the subscripts indicating the rotation angles. This generalised rotation gate is represented by

$$U_3\left(\theta, \phi, \lambda\right) = \begin{pmatrix} \cos\frac{\theta}{2} & -e^{i\lambda}\sin\frac{\theta}{2} \\ e^{i\phi}\sin\frac{\theta}{2} & e^{i(\phi+\lambda)}\cos\frac{\theta}{2} \end{pmatrix}, \tag{19}$$

with some example subsets being $U_3(0, -\pi/2, \pi/2) = R_X(\theta)$ and $U_3(\theta, 0, 0) = R_Y(\theta)$.

To actually implement these quantum operations and the gate-based method of quantum computing, standard transistor-based computer technology is obviously not applicable and as such a new approach to hardware is required, as will be discussed in the next section.

3 Hardware Implementation

The gate-based method of quantum computing is almost exclusively based on qubits which are two-level systems (TLS) with quantum properties. These types of systems are ubiquitous in nature and as such there are many adaptations of this property into controlled hardware devices where these systems can be manipulated into quantum gates. The most popular and developed of these qubit implementations include superconducting transmons, electron spins, quantum dots, trapped ions, and ultra-cold atoms. Each of these has their own advantages and drawbacks, however the systems focussed on in this work are superconducting transmon qubits, particularly those used in the IBMQ devices which the experiments were performed on.

3.1 Superconducting Qubits

While many of the other possible quantum systems encode information in their natural properties, such as the two spin states of an electron or photon, superconducting qubits are macroscopic in nature, as opposed to the microscopic size of a particle, and are defined by the lithography of their electronic circuits. This allows for their energy-level spectra to be controlled by the circuit elements which are customisable and can be finely tuned. The qubits are designed to be pseudo-atomic systems, referred to as "artificial atoms," while removing many constraints of working with actual atoms. The dynamics of a superconducting qubit circuit are based on the description of a linear LC resonant circuit, which has oscillating electrical and magnetic energy between the capacitor and inductor, respectively. This is the basis of the ideal quantum harmonic oscillator (QHO) which is to be used as the foundation of superconducting qubits.

To go from a simple LC resonant circuit to a quantum system is an important transformation. The goal is to be able to describe the energy dynamics of the circuit in a quantum mechanical framework, which requires the Hamiltonian description of both systems to bridge the gap. The dynamics of a quantum system are described by the time-dependent Schrödinger equation,

$$\mathscr{H}\left|\psi(t)\right\rangle = i\hbar\frac{\partial}{\partial t}\left|\psi(t)\right\rangle \Longrightarrow \left|\psi(t)\right\rangle = e^{-i\mathscr{H}t/\hbar}\left|\psi(0)\right\rangle, \tag{20}$$

for the quantum state $|\psi\rangle$ at a time t. The Hamiltonian $\mathscr{H}$ is the quantum operator which describes the total energy of the system, analogously to its classical counterpart, which needs

to be recast into the quantum operator formalism. For the LC circuit, the important quantities which need to be extracted are the voltage and current, through the relations

$$V = L\frac{\mathrm{d}I}{\mathrm{d}t} \qquad \& \qquad I = C\frac{\mathrm{d}V}{\mathrm{d}t}. \tag{21}$$

After some manipulation, this can be cast into Lagrangian form and thereby into the classical[2] Hamiltonian form of a classical harmonic oscillator (CHO),

$$\mathscr{H} = \frac{1}{2}CV^2 + \frac{1}{2}LI^2. \tag{22}$$

Some further generalisation is required in the full definition of the QHO from the LC circuit, but those details will be omitted here as they are described in other sources [9, 10]. This description can fortunately be easily adapted to the superconducting case where the dynamics are more complicated, which proves another advantage of the LC circuit model. The Hamiltonian in Equation (22) is equivalent to the 1D harmonic oscillator, and so is part of an eigenvalue problem, $\mathscr{H}\left|\psi\right\rangle = E\left|\psi\right\rangle$, with well known solutions. The solution is a sum of eigenstates with equidistant energy levels spaced in units of $\hbar\omega_r$ with

$$\omega_r = \frac{1}{\hbar}\sqrt{8E_L E_C} = \frac{1}{\sqrt{LC}}$$

being the resonant frequency of the quantum system. This solution lends itself to the compact representation of a QHO which represents the transitions between energy states with creation and annihilation operators, $a^\dagger$ and a respectively, to give the simplified Hamiltonian of

$$\mathscr{H} = \hbar\omega_r\left(a^\dagger a + \frac{1}{2}\right). \tag{23}$$

Before proceeding, it should be noted that for the rest of this work natural units will be used, such that $\hbar = k_B = 1$ which will suppress the constants, unless explicitly used. This also means that frequency, ω, and temperature, $\beta = 1/T$, will be treated as measures of energy. The natural appeal of the circuits to be made with superconducting materials is the idea of there not being electrical resistance, which would not be a problem for classical electronics but is a significant source of noise which would destroy the coherence of the quantum state long before it could be used. In superconductors, the electrical resistance decreases while the electrons form *Cooper Pairs* (CPs). These CPs are then bound and require more energy to separate which is no longer available at the low temperatures required for superconductivity. This phenomenon can then be used in the circuit, known as a Cooper Pair Box, which consists of a superconducting island either possessing an extra Cooper pair, with charge $2e^-$, or with no extra CP. These two states defined by the presence of a CP form the TLS of a quantum system with the presence of an extra CP representing $|0\rangle$ and the absence representing $|1\rangle$. These states can thus be controlled by applying different voltages to tunnel junctions in the circuit which can execute the basis gate instructions required for quantum computing.

Additionally, CP Boxes have other disadvantages which are fairly common to quantum computers, namely that of quantum noise. They are especially sensitive to noise induced by nearby charges which generate their own electromagnetic fields that can influence the CP of interest. It is now worth mentioning that the prohibiting factor in many other atomic systems being used as qubits is the fact that they are not exclusively two level quantum systems. Rather, they have

[2]The concept of the Hamiltonian is shared between classical and quantum mechanics, however being constructed in the quantum operator formalism. For the rest of this work the quantum form will be used exclusively, so there is no need to differentiate between the notations.

many higher energy discrete states, which are separated in units of $\hbar\omega$. This kind of system can be morphed into a TLS by isolating and controlling just two of these levels, but generally still come with other disadvantages. The CP Box inherits this problem from the fact that the QHO system upon which it is based is naturally a linear system which has equidistant energy levels. It lacks the required anharmonicity between the quantum states which allow for the correct transitions to be driven without exciting the wrong energy levels in the system. The obvious solution is to add anharmonicity to the system to separate the energy levels into easily addressable states, however this is not a trivial task. One example of the impracticality is that having greater anharmonicity, while making it easier to address individual states, limits the size of allowed drive pulses which are used to execute quantum gates, as discussed in more depth in [9].

To introduce the desired anharmonicity in the system developed so far, a new circuit element is introduced — the Josephson junction. It is a non-linear circuit element which has no dissipation. This junction replaces the linear inductor of the QHO system, as it performs the same task but with a dependence on the superconducting phase, ϕ. The system Hamiltonian then becomes

$$\mathscr{H} = 4E_C n^2 - E_J \cos(\phi), \tag{24}$$

where E_C is the charging energy, $n = Q/2\mathrm{e}$ is the charge number, and E_J is the Josephson energy. This expression gives rise to a new ratio of interest, E_J/E_C, which reflects the system dynamics and is used to infer more properties of the system. This inductor replacement changes the energy spectrum from being a quadratic form having equidistant energy levels, to a sinusoidal form with uniquely addressable energy levels, as depicted in Figure 2.

3.2 Transmon Qubits

The current regime of superconducting quantum computers favour circuit designs with $E_J \gg E_C$, as in the opposite case, where $E_J \leq E_C$, the issue of charge noise remains a significant disadvantage as with the CP Box, and the system is also more sensitive to changes in the Hamiltonian of the circuit. To solve the charge-noise sensitivity problem, the effective TLS isolation concept can be made use of, and approach the ideal $E_J \gg E_C$ state, a new kind of superconducting qubit was created. The *transmon* (transmission-line shunted plasma oscillation) qubit sacrifices some of the anharmonicity of the transition frequencies between quantum states, so that the charge noise of CPs can be mitigated while maintaining the TLS structure. This becomes possible as the charge dispersion decreases exponentially in E_J/E_C while the anharmonicity decreases only algebraically in a weak power law. This disparity in the growth rates of these quantities means that at a high enough ratio of E_J/E_C, the anharmonicity between states is mostly maintained while effectively removing all charge noise and improving scalability of the system to large numbers of qubits. The actual value of this ratio in a particular device depends on the design and implementation of the circuit, so charge noise is typically a persistent problem, added to by the fragile nature of quantum states in general which prevents perfect devices, however the outcome is still vastly improved with the transmon qubit approach. Now that an effective TLS is available, the anharmonicity can be concretely defined. For using the two lowest energy states as the TLS, the anharmonicity of the system is defined as

$$\alpha_q = \omega_q^{0\to1} - \omega_q^{1\to2}, \tag{25}$$

which, by virtue of the cosinusoidal energy spectrum, is a negative value as the energy level difference grows with increasing levels. For the case of IBMQ devices, the average anharmonicity is roughly between 5 and 10 % of the average qubit frequency. Another benefit of the transmon is that the superconducting phase, ϕ, has small fluctuations making it a good quantum number

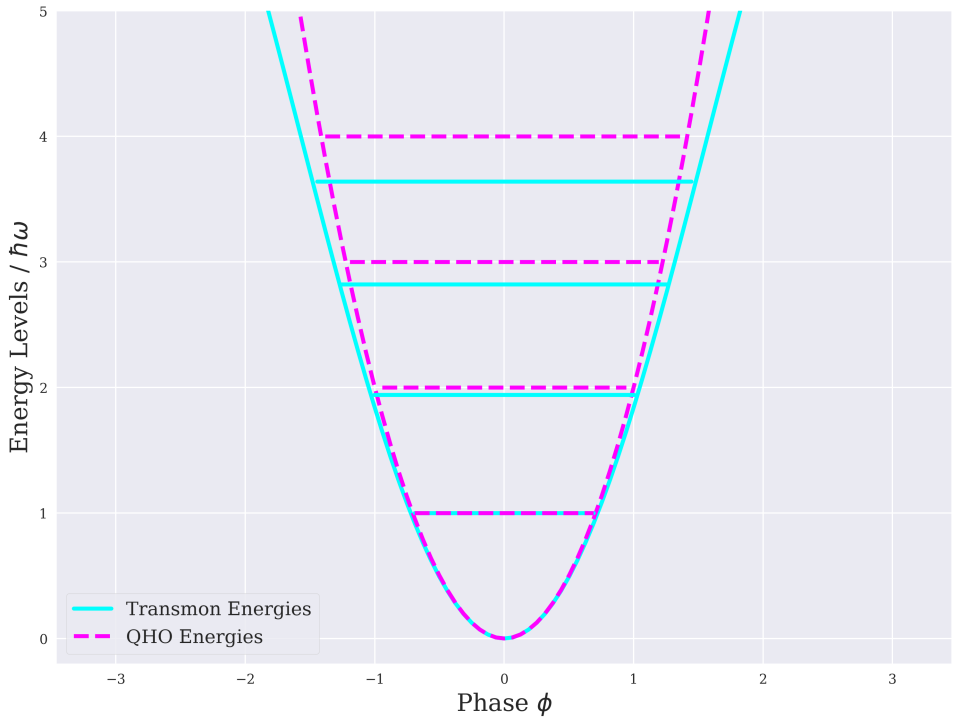

Figure 2: Energy level diagram depicting the difference in distances between the quantum states for the linear QHO inductor and the non-linear transmon qubit circuit.

and allowing for a good power series representation of the Josephson energy term in (24). For small ϕ,

$$E_J \cos(\phi) = \frac{1}{2}E_J\phi^2 - \frac{1}{24}E_J\phi^4 + \mathcal{O}(\phi^6), \tag{26}$$

where the newly introduced anharmonicity clearly comes into the picture from the second term, and confirming that the anharmonicity is a negative quantity. The eigenbases of the QHO in (23), and the continued formalism of second quantisation, allow for the representation of the system Hamiltonian as

$$\mathscr{H} = \omega_q a^\dagger a + \frac{\alpha_q}{2}\left(a^\dagger a^\dagger a a\right), \tag{27}$$

which has the form of a Duffing oscillator [11] representing a weakly anharmonic quantum oscillator (AHO) for small enough α. It should be noted that higher energy levels are still accessible despite the structure of the transmon system, however they are much more difficult to accidentally drive and this is reinforced by error correction and precise quantum control techniques in the driving process of gate execution. With all of these systems in place the TLS form is almost guaranteed and the Hamiltonian can be simplified once more to be

$$\mathscr{H} = \omega_q \frac{\sigma^z}{2} = \frac{\omega_q}{2}\begin{pmatrix} 1 & 0 \\ 0 & -1 \end{pmatrix}. \tag{28}$$

Unfortunately, single-qubits do not make for very good quantum computers, and so the system needs to be expanded some more. Looking at the two-qubit case, for example, the dimensionality of the Hilbert space needs to be extended, such that the Pauli Z operators in the Hamiltonian become

$$\sigma_1^z = \sigma^z \otimes \mathbb{I}_2 \qquad \& \qquad \sigma_2^z = \mathbb{I}_2 \otimes \sigma^z, \tag{29}$$

for qubits 1 and 2, respectively, and where $\mathbb{I}_2$ is the 2×2 identity matrix. In addition to there now being more than one qubit in the Hamiltonian, in order to create entanglement and execute multi-qubit gates, the Hamiltonian needs an interaction component to connect degrees of freedom in the individual qubits. This connection manifests itself in some physical coupling mechanism in the quantum device which generates an interaction term in the Hamiltonian.

There are many ways to achieve this and it comes down to qubit design and the choice of circuit components, the details of which are described in the following sources: [9–13]. For the intent of this discussion, the coupling feature is expressed as the effective qubit-qubit "flip-flop" interaction: if one coupled qubit undergoes a state transition, the other coupled qubit does as well. This is realised by the combination of Pauli raising and lowering operators,

$$\sigma^{\pm} = \frac{1}{2}\left(\sigma^x \mp i\sigma^y\right). \tag{30}$$

which have the effect of raising the state $|0\rangle$ to $|1\rangle$ or lowering $|1\rangle$ to $|0\rangle$. This connection is scaled by the coupling strength J between them. So, for the 2-qubit case, the system Hamiltonian becomes

$$\mathscr{H} = \frac{\omega_1}{2}\sigma_1^z + \frac{\omega_2}{2}\sigma_2^z + J\left(\sigma_1^+\sigma_2^- + \sigma_1^-\sigma_2^+\right). \tag{31}$$

The extension from 2 qubits to more is simpler than the extension from 1 qubit to 2. In moving to larger systems, the same process of including a frequency dependent term for each new qubit is followed, however noting that the Hilbert space must be increased accordingly, such that for 3 qubits the Pauli operators are expressed as follows,

$$\begin{aligned} \sigma_1^z &= \sigma^z \otimes \mathbb{I}_2 \otimes \mathbb{I}_2, \\ \sigma_2^z &= \mathbb{I}_2 \otimes \sigma^z \otimes \mathbb{I}_2, \\ \sigma_3^z &= \mathbb{I}_2 \otimes \mathbb{I}_2 \otimes \sigma^z. \end{aligned} \tag{32}$$

This pattern is repeated for larger systems, with the index of the qubit being operated on matching the position in the queue of factors in the tensor products. Additionally, the coupling between each pair needs to be accounted for. This part depends on the layout of the qubits in the device, and as such does not have a general form. For example, in a linear layout of 3 qubits, there would be two coupling terms which have similar operators, and different coupling strengths. For a more complicated layout, there may be some qubits which have multiple couplings. The 3-qubit Hamiltonian for a linear layout would, for example, become

$$\mathscr{H} = \frac{\omega_1}{2}\sigma_1^z + \frac{\omega_2}{2}\sigma_2^z + \frac{\omega_3}{2}\sigma_3^z + J_{1,2}\left(\sigma_1^+\sigma_2^- + \sigma_1^-\sigma_2^+\right) + J_{2,3}\left(\sigma_2^+\sigma_3^- + \sigma_2^-\sigma_3^+\right). \tag{33}$$

3.3 Qubit Drive and Control

To complete the discussion about the hardware implementation of a quantum computer, the single-qubit case will be focussed on to describe the process of executing quantum gates through *qubit drive*, and how exactly the quantum states are controlled and altered. From the simplified Hamiltonian of (28), a classical microwave driving electric field can be applied,

$$\vec{E}(t) = \vec{E}_0 e^{-i\omega_d t} + \vec{E}_0^* e^{i\omega_d t}, \tag{34}$$

which describes a dipole interaction between the microwave EM field and the qubit. The total system Hamiltonian then becomes a sum of these two operators,

$$\mathscr{H} = \mathscr{H}_0 + \mathscr{H}_d. \tag{35}$$

The motivation behind driving the qubit with an external electromagnetic field is to apply the raising and lowering Pauli operators from (30), which allow for the definition of the dipole operator

$$\vec{d} = \vec{d}_0\sigma^+ + \vec{d}_0^*\sigma^-. \tag{36}$$

This operator then forms the drive Hamiltonian with the electric field as

$$\begin{aligned}\mathscr{H}_d &= \vec{d}\cdot\vec{E}(t) \\ &= \left(\vec{d}_0\cdot\vec{E}_0e^{-i\omega_dt} + \vec{d}_0\cdot\vec{E}_0^*e^{i\omega_dt}\right)\sigma^+ - \left(\vec{d}_0^*\cdot\vec{E}_0e^{-i\omega_dt} + \vec{d}_0^*\cdot\vec{E}_0^*e^{i\omega_dt}\right)\sigma^- \\ &= \left(\Omega e^{-i\omega_dt} + \tilde{\Omega}e^{i\omega_dt}\right)\sigma^+ + \left(\tilde{\Omega}^*e^{-i\omega_dt} + \Omega^*e^{i\omega_dt}\right)\sigma^-\end{aligned} \tag{37}$$

where $\Omega = \vec{d}_0\cdot\vec{E}_0$ and $\tilde{\Omega} = \vec{d}_0\cdot\vec{E}_0^*$ have been introduced. Moving to the interaction picture, where $\mathscr{H}_{d,I} = U\mathscr{H}_dU^\dagger$, the unitary evolution is described by

$$U = e^{i\mathscr{H}_0t} = e^{-i\omega_q\sigma^zt/2} = \cos(\omega_qt/2)\,\mathbb{I}_2 - i\sin(\omega_qt/2)\,\sigma^z, \tag{38}$$

while noting that its effect on the Pauli operators can be described as

$$\begin{aligned}U\sigma^\pm U^\dagger &= \left[\cos(\omega_qt/2)\,\mathbb{I}_2 - i\sin(\omega_qt/2)\,\sigma^z\right]\sigma^\pm\left[\cos(\omega_qt/2)\,\mathbb{I}_2 + i\sin(\omega_qt/2)\,\sigma^z\right] \\ &= \sigma^\pm\left(\cos(\omega_qt) \pm i\sin(\omega_qt)\right) = e^{\pm i\omega_qt}\sigma^\pm\end{aligned} \tag{39}$$

where most of the algebra has been skipped, so as to not distract from the present discussion, but can be found elsewhere [14]. Evaluating this interaction picture Hamiltonian gives

$$\mathscr{H}_{d,I} = U\mathscr{H}_dU^\dagger = \left(\Omega e^{i\Delta_qt} + \tilde{\Omega}e^{i(\omega_q+\omega_d)t}\right)\sigma^+ + \left(\tilde{\Omega}^*e^{-i(\omega_q+\omega_d)t} + \Omega^*e^{-i\Delta_qt}\right)\sigma^-, \tag{40}$$

where

$$\Delta_q = \omega_q - \omega_d \tag{41}$$

is the difference between the qubit and driving frequencies, and is typically smaller than the sum of the frequencies. This difference allows for the rotating-wave approximation (RWA), which can be made since the sum of frequencies in the exponentials oscillates much faster than Δ_q and thereby average out to zero contribution so those terms can be dropped from the Hamiltonian, leaving

$$\mathscr{H}_{d,I,\mathrm{RWA}} = \Omega e^{i\Delta_qt}\sigma^+ + \Omega^*e^{-i\Delta_qt}\sigma^-. \tag{42}$$

Switching back to the Schrödinger picture the drive Hamiltonian becomes

$$\mathscr{H}_{d,\mathrm{RWA}} = U^\dagger\mathscr{H}_{d,I}U = \Omega e^{-i\omega_dt}\sigma^+ + \Omega^*e^{i\omega_dt}\sigma^-, \tag{43}$$

and the full system Hamiltonian is

$$\mathscr{H}_{\mathrm{RWA}} = \frac{\omega_q}{2}\sigma^z + \Omega e^{-i\omega_dt}\sigma^+ + \Omega^*e^{i\omega_dt}\sigma^-. \tag{44}$$

More insight can be gained from viewing this quantity in the actual drive frame, rather than the frame of the system. To change frames, the transformation $U_D = e^{-i\omega_d\sigma^zt/2}$ is used, such that the drive-frame Hamiltonian becomes[3]

[3] Assuming that the drive strength is a real value, $\Omega = \Omega^*$.

$$\begin{aligned}\mathscr{H}_D &= U_D \mathscr{H}_{\text{RWA}} U_D^\dagger - iU_D \left(\frac{\mathrm{d}U_D}{\mathrm{d}t}\right)^\dagger \\ &= \frac{\Delta_q}{2}\sigma^z + \Omega\sigma^x.\end{aligned} \tag{45}$$

From this frame it is evident that on resonance, $\Delta_q = 0$, the drive induces an X rotation on the Bloch sphere, with a drive strength of Ω. For an off-resonant drive additional Z rotations are contributed to giving rise to Ramsey oscillations which can be measured to gain insight into how well the device is performing, as will be demonstrated in a later section.

The discussion thus far, despite encapsulating a lot of real-world considerations which influence the capabilities and usage of quantum computers, has been predominantly focussed on the ideal case of isolated quantum systems undergoing simple unitary evolution. This, however, is the perfectly ideal case which is never attainable in practice. In real quantum devices, there are many more degrees of freedom which need to be accounted for, especially considering the fragile nature of quantum states. While some mention of noise has been included when talking about the design of superconducting circuits, the true presence of quantum noise is a significantly larger issue which needs careful treatment to avoid. This inclusion of noise falls under the theory of open quantum systems, where the quantum states which are being manipulated are part of a larger environment with which it interacts. This will be the topic of discussion for the following section.

4 Open Quantum Systems

Although the description of quantum dynamics has thus far been set in the framework of isolated systems, the reality is never fully described by these models as no quantum system can be completely isolated from the surrounding external environment. This is particularly significant in the case of quantum computers as there is a very high frequency of interactions with the quantum states in order to perform calculations, in addition to the hardware being very difficult to design in a way which fully isolates only the desired quantum states due to the impracticality of localising them. For example, the process of quantum tunnelling or vacuum field fluctuations are impossible to avoid in a device, so there needs to be an extension to the description of quantum dynamics in a system which interacts with its environment. This extension is the theory of open quantum systems (OQS). The more realistic quantum properties described in this extended theory will give far more insight into what actually happens while a calculation through a series of gates is being executed, and why NISQ devices are not yet at the stage of the ideal quantum computers which can perform algorithms considered to be classically intractable.

In classical computers, for example, there are well defined paths within the electronics for the electrons to travel and be used in calculation with very little error, while also having ubiquitous transistors to use redundancy in correcting any errors which might appear along with specialised algorithms, such as Error Correcting Codes (ECC), to account for any computation errors which may occur. This system is very well segregated to keep the computation particles separate from disruptions within the hardware, which is a stark contrast to quantum systems. The particles present in the hardware, be it through the present electromagnetic fields, vacuum quantum fields, or just the atoms which constitute the electronics, are naturally on equal footing with the qubits which need to be used. As such there are myriad degrees of freedom with which the qubits can interact during the process of calculation.

4.1 Density Operator Formalism

To discuss the level of this unwanted interaction which essentially destroys the quantum state of interest, the density matrix representation is introduced. While individual isolated quantum

states can be represented as a linear combination of basis states and normalised probability amplitudes, as in (2), larger quantum states are represented by statistical mixtures of these states. These statistical mixtures are mathematically represented by density operators, which follow from the use of pure quantum states, $|\psi\rangle$, to construct projection operators, $|\psi\rangle\langle\psi|$. The operators admit convex sums which act as an extension of the eigenbasis decomposition of (2) in that they have normalised probability amplitude sums. These operators naturally then form the foundation for the desired statistical mixtures as they can represent the internal dynamics between quantum states all while maintaining normalisation. Within this framework, a hermitian density operator can be decomposed into the projection operators as follows,

$$\rho = \sum_i p_i \left|\psi_i\right\rangle\!\left\langle\psi_i\right|, \tag{46}$$

with p_i providing a probability distribution as $p_i > 0$ and $\sum_i p_i = 1$. The physicality condition of the density operator is ensured by the fact that it has real non-negative eigenvalues, $\rho \geq 0$, and corresponds to a trace preserving map, $\mathrm{Tr}(\rho) = 1$. This is essentially an extension of the normalisation condition of (3), meaning that the quantum states cannot simply disappear from the Hilbert space for this kind of quantum system.

Describing quantum states in terms of density matrices[4] will form a much more natural and simple way to express the evolution of qubits, although it is for now still just a change in formalism. For example, unitary evolution of a closed system can be described by taking the initial conditions

$$\rho(t_0) = \sum_i p_i \left|\psi_i(t_0)\right\rangle\!\left\langle\psi_i(t_0)\right|, \tag{47}$$

and evolving them by the unitary operator, $U(t, t_0)$, as

$$\rho(t) = \sum_i p_i U(t, t_0) \left|\psi_i(t_0)\right\rangle\!\left\langle\psi_i(t_0)\right| U^\dagger(t, t_0) = U(t, t_0)\rho(t_0)U^\dagger(t, t_0). \tag{48}$$

Measurements can be described similarly, with measurement operators M_n, such that the probability of getting the result n from a measurement will be

$$p(n) = \sum_i p\left(n|i\right) p_i = \sum_i p_i \,\mathrm{tr}\left(M_n^\dagger M_n \left|\psi_i\right\rangle\!\left\langle\psi_i\right|\right) = \mathrm{tr}\left(M_n^\dagger M_n \rho\right). \tag{49}$$

Density operators become more interesting in the case of quantum systems in the simple distinction between pure and mixed states. For a pure state, the density matrix is simply $\rho = |\psi\rangle\langle\psi|$. However, for a mixed state the original definition (46) is required, and the requirements for these types of states are that a pure state has $\mathrm{tr}(\rho^2) = 1$ while a mixed state has $\mathrm{tr}(\rho^2) < 1$. This mixed-state nature allows for convenient decompositions into the basis states with associated probabilities. A good example of this is the Bloch sphere. Recalling the Bloch vector from (8), and the new vector of Pauli matrices,

$$\vec{\sigma} = \left(\sigma^x, \sigma^y, \sigma^z\right), \tag{50}$$

an arbitrary mixed-state density matrix can be expressed as

$$\rho = \frac{1}{2}\left(\mathbb{I}_2 + \sum_{i=x,y,z} r_i \sigma^i\right). \tag{51}$$

[4]The terms "Density Operator" and "Density Matrix" will be used interchangeably.

Furthermore, the density operator allows for the closer analysis of subsystems of the larger composite quantum system at hand. This will be extremely useful in the study of OQS, and as an example of using it with the qubit states described this far, the density operator allows for the study of only one or two qubits out of a much larger device. This separation of subsystems is performed with the *reduced density operator*, which is obtained by taking the *partial trace* of a system. For example, when looking at a composite system comprising subsystems A and B, described by the density operator ρ^{AB}, the reduced density operator for subsystem A is expressed as

$$\rho^A \equiv \mathrm{tr}_B \left(\rho^{AB}\right). \tag{52}$$

Here, tr_B is the partial trace over the subsystem B, and is defined as

$$\mathrm{tr}_B \left(|a_1\rangle\langle a_2| \otimes |b_1\rangle\langle b_2|\right) \equiv |a_1\rangle\langle a_2| \,\mathrm{tr}\left(|b_1\rangle\langle b_2|\right) = |a_1\rangle\langle a_2| \,\langle b_2|b_1\rangle\,, \tag{53}$$

for the quantum states a_1, a_2, b_1, and b_2 being any normalised vectors in the state spaces of their respective subsystems.

4.2 Quantum Channels

In order to describe the change of a quantum system and the states in this formalism, such as time evolution or the effect of measurements, a more general approach than that of unitary transformations is required. This is the approach of *quantum channels*. When mapping operators to operators, mathematically this requires a *map*. To map states to states requires a special case of maps, to map states to a quantum channel, which does not need to be a unitary transformation and can map pure states to statistical mixtures. The requirements for a map to be a quantum channel follow previously used physically motivated axioms, so a channel maintains Hermiticity, positivity, and trace, as the eigenvalues are still positive and add up to unity. Additionally, more than just preserving positivity, a channel must fulfil the requirement of *complete positivity* (CP). Considering a positive map

$$\Phi : A \to B, \tag{54}$$

which maps positive elements to positive elements, as $a \geq 0 \Rightarrow \Phi(a) \geq 0$. Noting that any such linear map can induce another map

$$\mathbb{I}_k \otimes \Phi : M_k(\mathbb{C}) \otimes M_n(\mathbb{C}) \to M_k(\mathbb{C}) \otimes M_n(\mathbb{C}). \tag{55}$$

If this extended map is positive, then Φ is called k-positive. If Φ is k-positive for $\forall\, k \in \mathbb{Z}$, it fulfils the requirement of being completely positive. A few more propositions based on this concept will shed more light on the significance and usefulness of the CP condition. Considering an arbitrary Hilbert space of a system, $\mathbb{H}$, if the dimensions of $\mathbb{H}$ can be expressed as $\dim \mathbb{H} = n$, then a map Φ is CP if and only if it is n-positive. So, the CP requirement can be scaled down from $\forall\, k \in \mathbb{Z}$ to the dimensions of the Hilbert space at hand. Furthermore, if $P_n^+ = |\psi_n^+\rangle\langle\psi_n^+|$ is a projector, where

$$\left|\psi_n^+\right\rangle = \frac{1}{\sqrt{n}} \sum_{k=1}^{n} e_k \otimes e_k, \tag{56}$$

is a maximally entangled state in $\mathbb{H} \otimes \mathbb{H}$, for e_k being the elements of a fixed orthonormal basis in $\mathbb{H}$, then Φ is CP if and only if $[\mathbb{I}_n \otimes \Phi](P_n^+) \geq 0$ [15]. This means that if one verifies that $\mathbb{I}_n \otimes \Phi$ is a positive one-to-one projector P_n^+, then it is guaranteed that the same holds for all projectors $P \in M_n(\mathbb{C}) \otimes M_n(\mathbb{C})$. Additionally, considering two CP maps, Φ_1 and Φ_2, the tensor

product $\Phi_1 \otimes \Phi_2$ is also always CP. These properties of CP maps show that they are deeply rooted in quantum physics, as the presence of entangled states necessarily require them.

One of the most important characterisations of CP maps is that of Kraus maps. The Kraus/Operator Sum Representation of a map Φ is as follows. $\Phi : M_n(\mathbb{C}) \to M_n(\mathbb{C})$ is CP if and only if

$$\Phi(\rho) = \sum_\alpha K_\alpha \rho K_\alpha^\dagger, \tag{57}$$

for $\rho \in M_n(\mathbb{C})$, where K_α are Kraus operators [16]. A CP map is trace-preserving, if and only if

$$\sum_\alpha K_\alpha^\dagger K_\alpha = \mathbb{I}_n, \tag{58}$$

which finally allows for the definition that a map which is completely positive and trace preserving (CPTP) is a *quantum channel*.

4.3 Quantum Master Equations

A framework has now been established for a more general and robust description of the change from one quantum state to another. The natural next step is to use this framework to model quantum evolution, in the simpler unitary case and then extended to the more realistic OQS case. In a closed system, the evolution of a state $|\psi(t)\rangle$ is expressed in the Schrödinger equation,

$$i\frac{\mathrm{d}}{\mathrm{d}t}|\psi(t)\rangle = \mathscr{H}(t)|\psi(t)\rangle . \tag{59}$$

The solution of this is typically expressed in terms of a unitary time-evolution operator, $U(t, t_0)$, evolving the state from an initial time t_0 to an arbitrary time t, to give

$$|\psi(t)\rangle = U(t, t_0)|\psi(t_0)\rangle . \tag{60}$$

Returning this to the Schrödinger equation gives

$$i\frac{\partial}{\partial t}U(t, t_0) = \mathscr{H}(t)U(t, t_0) \qquad \text{with} \qquad U_0 = U(t_0, t_0) = \mathbb{I}_n. \tag{61}$$

For a time-independent Hamiltonian, $\mathscr{H}$, as is typical of a closed and isolated system, this can be integrated to give the common form of the unitary operator,

$$U(t, t_0) = \exp\left(-i\mathscr{H}(t - t_0)\right). \tag{62}$$

The requirement of a time-independent Hamiltonian is only necessary for this simple case. If the Hamiltonian of the system does have some time dependence, all that is required is that time-ordering must be accounted for. This is done through a chronological time ordering operator, $T_\leftarrow$. The operator arranges the time arguments to increase from right to left, to be consistent with matrix multiplication, and changes the unitary operator to

$$U(t, t_0) = T_\leftarrow \exp\left(-i\int_{t_0}^{t} \mathrm{d}\tau\, \mathscr{H}(\tau)\right). \tag{63}$$

This description can then easily be extended to the density operator formalism by considering the definition in (46), such that the quantum channel unitary evolution of the density matrix can be expressed as

$$\rho(t) = U(t, t_0)\rho(t)U^\dagger(t, t_0). \tag{64}$$

This can be differentiated with respect to time to obtain the *Liouville-von Neumann* (LVN) equation for the density matrix dynamics[5],

$$\frac{\mathrm{d}}{\mathrm{d}t}\rho(t) = -i\left[\mathscr{H}(t), \rho(t)\right]. \tag{65}$$

This equation is typically expressed in a similar form to the classical Liouville equation from statistical mechanics, as

$$\frac{\mathrm{d}}{\mathrm{d}t}\rho(t) = \mathscr{L}(t)\rho(t), \tag{66}$$

where $\mathscr{L}$ is the *Liouville super-operator*[6]. This equation leads to the time-ordered solution

$$\rho(t) = T_{\leftarrow} \exp\left(\int_{t_0}^{t} \mathrm{d}\tau\, \mathscr{L}(\tau)\right)\rho(t_0), \tag{67}$$

closely resembling that of (63), and has an analogous solution to the time-independent situation of (62), as

$$\rho(t) = \exp\left(\mathscr{L}(t - t_0)\right)\rho(t_0). \tag{68}$$

This derivation is done in the Schrödinger Picture of quantum mechanics, but can be easily recast into the Interaction Picture where it will be of more use in further derivations. The full conversion to the Interaction Picture follows similar logic and is described in other sources [15], as it is not necessary for the present discussion. The final result is that the LVN equation in the Interaction Picture takes the differential and integral form, respectively, of

$$\frac{\mathrm{d}}{\mathrm{d}t}\rho_I(t) = -i\left[\mathscr{H}_I(t), \rho_I(t)\right] \qquad \& \qquad \rho_I(t) = \rho_I(t_0) - i\int_{t_0}^{t} \mathrm{d}\tau\left[\mathscr{H}_I(\tau), \rho_I(\tau)\right], \tag{69}$$

which forms the starting point of the perturbative approach to describing open system dynamics.

In an open system, there is generally the coupling of the quantum system of interest, S, to another quantum system of the environment, B. Each of these are each subsystems of the composite system $S + B$, which itself is assumed to follow closed-system Hamiltonian dynamics. It is thus necessary to extract a description of the *reduced system* S from the larger space. The composite Hilbert space of the two systems is defined in terms of the Hilbert spaces of the subsystems,

$$\mathbb{H} = \mathbb{H}_S \otimes \mathbb{H}_B, \tag{70}$$

such that the total system Hamiltonian can be defined as

$$\mathscr{H}(t) = \mathscr{H}_S \otimes \mathbb{I}_B + \mathbb{I}_S \otimes \mathscr{H}_B + \mathscr{H}_I(t), \tag{71}$$

where $\mathscr{H}_I(t)$ is the Hamiltonian describing the interaction between the system and environment. From previous discussion about subsystems, the description of the reduced density matrix, $\rho_S(t)$, can be obtained through tracing out the environment system:

$$\rho_S = \mathrm{tr}_B\,\rho \Longrightarrow \rho_S(t) = \mathrm{tr}_B\left\{U(t, t_0)\rho(t_0)U^{\dagger}(t, t_0)\right\} \Longrightarrow \frac{\mathrm{d}}{\mathrm{d}t}\rho_S(t) = -i\,\mathrm{tr}_B\left[\mathscr{H}(t), \rho(t)\right]. \tag{72}$$

The systems are first assumed to be separate such that the initial state can be expressed as

[5] The commutator is defined as $[A, B] = AB - BA$.

[6] A super-operator is an operator which acts upon an operator to yield another operator.

$$\rho_{SB}(0) = \rho_S(0) \otimes \rho_B, \tag{73}$$

and undergoes unitary evolution according to (64). Taking the partial trace over the environment for this case results in the reduced system dynamics,

$$\rho_S(t) = \mathrm{tr}_B \left\{ U(t)\rho_{SB}U^\dagger(t) \right\} = \mathrm{tr}_B \left\{ U(t)\rho_S \otimes \rho_B U^\dagger(t) \right\} \equiv \Lambda(t)\rho_S(0), \tag{74}$$

to form the definition of the *dynamical map*, $\Lambda(t)$, which is a map from the space of the density operators of the reduced system, $S(\mathbb{H}_s)$, to itself,

$$\Lambda(t) : S(\mathbb{H}_s) \to S(\mathbb{H}_s), \tag{75}$$

assuming that the environment, ρ_B, and final time, t, are fixed. A simplified view of the result of a dynamical map such as this is shown in Figure 3.

As can be seen, the use of a dynamical map is a different means to the same end as tracing out the environment after unitary evolution. In practice a dynamical map makes things far easier to evaluate. However, the system dynamics are still very complicated in the general form, as can be imagined when considering the vast amount of possible evolutions and degrees of freedom involved. Because of this, a few key assumptions will be made in the following derivations, which make things far more tractable while also preserving the accuracy of the description as the general cases which are excluded by these assumptions occur less frequently than the simplified case. The dynamics with these assumptions are formally known as *Markovian systems*.

Beginning from the integral form of the interaction picture dynamics, (69), and substituting it into the differential form of the equation and taking the partial trace over the environment gives the following,

$$\frac{\mathrm{d}}{\mathrm{d}t}\rho_S(t) = -\int_0^t \mathrm{d}\tau\, \mathrm{tr}_B \left([\mathscr{H}_I(t), [\mathscr{H}_I(\tau), \rho_{SB}(\tau)]] \right), \tag{76}$$

where the assumption of $\mathrm{tr}_B [\mathscr{H}_I(t), \rho_{SB}(0)] = 0$ has been made, under the logic that the system is initially decoupled. The next approximation to be included is the Born approximation, which assumes that throughout the evolution of the composite system, the subsystems remain weakly coupled. Mathematically this means that the system-bath correlations are effectively negligible,

$$\rho_{SB}(t) \approx \rho_S(t) \otimes \rho_B. \tag{77}$$

This approximation leads to the integro-differential form of the system dynamics,

$$\frac{\mathrm{d}}{\mathrm{d}t}\rho_S(t) = -\int_0^t \mathrm{d}\tau\, \mathrm{tr}_B \left([\mathscr{H}_I(t), [\mathscr{H}_I(\tau), \rho_S(\tau) \otimes \rho_B]] \right). \tag{78}$$

It should be noted that in this equation the evolution of the system at future time-steps still depends on the past states for $\tau < t$, which means that the system keeps a detailed "memory" of the past states, which is part of what makes the general solutions so complicated. However, in most practical cases, the integrand quickly decays to zero in a *characteristic correlation time*, τ_B, and so does not maintain its memory for a significant influence on the system dynamics. This allows for the assumption that $\rho_S(\tau)$ can be replaced by its value at time t, $\rho_S(t)$, resulting in the Redfield equation,

$$\frac{\mathrm{d}}{\mathrm{d}t}\rho_S(t) = -\int_0^t \mathrm{d}\tau\, \mathrm{tr}_B \left([\mathscr{H}_I(t), [\mathscr{H}_I(\tau), \rho_S(t) \otimes \rho_B]] \right). \tag{79}$$

This assumption of the density operator not changing much within characteristic correlation time can be further enforced, to assume the operator does not change at all, through course-graining

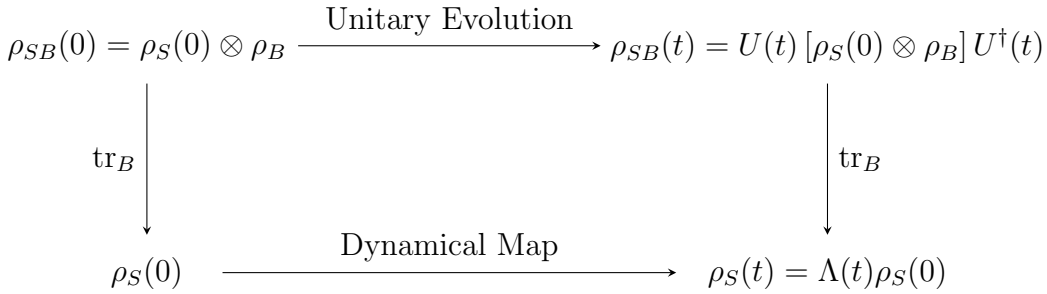

Figure 3: A commutative diagram showing the action of a dynamical map $\Lambda(t)$. Adapted from [15].

in time, replacing the limits of the integral by $[0, \infty)$, and for convenience later on making the interchangeable substitution of $\tau \to t - \tau$,

$$\frac{\mathrm{d}}{\mathrm{d}t}\rho_S(t) = -\int_0^\infty \mathrm{d}\tau\, \mathrm{tr}_B\left([\mathscr{H}_I(t), [\mathscr{H}_I(t-\tau), \rho_S(t) \otimes \rho_B]]\right). \tag{80}$$

This assumption of the system being "memoryless" is the application of the Markov approximation, and so the model thus far has been derived under the Born-Markov approximation of weak coupling and memoryless dynamics. This is the first form of the *Markovian Quantum Master Equation*. Now turning attention to the interaction Hamiltonian, $\mathscr{H}_I$, which can be expanded in terms of Hermitian operators associated with the system and environment, respectively,

$$\mathscr{H}_I = \sum_\alpha A_\alpha \otimes B_\alpha, \tag{81}$$

where A_α can be defined in terms of the eigenvalues of the system, S, and the corresponding projectors onto their eigenspace, $\Pi(\epsilon)$, such that

$$A_\alpha(\omega) = \sum_{\epsilon' - \epsilon = \omega} \Pi(\epsilon) A_\alpha \Pi(\epsilon'). \tag{82}$$

A_α is an eigenoperator of $\mathscr{H}_S$ with eigenvalues $\pm\omega$ (for the standard and Hermitian conjugate, respectively), and transfer to the interaction picture as $A_{\alpha,I} = \exp(-i\omega t)\, A_\alpha(\omega)$ and $A^\dagger_{\alpha,I} = \exp(i\omega t)\, A_\alpha(-\omega)$, with completeness being required,

$$A_\alpha = \sum_\omega A_\alpha(\omega) = \sum_\omega A^\dagger_\alpha(\omega). \tag{83}$$

The operators of the environment have a simpler behaviour, and are expressed in the interaction picture as

$$B_\alpha(t) = \exp(i\mathscr{H}_B t)\, B_\alpha \exp(-i\mathscr{H}_B t). \tag{84}$$

Using these definitions of Hermitian operators, the master equation can be recast in the following form[7],

$$\frac{\mathrm{d}}{\mathrm{d}t}\rho_S(t) = \sum_{\omega,\omega'}\sum_{\alpha,\beta} e^{i(\omega'-\omega)}\Gamma_{\alpha\beta}(\omega)\left[A_\beta(\omega)\rho_S(t)A^\dagger_\alpha(\omega') - A^\dagger_\alpha(\omega')A_\beta(\omega)\rho_S(t)\right] + \text{h.c.} \tag{85}$$

where the following correlation functions have been introduced,

[7] The abbreviation "h.c." stands for "Hermitian conjugate."

$$\Gamma_{\alpha\beta}(\omega) \equiv \int_0^\infty \mathrm{d}\tau\, e^{i\omega\tau} \left\langle B_\alpha^\dagger(t) B_\beta(t-\tau) \right\rangle, \tag{86}$$

$$\left\langle B_\alpha^\dagger(t) B_\beta(t-\tau) \right\rangle \equiv \mathrm{tr}_B \left(B_\alpha^\dagger(t) B_\beta(t-\tau) \rho_B \right). \tag{87}$$

Now the final approximation of the derivation can be made: the secular approximation. This requires the definition of two more characteristic time scales. The intrinsic evolution time of the system, τ_S, and the relaxation time of the open system, τ_R. If the system has $\tau_S \gg \tau_R$, the exponential terms can be ignored as they oscillate fast enough to average out to zero, similar to the RWA of (42). Following this, the environment correlation functions can be decomposed into their real and imaginary components,

$$\Gamma_{\alpha\beta}(\omega) = \frac{1}{2}\gamma_{\alpha\beta} + iS_{\alpha\beta}(\omega), \tag{88}$$

where the new definitions, for fixed values of ω, are

$$\gamma_{\alpha\beta}(\omega) = \Gamma_{\alpha\beta}(\omega) + \Gamma_{\alpha\beta}^*(\omega) = \int_{-\infty}^\infty \mathrm{d}\tau\, e^{i\omega\tau} \left\langle B_\alpha^\dagger(\tau) B_\beta(0) \right\rangle, \tag{89}$$

$$S_{\alpha\beta}(\omega) = \frac{1}{2i} \left(\Gamma_{\alpha\beta}(\omega) - \Gamma_{\alpha\beta}^*(\omega) \right), \tag{90}$$

which form a positive matrix and a Hermitian matrix, respectively. Putting all of these definitions together finally results in the *Lindbladian generator*[8] of the master equation in "first standard form" as[9]

$$\mathscr{L}_S \rho_S = -i \left[\mathscr{H}_S, \rho_S \right] + \sum_\omega \sum_{\alpha,\beta} \gamma_{\alpha\beta}(\omega) \left(A_\beta(\omega) \rho_S A_\alpha^\dagger(\omega) - \frac{1}{2} \left\{ A_\alpha^\dagger(\omega) A_\beta(\omega), \rho_S \right\} \right), \tag{91}$$

from which the matrix $\gamma_{\alpha\beta}(\omega)$, which is real and positive, can be diagonalised through some unitary transformation and the sum over ω can be evaluated to obtain the Gorini, Kossakowski, Sudarshan, Lindblad (GKSL) [17, 18] Markovian master equation,

$$\frac{\mathrm{d}}{\mathrm{d}t}\rho_S = \mathscr{L}_S \rho_S = -i \left[\mathscr{H}_S, \rho_S \right] + \sum_\alpha \gamma_\alpha \left(A_\alpha \rho_S A_\alpha^\dagger - \frac{1}{2} \left\{ A_\alpha^\dagger A_\alpha, \rho_S \right\} \right). \tag{92}$$

This is the general form of the quantum master equation used to describe the evolution of the density matrix for simple open systems, such as that of quantum computers. This is because the Born-Markov approximation can be violated in some devices, transferring them to the Non-Markovian regime. However, for the present discussion, this form of the equation will suffice. For example, in the case of a two-level atom in a zero-temperature reservoir, which describes spontaneous emission in a vacuum, the master equation has the following form,

$$\frac{\mathrm{d}}{\mathrm{d}t}\rho = -i \left[\mathscr{H}, \rho \right] + \Gamma \left(\sigma^- \rho \sigma^+ - \frac{1}{2} \left\{ \sigma^+ \sigma^-, \rho \right\} \right), \tag{93}$$

where the Hamiltonian has the form $\mathscr{H} = \omega_0 \sigma^z$, and the emission coefficient, Γ, is defined by the state-transition probability of the system. The jump operators in this case are matrices representing the transitions between polar states, expressed by

$$\sigma^+ = \begin{pmatrix} 0 & 1 \\ 0 & 0 \end{pmatrix} \qquad \sigma^- = \begin{pmatrix} 0 & 0 \\ 1 & 0 \end{pmatrix}. \tag{94}$$

[8] A generalisation of the Liouville super-operator introduced in (66).

[9] The anti-commutator is defined as $\{A, B\} = AB + BA$.

This demonstrates that a quantum system connected to an environment will undergo non-unitary evolution and decay to a ground state. This decay is only exacerbated by the presence of more uncontrolled degrees of freedom with which the system can interact, such as a non-zero temperature field, or a coupling to some electromagnetic field. In quantum devices these environmental interactions which influence the density matrix dynamics are known collectively as *quantum noise*.

4.4 Quantum Noise

As opposed to the deterministic evolution of a closed system, where the Hamiltonian can be used to predict the dynamics of the system, quantum noise causes many more fluctuations in the quantum state as it tends toward equilibrium with its environment. In a quantum computer this means that the state which is measured after a computation looks less and less like the state which was prepared as more time is taken for the system to be corrupted by the present noise. Quantum noise can be categorised into two forms, systematic and stochastic noise, each with its own framework.

A systematic error is more easy to account for, as it stems from traceable processes of qubit control or readout, such as an anharmonicity between the qubit and the applied microwave pulse to execute a quantum gate operation, which then applies the same error with each application of the process. When many of these types of errors are present in the full ensemble of qubit manipulations, they aggregate to form much less clear errors, and so appear to be random. These errors can be typically dealt with through hardware calibration or error-correction post-processing.

Stochastic noise, on the other hand, is much more random and stems from the fluctuations of parameters coupled to the qubit, which can come from current and voltage fluctuations in the circuits of the processor, nearby fluctuating electromagnetic fields, and temperature fluctuations from other atoms in the proximity undergoing their own emission. These are all uncontrolled fluctuations and lead to the decoherence of qubit states. The general way to combat stochastic noise such as this is in qubit design, as they can be engineered to be less susceptible to different kinds of noise, as discussed in the example of transmon qubits in Section 3. This is open to solutions from many overlapping fields such as electronics design, cryogenics, fabrication, and materials science, which all aid in the design of qubits which are shielded from the noise sources to which the type of qubit is most sensitive to. This is currently a large area of focus for the improvement of modern NISQ devices, which are highly susceptible to this decoherence.

To model and depict the noise process which the quantum state goes through, it is natural to return to the Bloch sphere representation introduced in Section 2. Whereas before the Bloch state representation was based on quantum states, $|\psi\rangle$, as in (7), this representation can be updated to the density operator formalism, as mentioned in (51), and expanded to give

$$\rho = \frac{1}{2}\left(\mathbb{I}_2 + \vec{r}\cdot\vec{\sigma}\right) = \frac{1}{2}\begin{pmatrix} 1+\cos\theta & e^{-i\phi}\sin\theta \\ e^{i\phi}\sin\theta & 1+\sin\theta \end{pmatrix} = \begin{pmatrix} |\alpha|^2 & \alpha\beta^* \\ \alpha^*\beta & |\beta|^2 \end{pmatrix}. \tag{95}$$

The important difference in this new framework is that if $\vec{r}$ is a unit vector then ρ represents the pure state ψ with $\mathrm{tr}(\rho^2) = 1$, while now in OQS mixed states can be dealt with, and are represented by Bloch vectors $|\vec{r}| < 1$ and $0 \leq \mathrm{tr}(\rho^2) \leq 1$ such that the vectors do not reach the edge of the Bloch sphere and are rather "shorter" versions which end at points in the interior.

The two kinds of noise have been introduced, and can be investigated further to see how external noise affects quantum states. In this case there are again distinct categories, which can overlap to cause faster changes in the quantum state. These qubit errors can be described in the formalism of quantum channels, as introduced earlier in (57). When speaking of noise and quantum errors, it is more common to express quantum channels in terms of *operation elements*,

rather than Kraus operators, although the two frameworks are essentially the same, so to keep with convention the operator sum representation of quantum channels will now be expressed by

$$\mathscr{E}(\rho) = \sum_k \langle e_k| U \left(\rho \otimes |e_0\rangle\langle e_0|\right) U^\dagger |e_k\rangle = \sum_k E_k \rho E_k^\dagger, \tag{96}$$

where $|e_k\rangle$ is an orthonormal basis for the environment state space, $\rho_e = |e_0\rangle\langle e_0|$ is the initial state of the environment, and $E_k \equiv \langle e_k| U |e_0\rangle$ is an operator on the system, as the operation elements of the quantum channel $\mathscr{E}$. The first of the noise errors which will be discussed are the bit-flip/phase-flip channels. The *bit-flip* channel is the error of the qubit state either relaxing or exciting between the states $|0\rangle$ and $|1\rangle$, as illustrated in the left panel of Figure 4, with a probability of $1-p$, such that the operation elements are

$$E_0 = \sqrt{p}\,\mathbb{I}_2 \qquad \& \qquad E_1 = \sqrt{1-p}\,\sigma^x. \tag{97}$$

The *phase-flip* channel is quite similar to the bit-flip, but now along the z-axis, and so changes only the phase, with the operation elements being defined as

$$E_0 = \sqrt{p}\,\mathbb{I}_2 \qquad \& \qquad E_1 = \sqrt{1-p}\,\sigma^z. \tag{98}$$

A special case of this channel occurs when $p = 1/2$, as that corresponds to the qubit measurement in the computational basis, $|0\rangle$ & $|1\rangle$. The corresponding "flip" channel for the y-axis is the combination of the two previous channels, and is known as the *bit-phase flip* channel, with the following operation elements,

$$E_0 = \sqrt{p}\,\mathbb{I}_2 \qquad \& \qquad E_1 = \sqrt{1-p}\,\sigma^y. \tag{99}$$

To illustrate the effect of these channels changing the pure state "full-sized" Bloch vector to a mixed state representation, it should be noted that each of these channels effectively polarises the Bloch sphere to be oblate along the associated axis, minimising the extent of the sphere along the other two axes. This naturally leads to the state of

$$\mathrm{tr}\left(\rho^2\right) = \frac{1}{2}\left(1 + |r|^2\right) \leq 1, \tag{100}$$

satisfying the mixed state condition.

The next category of noise is that of the *depolarising channel*, which is effectively the quantum state decaying to a completely mixed state, where no more information is attainable from the qubit as all states are equally likely. The quantum channel is again defined in terms of the $1-p$ probability of depolarising, expressed as

$$\mathscr{E}(\rho) = \frac{p}{2}\mathbb{I}_2 + (1-p)\rho. \tag{101}$$

This is essentially the quantum system decaying to thermodynamic equilibrium at $t \to \infty$ with the environment, and as such the accessible Bloch sphere contracts while maintaining its shape, which again verifies the mixed state property of (100), and is illustrated in the right panel of Figure 4.

The next quantum noise channel is that of *amplitude damping*, which describes the energy dissipation to the fully mixed state at equilibrium with the environment. This energy loss occurs through processes such as the emission of photons from excited quantum states. This energy dissipation results in the damping of the strength of the signal of the qubit state when it is measured as the energy of the excited states is carried away by emitted photons rather than being kept within the two-level system. The quantum channel of this kind of noise is defined by the operation elements

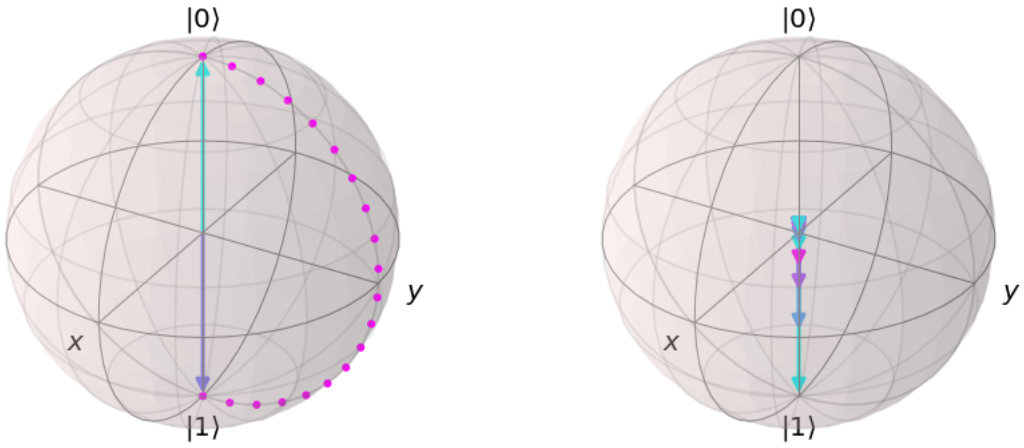

(a) Bit-flip (b) Amplitude damping

Figure 4: A Bloch sphere representation of the noise channels of bit-flip (a) and amplitude damping (b), respectively. The bit-flip channel is the process of an excited state, $|1\rangle$, decaying to the ground state, $|0\rangle$. The depolarising channel is the process of the system diffusing into a completely mixed state, in equilibrium with its environment.

$$E_0 = \begin{pmatrix} 1 & 0 \\ 0 & \sqrt{1-\gamma} \end{pmatrix} \qquad \& \qquad E_1 = \begin{pmatrix} 0 & \sqrt{\gamma} \\ 0 & 0 \end{pmatrix}, \tag{102}$$

where the probability of losing energy through photon emission is γ, as a spontaneous emission coefficient. To extend this to describe dissipation to an environment at finite temperature where the $1-p$ channel probability is included alongside the spontaneous emission, the *generalised amplitude damping* channel is required, with the following operation elements,

$$\begin{aligned} E_0 &= \sqrt{p}\begin{pmatrix} 1 & 0 \\ 0 & \sqrt{1-\gamma} \end{pmatrix}, & E_1 &= \sqrt{p}\begin{pmatrix} 0 & \sqrt{\gamma} \\ 0 & 0 \end{pmatrix}, \\ E_2 &= \sqrt{1-p}\begin{pmatrix} \sqrt{1-\gamma} & 0 \\ 0 & 1 \end{pmatrix}, & E_3 &= \sqrt{1-p}\begin{pmatrix} 0 & 0 \\ \sqrt{\gamma} & 0 \end{pmatrix}. \end{aligned} \tag{103}$$

This then describes the coupling of the system to other degrees of freedom such as nearby spins or electromagnetic field fluctuations as well as the photon emission decay to thermal equilibrium, and so is used to describe the T_1 relaxation time, which will be elaborated upon in a later section. The final quantum noise channel to be introduced is *phase damping*, which is similar to the amplitude damping channel. However, this channel describes the loss of quantum information without the loss of energy, through the eigenenergies not decaying but rather obtaining a relative phase change. The operation elements are also analogous to the amplitude damping channel, as in this case they can be defined in terms of the probability, λ, of a photon scattering in the system without loss of energy,

$$E_0 = \begin{pmatrix} 1 & 0 \\ 0 & \sqrt{1-\lambda} \end{pmatrix} \qquad \& \qquad E_1 = \begin{pmatrix} 0 & 0 \\ 0 & \sqrt{\lambda} \end{pmatrix}. \tag{104}$$

Similar to amplitude damping, the E_0 operation only reduces the amplitude of $|1\rangle$, and conversely to the amplitude damping channel, the E_1 operation destroys the $|0\rangle$ state while damping the amplitude of $|1\rangle$. This channel is not as frequently included in the descriptions of quantum noise, as the operation elements can be unitarily recombined to show that

$$E_0 = \sqrt{\alpha}\,\mathbb{I}_2 \qquad \& \qquad E_1 = \sqrt{1-\alpha}\,\sigma^z, \tag{105}$$

for $\alpha = \left(1 + \sqrt{1-\lambda}\right)/2$, which is then the exact same channel as that of phase-flipping, however now with a better description for the physical process behind the noise.

Before moving on to the next discussion, it is worth describing the connection between photon emission and system temperature in more detail. The probabilities of the system being in the $|0\rangle$ or $|1\rangle$ states can be assumed to satisfy a Boltzmann distribution with the partition function[10]

$$Z = e^{-\varepsilon_0/T} + e^{-\varepsilon_1/T}. \tag{106}$$

Here ε_0 and ε_1 are the energies of the states $|0\rangle$ and $|1\rangle$, respectively, such that the probabilities of being in each state can be expressed as

$$p_0 = \frac{e^{-\varepsilon_0/T}}{Z} \qquad \& \qquad p_1 = \frac{e^{-\varepsilon_1/T}}{Z}. \tag{107}$$

Furthermore, the thermal average number of photons in a qubit oscillation mode with angular frequency ω is

$$\langle n \rangle = \frac{e^{-\omega/T}}{1 - e^{-\omega/T}} = \frac{1}{e^{\omega/T} - 1}. \tag{108}$$

4.5 Relaxation and Decoherence

The noise quantum channels discussed until now have set the background for how a qubit state can change. However, in real systems it is rare to see just one of these happen individually as an isolated event. The combination of these through coupling to nearby noise gives rise to processes of *relaxation and decoherence*. Within the framework of the Markovian master equations derived earlier, the Bloch-Redfield model describes these processes, notably in the regime of weak coupling to noise and short correlation times, which lead to two relaxation rates. These are relaxation,

$$\Gamma_1 \equiv \frac{1}{T_1} = \Gamma_{1\downarrow} + \Gamma_{1\uparrow}, \tag{109}$$

and transverse relaxation,

$$\Gamma_2 \equiv \frac{1}{T_2} = \frac{\Gamma_1}{2} + \Gamma_\varphi \tag{110}$$

with the pure dephasing rate, Γ_φ, being introduced. To visualise these relaxation and decoherence processes on the Bloch sphere, Figure 5 depicts what each of these represent. Longitudinal relaxation (Figure 5 left panel) occurs when the qubit couples to transverse (x-y axis) noise leading to the transitions between the $|0\rangle$ and $|1\rangle$ states. The transition $|0\rangle \to |1\rangle$ is excitation, $\Gamma_{1\uparrow}$, and the transition $|1\rangle \to |0\rangle$ is relaxation, $\Gamma_{1\downarrow}$. The T_1 time is an exponential decay time which is the characteristic time scale for qubit relaxation to a steady state. Typical superconducting computers are kept in dilution refrigerators for cryogenic temperatures, on the scale of $T \approx 15\,\text{mK}$. At this point the excitation rate, $\Gamma_{1\uparrow}$, is exponentially suppressed leaving the relaxation rate, $\Gamma_{1\downarrow}$, to dominate. This allows for the quantum state to decay but not spontaneously re-excite which is ideal for computation as it allows the qubit manipulation to remain more stable. Additionally, this relaxation requires resonant noise frequency which matches the qubit frequency to cause this quantised transition. The T_1 time can be measured through exciting a ground state qubit and fitting an exponential function to extract the characteristic decay time.

[10] Continuing the atomic units convention, $k_B = 1$.

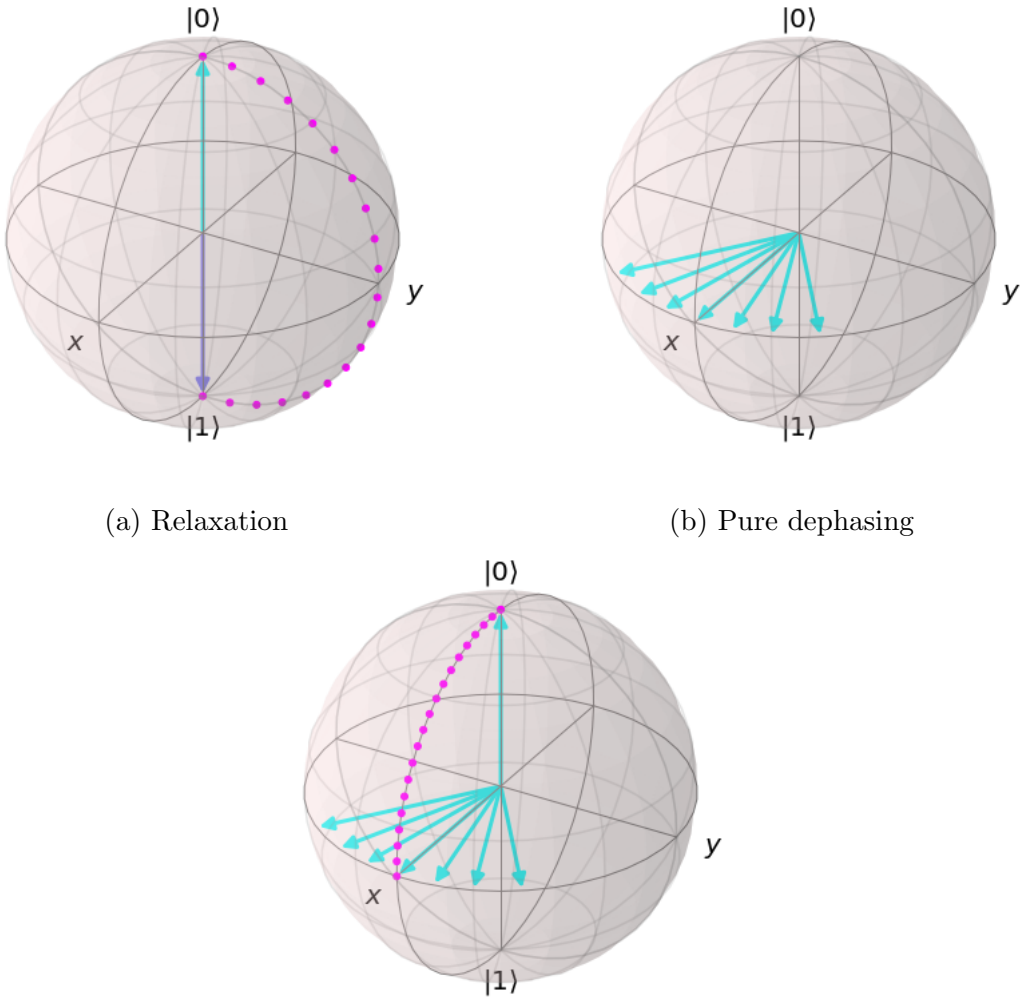

(a) Relaxation

(b) Pure dephasing

(c) Decoherence

Figure 5: A Bloch sphere representation of the noise processes of relaxation (a), pure dephasing (b), and decoherence (c), respectively. Relaxation is the process of an excited state, $|1\rangle$, decaying to the ground state, $|0\rangle$. Pure dephasing is the fluctuations along the x-y axis from the initial $|+\rangle$ state in this example. Decoherence is the combination of starting in the ground state, moving to the transverse axis, dephasing, and going back to the ground state.

Pure dephasing (Figure 5 centre panel) occurs when the qubit is in a transverse state, such as $|+\rangle$, and couples with longitudinal noise, which results in the qubit frequency fluctuating, due to the newly non-zero qubit drive anharmonicity, Δ_q, from Equation (41). As a result the state vector diffuses in the transverse plane. This is an example of stochastic frequency fluctuations mentioned earlier, and depolarises the azimuthal phase, ϕ, with a rate of Γ_φ. Contrary to the longitudinal relaxation, this dephasing can occur at any noise frequency and so qubits are more susceptible to this, as well as this being the reason for the oscillating phase. This is an example of a phase damping form of noise, so no energy is lost to the environment, and as such is an elastic process which can be reversed.

Transverse relaxation, or *decoherence*, (Figure 5 right panel) is the combination of these two, as the qubit in the transverse state undergoes dephasing and then relaxes to the $|0\rangle$ state. This type of relaxation is what is known as a *phase-breaking* process, as the transition to the ground state, $|0\rangle$, removes all history of the direction and phase which the qubit had when in the transverse state. This relaxation rate can be measured through multiple experiments for different T_2 characteristic decay times. One such experiment is Ramsey interferometry, which excites the

ground-state qubit to the $|+\rangle$ state through a Hadamard or $R_x(\pi/2)$ operation, typically with a deliberate detuning Δ_q, and left to decay for a period of time before being projected back to the ground state $|0\rangle$. This is used to measure the T_2^* time, which indicates that the experiment is subject to *inhomogeneous broadening*, meaning that it is sensitive to fluctuations which are consistent within individual trials of the experiment but vary overall, as the experiment needs to be repeated to use statistical rigour to reduce stochastic noise fluctuations. To avoid these noise fluctuations, the T_2 experiment can be modified to the Hahn echo sequence. This performs the same sequence as the Ramsey experiment, however now with a σ^y pulse midway through the decay time, which avoids the sensitivity to inhomogeneous broadening mechanisms as the contributions to the dephasing from stochastic noise can be effectively refocussed into a smoother decoherence rate.

In the simple case where the inhomogeneous broadening noise is ignored, to see the influence these decay rates have on the density matrix of the single-qubit system, the Bloch-Redfield model [19, 20] is used to express the decay dynamics as follows,

$$\rho_{\text{BR}} = \begin{pmatrix} 1 + \left(|\alpha|^2 - 1\right) e^{-\Gamma_1 t} & \alpha\beta^* e^{i\Delta_q t} e^{-\Gamma_2 t} \\ \alpha^*\beta e^{-i\Delta_q t} e^{-\Gamma_2 t} & |\beta|^2 e^{-\Gamma_1 t} \end{pmatrix}. \tag{111}$$

Assuming a qubit is coupled to multiple independent sources of fluctuating noise, such as *flicker noise*, or $1/f$-noise, which originates from low-frequency fluctuations within the electrical circuits of the device, the statistics of the noise sources converge to a Gaussian distribution. The $1/f$-noise of the system generates a coherence function, $\chi_N(t)$, for N π-pulses used to refocus the noise. This then leads to an additional decay function, $\langle \exp(-\chi_N(t)) \rangle$, which describes the generalisation of pure dephasing to encapsulate non-exponential contributions to the decay functions in the Bloch-Redfield density matrix, which can now be generalised to

$$\rho_{\text{BR}} = \begin{pmatrix} 1 + \left(|\alpha|^2 - 1\right) e^{-\Gamma_1 t} & \alpha\beta^* e^{i\Delta_q t} e^{-\Gamma_2 t/2} e^{-\chi_N(t)} \\ \alpha^*\beta e^{-i\Delta_q t} e^{-\Gamma_2 t/2} e^{-\chi_N(t)} & |\beta|^2 e^{-\Gamma_1 t} \end{pmatrix}. \tag{112}$$

As will be seen in a later section, this relation only holds for the ideal case within the Bloch-Redfield model, which does not often occur in practical cases, so a more practical model is required with the assistance of the OQS descriptions.

4.6 Quantum Process Tomography

To bridge the gap between the past few concepts which have been introduced, it is important to discuss how the quantum operations and descriptions of qubit evolution relate to experimentally measurable quantities. After all, the concepts discussed before now have been in terms of quantum operators which are theoretical objects, whereas in experiments only bit-strings and numbers can be measured. So to characterise the dynamics of the quantum system from this perspective, an experimentalist requires a way to connect the measurements to the theoretical objects. The method used for this is known as *quantum process tomography* (QPT), and is an extension of *quantum state tomography* (QST).

For example, a quantum measurement is only going to result into a bit-string of 0's and 1's, or counts of those quantum states measured, so there is no way to distinguish the $|0\rangle$ or $|1\rangle$ state from the $|+\rangle$ state which is projected to $|0\rangle$ or $|1\rangle$ with equal probability when measured. To accurately estimate the collection of states ρ, it is necessary to repeat the experiment to have several copies of the states produced and use tomography to calculate the state before measurement collapses it. For example, with multiple experiment copies for a single-qubit, the density matrix can be expanded as

$$\rho = \frac{1}{2}\left(\text{tr}(\rho)\mathbb{I}_2 + \text{tr}(\sigma^x\rho)\sigma^x + \text{tr}(\sigma^y\rho)\sigma^y + \text{tr}(\sigma^z\rho)\sigma^z\right). \tag{113}$$

However, this is not quite enough to fully characterise the state, as the trace of the operations is an average of the observable quantities, such as the Pauli operators, which means that more repetitions of this process are required to have statistical rigour. Due to the probabilistic nature of quantum states, a large number of measurements, m, will obtain a series of outcomes, $\{z_i\}$, such that the estimate of the contribution to the density matrix will be

$$\mathrm{tr}(Z\rho) \approx \frac{1}{m}\sum_i z_i, \tag{114}$$

and similarly for the other terms in (113). With a large enough ensemble of measurements, a Gaussian distribution is formed, with a mean of (114) and a standard deviation of $\delta(Z)/\sqrt{m}$ for a single-measurement standard deviation $\delta(Z)$. This is then enough to fully characterise the density matrix for a single-qubit in terms of observables, and can be extended to sets of more than one qubit, following the expansion for an arbitrary system of n qubits,

$$\rho = \frac{1}{2^n}\sum_{\vec{v}} \mathrm{tr}(\sigma^{v_1}\otimes\sigma^{v_2}\otimes\cdots\otimes\sigma^{v_n}\rho)\sigma^{v_1}\otimes\sigma^{v_2}\otimes\cdots\otimes\sigma^{v_n}, \tag{115}$$

where the vector $\vec{v}$ represents each entry the Pauli vector, (50), and the indices v_i representing the qubit in the system, as in (32). This extension to multiple qubits is simple in theory, however much more impractical when applied to a system, as will be seen later. As this process is dependent on the statistical rigour of the calculations to give acceptable results, it is important to define how this success in tomography can be measured. The standard quantitative measure of this accuracy, or how close the experimental tomography is to the expectations of the system, is the *quantum state fidelity* of the system. It can be defined in terms of two operators as follows,

$$F(\rho,\sigma) = \left(\mathrm{tr}\sqrt{\sqrt{\rho}\sigma\sqrt{\rho}}\right)^2, \tag{116}$$

which is symmetric under the exchange of the operator order, and results in a scale of 0 to 1, from worst to best, depending on the orthogonality of the non-commuting operators.

Now that state tomography has been outlined, it can be used in the more general method of process tomography. The extension to process tomography is motivated by the same idea as before, to experimentally determine the processes which quantum states go through, to determine the quantum channel. The procedure begins with looking at a subspace, of dimension d, and choosing d^2 pure states $|d_i\rangle$, such that the density matrices based on these states, $|\psi_i\rangle\langle\psi_i|$, together form a basis set for the matrix space. Then, for each of these pure states, a quantum system is prepared in the initial state; after which the experimental process can be executed and characterised. Following this, in theory state tomography can be used to characterise each of the states and construct $\mathscr{E}(|\psi_i\rangle\langle\psi_i|)$, completing the process.

Unfortunately, in practice it is not so simple, and involves more non-trivial steps to construct a useful representation of $\mathscr{E}$ in terms of operation elements E_i. The algebraic process behind making this process more practical is delegated to dedicated sources, [16, 21], as it is not pertinent to the discussion at hand. The important outcome of the practical procedure of process tomography is the scaling in system size. For example, this procedure is simple enough for a single-qubit, as it only requires the determination of 12 parameters to fully characterise the quantum channel. For two qubits, however, the procedure requires 240 parameters for full characterisation, which is a significant increase and can be extrapolated for larger systems. So although this number is not too large for numerical algorithms to determine, it quickly becomes impractical for larger systems.

As mentioned before, small quantum computers of 1 or 2 qubits are not very practical, and so better methods for characterising quantum systems are necessary for the engineering of fault-tolerant high-qubit processors. This is an active area of research to find ways to circumvent

the demanding process of full process tomography. This discussion concludes the background required for the concepts used in this work, allowing for the progression to discuss the recent research done to implement these principles and create a map of where the present research fits into the larger scope of literature, which is the focus of the next section.

5 Literature Review

The concepts discussed so far have been kept mostly separate and spoken of from a theoretical standpoint without applying them to more complicated situations or experimental procedures. To cover these discussions of the topics which will be used in the results of this work, more recent work focussed on the different aspects of qubit dynamics is required. The focus of this section will be on the research performed mostly over the past two decades to give a survey of the current state of the literature around this work's focus as well as show the gaps in current research which will be contributed to by this dissertation.

5.1 Relaxation and Decoherence

An early example of researching qubit dynamics in NISQ devices is that of Tian, Lloyd, and Orlando (2002) [22], where the authors investigated the influence of the measurement process on the qubit state fidelity. The authors noted that in the process of measuring a quantum state, the necessary coupling between the qubit and the measuring apparatus which is used as a conduit to transfer information also transmits noise from the detector's environment, detracting from the measurement efficiency. Their investigation focussed on finding the limit of this efficiency in a direct current (DC) superconducting quantum interference device (SQUID) while calculating the noise transmission during the measurement process. The description of these processes and limits were then used to form estimates of the relaxation and decoherence parameters of the device.

The authors note that in quantum computers the qubits need to be coupled to each other in some way to be able to execute multi-qubit gates and make use of quantum entanglement, however as noted earlier this vulnerability to coupling cannot be isolated just between qubits and rather they also couple to degrees of freedom in their environment. To measure quantum states of qubits, the same kind of coupling is required between the qubits and a detector so that information about the measured state can be extracted. A stronger coupling between the detector and qubits means that more information can be gathered in a single measurement, which allows for less errors as fewer repetitions of the experiment need to be run. This measurement coupling is subject to the same problems of environmental interaction leading to noise and destroying the quantum information before it can be fully extracted. So it is necessary to have this coupling for measurement but also dangerous to the measurement fidelity, and thus requires an optimised process which minimises noise due to coupling while maximising measurement efficiency and fidelity.

In this experiment, they make use of a persistent-current (PC) superconducting qubit comprising three Josephson junctions in series through one superconducting loop, which is then measured by the SQUID detector. This combination was used for the authors to derive a full system Hamiltonian based on that of the qubit, the detector, and their coupling, based on a coupled harmonic oscillator system. They approached the act of measurement from the perspective of it being a perturbation of the total system which then gives rise to a measured ground state of the composite system. The important parameter in this perturbative approach is the ramping/bias current of the SQUID detector, as increasing this leads to the spin states of the qubit and SQUID to separate at which point the measurement can be made on the oscillator state of the detector. Using this as well as all of the other parameters of the system, the authors

derived an effective noise spectrum, as a function of qubit frequency, which is used in finding the optimal measurement strength to minimise noise and maximise efficiency. For simplicity they assumed the system operates at zero temperature, and using the effective noise frequency they derived approximations for the relaxation and decoherence rates of the system. They also found that better circuits can be designed for optimal readout efficiency as this is heavily dependent on the circuit parameters.

Further research into the relaxation and decoherence rates of qubits was performed by Smirnov (2003) [23], in which the authors considered the extension of the qubit system to be in a non-zero temperature thermal bath giving rise to Rabi oscillations. A difference in state-population in a qubit, or any two-level system, which is subject to a resonant electromagnetic field will oscillate at a frequency which is proportional to the strength of the EM field, and these oscillations are what are known as Rabi oscillations [24]. These oscillations are ubiquitous in almost all qubit devices, as it is very difficult to isolate qubits from these resonant EM fields. The author describes the processes of relaxation and decoherence as being a consequence of coupling to a dissipative environment of a heat bath, which can both be formulated in terms of a thermal noise spectral density, $J(\omega)$, as follows,

$$\frac{1}{T_1} = \frac{\Delta^2}{2\omega_0^2}\left[S(\omega)\right]_{\omega=\omega_0}, \tag{117}$$

$$\frac{1}{T_2} = \frac{1}{2T_1} + \frac{\varepsilon^2}{2\omega_0^2}\left[S(\omega)\right]_{\omega=0}, \tag{118}$$

$$S(\omega) = J(\omega)\coth\left(\frac{\omega}{2T}\right) \tag{119}$$

with Δ being the tunnel splitting, ε being the qubit energy bias, $\omega_0^2 = \Delta^2 + \varepsilon^2$, and T being the environment temperature. It is noted that additional noise sources, such as $1/f$-noise which behaves as $S_f(\omega) \sim |\omega|^{-1}$. These equations, however, only hold in the case of weak coupling with the heat bath, and in the absence of time-dependent external forces on the qubit. The author notes that decoherence can be suppressed through the use of an external driving force, which motivates the extension to a framework which can account for that, which the author uses the work by Bloch [25] to do. It is noted, however, that there is a need for the description of the qubit dynamics in the presence of a resonant drive. From this perspective the author demonstrates the effects of Rabi oscillations in the TLS to find field-induced modifications to the rates in (117), (118), and (119), from the approach of OQS. From this perspective the author assumes the rotating wave approximation, with sufficient justification in terms of the relevant frequencies involved, and derives non-Markovian expressions which are then adapted to the form of generalised Bloch equations which describe the qubit dynamics in the presence of thermal dissipation and Rabi fluctuations in one framework. Together this leads to an initial qubit Hamiltonian which includes interactions with a resonant field, $F(t)$, and coupling to a dissipative environment, $Q(t)$, and has the following form,

$$\mathscr{H} = \frac{\Delta}{2}\sigma^x + \frac{\varepsilon}{2}\sigma^z - \sigma^z F\cos\left(\omega_0 t\right) - \frac{Q}{2}\sigma^z. \tag{120}$$

After all of the approximations and derivations are performed, this system effectively leads to a much more complicated longitudinal relaxation rate than encountered before, as described by

$$\begin{aligned}\frac{1}{T_1} &= \frac{1}{2}\left(\Gamma_x + \Gamma_y\right) \\ &= \frac{\Delta^2}{4\omega_0^2}S(\omega_0) + \frac{\varepsilon^2}{4\omega_0^2}S(\Omega_R) \\ &\quad + \frac{\Delta^2}{8\omega_0^2}\frac{(1+3\alpha)S(\omega_0+\Omega_R) + (1-3\alpha)S(\omega_0-\Omega_R)}{2},\end{aligned} \tag{121}$$

where Ω_R is the Rabi frequency, and α is a factor dependent on the ratio between the Rabi and qubit frequencies to demonstrate resonance. The author continues to demonstrate that the Rabi oscillations eliminate the divergence in the decoherence of the qubit due to flicker noise. Finally the author analyses necessary conditions of the Rabi oscillations in the phase qubit having a resonance frequency equal to Ω_R when coupled to an LC-circuit.

For more recent research where these principles have been applied and investigated in modern quantum devices, it is worth discussing the work of Klimov et al. published (2018) [26], who investigated the fluctuations in relaxation times of superconducting frequency-tunable "Xmon" transmon qubits.

The authors note that while there has been much research into qubit relaxation mechanisms in the past, generally the analysis has been focussed on either the spectral or temporal resolution of the T_1 data, which does not offer a full description of the mechanisms behind the relaxation.

This paper aimed to remedy this gap by demonstrating the spectral and temporal resolution simultaneously to show that the significant fluctuations in measured T_1 times are due to TLS defects and *spectral diffusion* (time-dependent transition frequency variations). The combination of spectral and temporal resolution is important as it allows for the defects to be identified while the qubit dynamics are inferred, to provide a more generalised description of the relaxation process. These TLS defects include processes such as the qubit coupling to external degrees of freedom leading to phenomena like dielectric loss to the circuit.

The authors performed the standard T_1 measurement procedure, which consists of initialising a qubit into the $|0\rangle$ state, exciting it to the $|1\rangle$ state, and waiting a certain time before measuring the qubit to find the state distribution. For a single T_1 resolution the authors repeated this sequence 2000 times, for 40 delay times, spaced in $\log_{10}$ increments, from 0.01 µs to 100 µs. This range is large enough to give statistically significant results with active initialisation and readout protocol times of 7 µs and 1 µs, respectively, with an average fidelity of > 0.95. This allowed for the resolution of a relaxation time for a single frequency to be performed over roughly 2 s, and the full spectroscopic range of 400 MHz in steps of 1 MHz to take roughly 15 min, giving a full temporal and spectroscopic resolution profile.

The analysis of the results obtained through these experiments demonstrate the instability of the T_1 times as they varied up to an order of magnitude, and fluctuated abruptly between extreme points within the 15 minute intervals, and form multi-modal distributions with longer tails towards shorter relaxation times, being characteristic of sparse, but deep, relaxation resonances which form strong relaxation channels. The authors mention several sources of the noise, such as bleed-through microwave frequencies near the resonance frequency of the qubit, and qubit coupling to electric fields near the capacitor and Josephson junction nodes, with other small background noise which can be due to sources such as quasi-particles and measurement errors.

Altogether the significant noise sources show a combination of telegraphic and diffusive spectral diffusion regimes. Telegraphic defects experience discrete fluctuations in transition frequency, while diffusive defects experience gentle continuous drifts in transition frequency. The authors accurately model and describe these phenomena, verifying that their noise characterisation was accurate. The authors go on to express that the data they extracted showed a qualitative similarity to T_1 data obtained from other superconducting qubit architectures, such as 3D transmons and flux qubits, suggesting that these TLS defects are likely the source of relaxation time fluctuations native to superconducting qubits rather than the architecture used in this experiment. They do, however, highlight that these problems are not easily accounted for, although they potentially can be for NISQ devices, and require advancement of qubit calibration, circuit design, and fabrication will be necessary in the long term.

A report by Schlör et al. (2019) [27] reinforces these results from a different perspective, and a different variation of transmon qubit. In this the authors investigated long-term measurements of a highly coherent non-tunable transmon qubit to find low frequency burst noise

of qubit coherence times and transition frequency, similarly to the work previously discussed, through measuring the qubit relaxation and dephasing times along with the resonance frequency. Through analysis of these parameters and the correlations between them, the authors could infer information about the decoherence mechanisms in superconducting qubits. To fully characterise the stability and decay dynamics of transmon qubits, the authors measured not only the relaxation time, T_1, but also the Ramsey, T_2^R, and spin echo, T_2^E, coherence times and the transition frequency, ω_q, of the qubits.

The experimental procedures for measuring the new Ramsey and spin echo decoherence times are as follows. For the Ramsey experiment to measure T_2^R, the qubit is initialised in the $|0\rangle$ state, excited by a $\pi/2$ pulse onto the transverse axis of the Bloch sphere, left to decay for a variable time, and de-excited by another $\pi/2$ pulse back to the $|0\rangle$ state where it is measured. For the spin echo experiment to measure T_2^E, a similar procedure is followed, however now with a π pulse to rotate the state vector halfway around the Bloch sphere to point in the opposite direction is applied halfway through the variable decay time between the two $\pi/2$ pulses.

Their findings from long-term measurements depict substantial fluctuations in all of the relevant qubits parameters, and telegraphic noise once again suggesting the undesirable coupling of the qubit with environmental two-level systems. These results ascribe a small number of dominant TLSs near qubit resonance in addition to a bath of weakly coupled TLSs leading to the perceived $1/f$-noise in the background. The authors note that while other fluctuation sources, such as thermal variations, quasiparticle tunneling, and flux vortices, are likely present in the system, they contribute minimally to the observed noise results.

An important system is also introduced, a two-level *fluctuator* (TLF), which is a TLS that has a transition energy, $\hbar\omega_q$, close enough to the thermal level, k_BT, of the environment to undergo a thermally activated state switch which cannot be reliably predicted. The longitudinal coupling between these and TLSs gives rise to the telegraphic and spectral diffusion of resonance frequencies discussed before, which go on to cause the observed qubit parameter fluctuations. The authors modelled the system Hamiltonian, for TLS index k, as follows,

$$\begin{aligned}\mathscr{H} &= \mathscr{H}_q + \mathscr{H}_{\mathrm{TLS},k} + \mathscr{H}_{\mathrm{int},k} \\ &\approx (\omega_q + \chi_k\sigma^z)\, a^\dagger a + \frac{1}{2}\left(\omega_{\mathrm{TLS},k} + \chi_k\right)\sigma^z - \alpha\left(a^\dagger\right)^2 (a)^2,\end{aligned} \tag{122}$$

for a dispersive shift, $\chi_k = g_k^2/\Delta$, and qubit-TLS detuning $\Delta = \omega_{\mathrm{TLS},k} - \omega_q$, where g_k is the coupling strength between the qubit and TLS. These parameters were measured and calculated through the experimental results and used to verify the qualitative descriptions of the relaxation dynamics of the qubits under the influence of interacting TLSs. The authors found strong correlation between the dephasing and fluctuations over a time scale range of seconds to days, and which were ascribed to dominant individual TLSs near conductor edges. This observation was reinforced by cross-correlation and power spectral density (PSD) analysis which also attributed the fluctuations to originate from interactions between thermal fluctuators and near-resonance TLSs. These results confirm the findings of Klimov et al. [26] in demonstrating that current NISQ devices with transmon qubits have coherence fluctuations up to an order of magnitude which places significant focus on continuous recalibration to maintain the reliability of the outputs of these devices. The authors also emphasise the fact that even this recalibration is a temporary solution and fundamental improvements in qubit stability will be required for scaling up to larger devices and to advance towards fault-tolerance.

Another contribution to the topic of this discussion comes from the work of Burnett et al. (2019) [28], which aimed to benchmark the stability of decoherence properties of superconducting qubits, in terms of the decay time metrics, T_1, T_2^*, T_φ, and ω_q. The approach which makes this work unique in the literature, as the authors note, is that it is more generalisable than previous works, as it does not rely upon tunable qubits or advanced reset protocols, which also

leads to more frequency stability and thereby less dephasing. To achieve this, the investigation was performed on a single-junction Xmon transmon qubit, without the presence of a SQUID which leads to extra $1/f$-noise suppression as the qubit frequency is decoupled from electric and magnetic flux. Furthermore, in the device used there were no individual qubit drive lines or qubit-qubit coupling connections, which served to deliberately isolate the qubits from as much external noise as possible so that a more precise study could be performed on the decoherence due to intrinsic mechanisms of the quantum system.

The study involved experiments performed on two separate qubits each on a chip of their own, with the primary differences between them being their Josephson-charging energy ratio, E_J/E_C, and that one of the qubit had its capacitor trenched such that dielectric loss was suppressed. To benchmark the decay dynamics, the standard T_1 sequence was performed on the qubits such that an exponential decay function could be fitted to the excited state population over time to extract the T_1 parameter. Each sequence was performed for 2 000 iterations over a period of 65 hours. The initial results indicated that the relaxation times were not synchronised, indicating that the dominant relaxation mechanism and associated fluctuations were local to each qubit, as intended. The decay times also had a large range across all of the iterations, with the T_1 value fluctuating by more than a factor of 2, confirming previously discussed results.

The experiments were repeated on a new time range spanning roughly 125 hours to allow for sufficient cooldowns between iterations, and the T_2^* times were measured from Ramsey experiments following the same protocol. Using these results the authors were able to extract several parameters of the qubit dynamics while fitting multiple noise functions to the experimental data to quantify their influence on the system and find which noise sources are dominant. The authors found that fluctuations in the T_1 time were accurately described by a Lorentzian noise model with switching rates in the range 75 µHz to 1 mHz, which eliminate quasiparticles and parasitic microwave modes as potential noise candidates, leaving the coherent qubit-TLS coupling as the dominant source of noise especially due to near-resonant TLSs. The results obtained here are in line with previously discussed studies, verifying the presence and influence of TLS noise.

A less restrictive and more realistic study, by Carroll et al. (2021) [29], investigates the spectral and temporal dynamics of single-junction transmon qubit T_1 times, through repeated measurements of the T_1 procedure via the *AC-Stark shift*, which is the shift of levels in a variable monochromatic EM field [30, 31]. The experiments were performed on an IBMQ 20-qubit device kept at ~ 15 mK, with focus on a group of 10 qubits with ~ 5 GHz frequency, through roughly 250 measurements over a period of 9 months to monitor the long-term consistency and correlations of the qubit dynamics. Rather than using the typical flux based TLS spectroscopy methods, the authors turn to a method of using off-resonant microwave pulses to drive the AC-Stark shift in qubit transition frequency to spectrally resolve the qubit T_1 times and use frequency sweeps to track the spectral diffusion of strongly coupled two-level systems.

The AC-Stark shift method consists of inducing an effective frequency shift, $\Delta\omega_q$, through the AC-Stark effect into resonance with a defect TLS which accelerates the qubit relaxation time, giving insight into the frequency location of the TLS. The Stark shift is modelled as a Duffing oscillator, as elucidated in refs. [32, 33],

$$\Delta\omega_q = \frac{\alpha_q \Omega_s^2}{2\delta_{qs}\left(\alpha_q + \delta_{qs}\right)}, \tag{123}$$

for a qubit anharmonicity, α_q, drive amplitude, Ω_s, and detuning between the qubit frequency and Stark tone, $\delta_{qs} = \omega_q - \omega_s$. These shifts in frequency were measured through a modified Ramsey experiment sequence, which consists of a $\pi/2$ pulse to excite the qubit from $|0\rangle$ to the transverse axis, performing the frequency sweep in $\Delta\omega_q$ (through controlling Ω_s) over a variable time rather than allowing the qubit to undergo pure dephasing, and then applying another $\pi/2$ pulse to return the qubit to $|0\rangle$.

The authors found strong correlation between the relaxation time long- and short-time means, averaged over several months and around the local qubit frequency, respectively. These results suggest that long-time T_1 averages may be estimated rapidly through this spectroscopy method, as the TLS spectral diffusion near the qubit frequency exhibits quasi-ergodic behaviour. They highlight that this work provides a new avenue of rapid process characterisation and device stability evaluation through this statistically rigorous method. These results remain consistent with previous discussions of TLSs having a characteristic dominant influence on the relaxation time of qubits.

In the research overview thus far, most discussions concerning TLS acceleration of relaxation and decoherence times have neglected the influence of secondary factors, such as quasiparticles and external thermal or electromagnetic field variations under the justification that they generally do not have a significant influence on the noise of the system. For a contrasting perspective, the work of de Graaf et al. (2020) [34] focusses on the process of trapped quasiparticles generating new forms of TLSs, referred to as "qTLSs", which go on to induce qubit decoherence and relaxation.

The authors note that most studies have been focussed on TLSs which reside outside qubit junctions within the metals and dielectrics of the circuit, leading to a focus on improved materials, however the charged surface TLSs and paramagnetic impurities lead to a stochastic backdrop in the superconductor for quasiparticles. These quasiparticles are generated by electromagnetic and ionising radiation from events such as high-energy cosmic rays impinging on the device, and when these particles dissipate energy they can couple as TLSs to qubits thereby decreasing their coherence times.

The authors found that quasiparticles can be trapped in superconducting quantum devices by rare elongated fluctuations in the disorder potential, which leads to multiple bound states within a single energy well which mimics the behaviour of typical TLSs. These properties were discovered through spectral, temporal, thermal, and magnetic field profiling and mapping of a planar superconducting quantum device.

To corroborate these findings, the work of Vepsäläinen et al. (2020) [35] investigates specifically the impact of ionising radiation on the coherence of superconducting quantum devices, as an origin of these qTLSs. The authors note that the superconducting qubit coherence is destroyed by the breaking of electron Cooper pairs into collections of quasiparticles. The experimentally observed density of these quasiparticles is significantly higher than the negligible level predicted by the superconducting formalism used in the design of quantum devices, highlighting the need for research such as this.

The authors claim that the dominant source of these broken Cooper pairs is ionising radiation from high-energy cosmic rays and environmental radioactive materials. They support this claim with experimental evidence and go on to show that the use of radiation shielding significantly decreases the incident flux of ionising radiation and increases the relaxation time of the qubits. The quasiparticle contribution to the qubit relaxation rate was modelled in terms of the superconducting gap, $\Delta \approx 180\,\mu\text{eV}$, the quasiparticle density, n_{qp}, and Cooper pair density, $n_{\text{cp}} \approx 4 \times 10^6\,\mu\text{m}^{-3}$, as follows

$$\Gamma_1 = \Gamma_{\text{qp}} + \Gamma_{\text{other}}, \tag{124}$$

$$\Gamma_{\text{qp}} = \sqrt{\frac{2\omega_q \Delta}{\pi^2 \hbar}} \frac{n_{\text{qp}}}{n_{\text{cp}}}. \tag{125}$$

The experiments performed to verify these claims consisted of exposing accurately calibrated transmon qubits, kept at roughly $\omega_q \approx 25\,\text{GHz}$ and $T_{\text{eff}} \approx 40\,\text{mK}$, to a ^{64}Cu source, undergoing radioactive decay[11] with a half-life of 12.7 h, and measuring the relaxation rate repeatedly over

[11] The decay modes for this isotope are β^+ (17.9 %), β^- (39 %), electron capture (43.1 %), and γ-radiation/internal conversion (0.475 %)

a 400 h period. The cosmic ray presence and spectra were measured using industry standard equipment used in other cosmic ray detection experiments. The shielding component of the experiment was performed by encasing the quantum device and its cryostat in a box made of 10 cm thick lead bricks, which could easily be used in the mathematical modelling of the predicted influence of the shield.

These experiments provided the authors with significant quantitative evidence to support the claims that naturally occurring ionising radiation incident on the quantum device has a strong impact on the coherence of the superconducting qubits. This was supported by the shielding attempt leading to a roughly 0.2 % improvement in qubit relaxation time, which the authors note is small but still significant as the current state of qubit coherence is suppressed by many of these small noise sources and this method is a simple actionable precaution which can be taken to improve qubit coherence times, as this method is already being used in many neutrino and dark matter detection experiments.

This concludes the discussion of recent research into relaxation and decoherence mechanisms of quantum devices, particularly with respect to the influence of TLSs, while a more thorough and intricate report on the matter has been created by Müller et al. (2019) [36], and a hardware-perspective work by McRae et al. (2020) [37], for details not included here. The next area of study worth highlighting in the landscape of relevant research is that of methods of characterisation and tomography of quantum devices and the efforts therein to mitigate errors in post-processing.

5.2 Characterisation and Tomography

To expand upon the discussion of QPT from Section 4.6, the work of Mohseni, Rezakhani, and Lidar (2008) [38] provides a review of all known methods at the time of complete characterisation of quantum dynamics as well as analysing the associated physical resources required. The authors also provide a discussion on the complexity of different methods of QPT, noting which methods are more efficient depending on the available resources in the system. Three main methods of QPT are discussed in this work, namely Standard Quantum Process Tomography (SQPT), Ancilla Assisted Process Tomography (AAPT), and Direct Characterisation of Quantum Dynamics (DCQD).

The idea behind SQPT, as introduced in Section 4.6, is the process of preparing d^2 linearly independent input operators, $\{\rho_k\}_{k=0}^{d^2-1}$, where $d = 2^n$ for n qubits, and using QST to measure the output states $\mathscr{E}(\rho_k)$. The quantum channels $\mathscr{E}(\rho_k)$ can be decomposed into a linear combination of basis states,

$$\mathscr{E}(\rho_k) = \sum_l \lambda_{kl}\rho_l, \tag{126}$$

where the parameters λ_{kl} are the measurement outputs, which can be expanded as expectation values of operation elements E_k,

$$\lambda_{kl} = \mathrm{tr}\left(E_k \mathscr{E}(\rho_l)\right), \tag{127}$$

for $E_k = \rho_k$. These expressions can be related through the formalism of quantum channels to provide two new expressions,

$$E_m \rho_k E_n^\dagger = \sum_l B_{mn,lk}\rho_l, \tag{128}$$

$$\lambda_{kl} = \sum_{mn} B_{mn,lk}\chi_{mn} \Longrightarrow \lambda = \mathbf{B}\chi. \tag{129}$$

The matrix $\mathbf{B}$ is $(d^4 \times d^4)$-dimensional and made of the bases $\{\rho_k\}$ and measurement operators $\{E_m\}$, the d^4-dimensional vector λ comes from the state tomography, and the super-operator χ is calculated from this equation and encompasses all of the information of the quantum channel $\mathscr{E}$. Using this method requires d^4 measurements to be made, where as in Section 4.6 each measurement requires an ensemble of data to be statistically stable.

The AAPT method is based upon the idea of QPT being an extension the QST framework. Within this tomography scheme, there is an auxiliary/ancillary system, B, attached to the principal system, A, such that the combined system can be prepared in a way that allows complete information about the dynamics to be imprinted on the final state, from which point QST can be performed on the extended Hilbert space, $\mathbb{H}_{AB}$, to extract complete information of the unknown quantum map which acts upon the principal system.

The input state of the composite system must have a good measure of faithfulness to the map, $\mathscr{E}$, for QST of the outputs to be able to provide a complete identification of the unknown map. This measure of faithfulness can be formalised and quantitatively described, in terms of the eigenvalues of the input state. This requirement of faithfulness is essentially an invertibility condition based on the linearity of the composite map, $\mathscr{E} \otimes \mathbb{I}_n$, which ensures that the information of the process is imprinted linearly onto the output states. Performing QST on the output state, $(\mathscr{E} \otimes \mathbb{I}_n)\rho$, gives a set of linear relations of possible measurement outputs in the elements of $\mathscr{E}$ and ρ. These components join to form a set of linear equations for the unknown map which can then be solved for the full process tomography. As this process is more intricate than SQPT, there are more conditions and approaches to the methodology, delegated to the initial review, however this description summarises the essence of the AAPT method.

The method of DCQD is based upon some of the ideas of AAPT, in that it also makes use of an ancilla system, however contrary to AAPT it does not require the step of inverting a full $(d^2 \times d^2)$-dimension matrix, which is what makes the method direct. Instead, it makes use of different input states a *fixed measurement apparatus* to analyse Bell states, as in Equation (14), at the output. This method uses certain entangled states as the inputs, and then makes use of a simple error detection measurement on the composite Hilbert space. The outcomes of this are directly related measured probability distributions, negating the need for an inversion in the solution of the linear system of equations to express the unknown map. Instead, the χ matrix elements of linear quantum maps are directly observable in experiments, which are essentially Bell state measurement experiments.

The authors found through their modelling and experiments that quantum systems with controllable single-body and two-body interactions the DCQD method is the most efficient, requiring less experimental configurations and elementary operations. In quantum systems where the two-body options are not accessible, the DCQD and AAPT methods are no longer applicable, leaving the SQPT method as the most efficient.

For a more practical approach, the work of Merkel et al. (2013) [39] investigates the application of the standard approaches to QPT to demonstrate their experimental inaccuracy in cases where the quantum states and measurement operation elements used in the tomography sequence are generated by gates and drive pulses which contain significant systematic error which is not accounted for in the theoretical framework. These kinds of errors, State Preparation And Measurement (SPAM) errors, are not remedied through the broadening of measurement ensembles as discussed in the statistical requirements in Section 4.6.

Furthermore, the authors introduce a new method of tomography better suited to the practical setting, which reconstructs a complete library of quantum gates self-consistently, based upon a likelihood function which is independent of the physical gates used in the tomography process and can thus be optimised for any system. The method of oversampling to create larger ensembles of statistically stable measurements serves well to eliminate stochastic measurement errors, however does not have the same effect in eliminating SPAM errors, as the apparatus

used for these operations have the same degree of error as the quantum process which is being interrogated, so the intrinsic error only gets propagated.

The authors note there are other methods which have been crafted to avoid these errors, such as self-correcting QST [40] or a bootstrap method [41], however those approaches rely more on assumptions about the gate error model of the device at hand, which is not a necessary assumption in the formulation of the method created in this work. The authors demonstrate attempts at QPT based upon likelihood functions which do not account for SPAM errors to demonstrate the inaccuracies which render the methodology unsuccessful. The experiments were performed on single junction transmon qubits, with the tomography focussed on a pair of two coupled qubits. This is used as the starting point for the development of a new method which modifies the maximum likelihood function to incorporate uncertainty of the SPAM gates in the tomography process. This allows for the reconstruction of an entire library of quantum gates, rather than simply characterising the unknown quantum map as in SQPT.

These claims are validated by the experimental results of the application of the method in the same context as the experiment which demonstrated the failure of SQPT to fully characterise the entire process. The self-consistent method outperforms SQPT in estimation accuracy while making use of the same number of experiments, with only polynomial increase in the classical post-processing sequence. This work serves to demonstrate the intricacies involved in the accurate mapping of qubit dynamics in real systems as an actively improving field of research.

An often overlooked category of tomography is that of Quantum Detector Tomography (QDT), which focusses not on the processes a quantum state undergoes in its evolution, but rather the performance of the detector apparatus which makes the final measurement of the output state. This topic is the focus of the work by Chen, Farahzad, Yoo, and Wei (2019) [42]. In this study, the authors apply methods of detector tomography to cloud-accessible quantum devices hosted by IBM. In QST, the idea is to use a set of projectors and measure them with respect to some unknown state which yields a set of data describing the state. Conversely, in QDT the idea is to use a set of unknown states to estimate a fixed, but unknown, set of measurement operators which characterise the detector.

In this study, the authors performed QDT on two of IBM's 5-qubit devices in an attempt to fully characterise the detectors of these devices. The sequence used consisted of initialising the qubits in the ground state, $|0\rangle$, and performing a series of combinations of σ^x, H, and S gates for 100 iterations of the maximum 8192 shots for each iteration. The authors used maximum likelihood estimation [43] to calculate the Positive-Operator Valued Measure (POVM) parameters to describe the projectors to be used in QDT. The authors performed this process for single-qubits, which can be mathematically isolated from the other 4 and should in principle not cause any discrepancies although the authors found this to not hold strictly. They repeated the procedure for two-qubit pairs as well, with larger groups of qubits having a trivial expansion in the procedure.

The discrepancies found by the authors in the single-qubit case were most prevalently displayed in the difference between individual measurement, where one qubit is manipulated while the rest are left idle, and parallel measurement, where the same sequence of gates is executed on all of the qubits simultaneously and measured individually. In principle these procedures should provide the same results, excluding statistical fluctuations, however undesirable cross-talk and correlations between the qubits prevents this. These findings are supported by the two-qubit procedures providing evidence of a clash between the desired coupling between qubits which allows for entanglement and the fluctuations observed when no qubit correlation was applied. The authors suggest that a design modification would be beneficial with multi-qubit detector models being used which can account for the observed behaviour rather than single-qubit detector models acting in parallel.

To extend upon the idea of advancing QDT procedures in real quantum devices, the work of

Maciejewski, Zimborás, and Oszmaniec (2020) [44] proposes a framework to reduce the impact of readout errors through post-processing after the implementation of QDT. The authors note that if the detector is only affected by classical stochastic invertible noise then the outcome statistics can be corrected and included in the device calibration for further experiments. They perform this procedure on devices offered by IBM and Rigetti, to measure the practical improvements which it has to offer in the use cases of QST, QPT, and certain quantum algorithms which are not typically successful on NISQ devices.

The idea behind mitigating the invertible stochastic noise is that it creates a map which describes the noise profile which can be used to invert the map to classically reverse the effects of the quantum noise, which is done through solving a system of equations containing the product of this map and the vector of experimental statistics, similarly to the procedure of calculation in SQPT discussed earlier. This work aimed to present this framework as well as an analysis of its accuracy on real devices. The authors note that this form of noise analysis works well for superconducting transmon qubits, which have classical noise as the dominant source of measurement noise, making the devices offered by IBM and Rigetti suitable choices for experimental implementation.

This method of post-processing was algorithmically applied in conjunction with QDT methods similar to those introduced earlier, with the objective being to find the single-qubit "correction matrix",

$$\Lambda^{-1} = \frac{1}{1-p-q}\begin{bmatrix} 1-q & -q \\ -p & 1-p \end{bmatrix}, \tag{130}$$

for the measurement operators,

$$M_1 = \begin{bmatrix} 1-p & 0 \\ 0 & q \end{bmatrix} \qquad M_2 = \begin{bmatrix} p & 0 \\ 0 & 1-q \end{bmatrix}, \tag{131}$$

where $p, q \in [0, 1]$ are the respective probabilities for erroneous detection measurement for the states $|0\rangle$ and $|1\rangle$. For multi-qubit systems, the single-qubit correction matrices of each component qubit are stitched together using tensor products,

$$\Lambda^{(n)} = \bigotimes_{i=1}^{n} \Lambda_i \qquad \Lambda_i = \begin{bmatrix} 1-p_i & q_i \\ p_i & 1-q_i \end{bmatrix}. \tag{132}$$

Through implementations of this method on a variety of quantum circuits, including SQPT gates and a two-qubit version of Grover's algorithm, on IBM's 5-qubit device the authors found substantial improvements in the performance of the device. These observations were compared to other error-mitigation schemes and found to be a successful framework especially considering that it is no more hardware intensive than standard QDT, and is an easily implementable classical processing scheme which can assist significantly in the performance of NISQ devices.

As another example of the tomography and characterisation of quantum devices being performed primarily with classical post-processing, the work of Kandala et al. (2019) [45] investigates the process of error mitigation through an extrapolation of data from an ensemble of experiments with varying noise to allow for the calibration and error correction of outputs from single- and two-qubit procedures.

This serves as an example of using noisy quantum hardware to numerically account for the presence of noise throughout a collection of experiments and not need to make any hardware changes to obtain reliable results. The experiments performed in this study were implemented on a 5-qubit fixed-frequency Josephson-junction transmon qubit device hosted by IBM, and consisted of a series of gate sequences similar to SQPT using basis gates and multiple equally-spaced unitary rotation gates.

To advance the processing of tomography information even further, the work of Palmieri et al. (2020) [46] demonstrates the use of machine learning, in the form of a supervised neural network, to perform accurate filtering of experimental data to uncover patterns which characterise the measurement probabilities and the tomography of the system while SPAM errors are eliminated.

The supervised learning approach allows for the specific targeting of SPAM errors, and as the procedure of tomography is heavily data driven due to the ensembles of measurement results required, this method of machine learning assistance is a natural fit. The framework developed in this work is adaptable to many systems, as it is not dependent on the specific apparatus used but rather experimental data, and is in the case of the demonstration provided by the authors performed on a photonic quantum device with higher dimensional states encoded in the spatial modes of single photons, fitting well with the high-dimensional nature of the neural network architecture.

The authors constructed a Deep Neural Network (DNN) of 36-neuron input and output layers with two hidden layers with 400 and 200 respective neurons. The size of the input and output layers is guided by the d^2 measurement count requirement of the tomography experiments and the reconstruction of a Hermitian density matrix, ρ, for a set of $d = 6$ Hilbert space dimensions. In an attempt to avoid over-fitting and make the model more robust against variations, a drop-out approach was used to include a drop probability of 0.2 between the two hidden layers, where the entries most likely to skew the training are excluded from the model. A rectified linear unit (ReLu) was used for the activation function of the input and output layers, with the hidden layers making use of a softmax activation function to provide normalised probability distributions of the predicted tomography parameter values. The model was trained on 7 000 states, with 1 500 being left for validation and a final 2 000 used for testing of the model.

The results of applying the trained DNN to the experimental procedure of full state tomography, including QPT and QDT, resulted in a 10 % increase in reconstruction fidelity compared to a process tomography approach to treating SPAM errors, and a 27 % increase compared to a protocol which is SPAM-agnostic and uses idealised measurements. These increases over current methods of mitigating the presence of SPAM errors demonstrate that this method can be highly effective, and is a natural choice due to the compatibility of the data-driven and high-dimensional nature of tomography. The authors note that although this method was applied to a photonic system in this work, which makes use of qudits or qumodes as computational elements, the framework is adaptable to qubit based technologies and the QPT methods discussed previously.

In a different approach to the application of machine learning methods to the tomography and characterisation of superconducting qubits, the work of Baum et al. (2021) [47] demonstrates the use of Deep Reinforcement Learning (DRL) to design a error-robust universal gatesets for quantum circuit control. In the typical control of qubits through the construction of gate-based quantum circuits, a set of universal basis gates are used to compose linear combinations to form more complex gates. For example, a set of these basis gates could be composed of CX, I, R_Z, $\sqrt{X}$, and X gates, representing the controlled-NOT, identity, rotation, and σ^x quantum operations. However, the implementation of these gates in practice leads to inaccurate execution or systematic errors such as the readout error. It is because of these errors in execution that processes such as error-correction post-processing or QDT are required to reconstruct the fidelity of the output states.

This work demonstrated the modelling and construction of a machine learning model, which operates through a reinforcement learning architecture, to algorithmically improve the design of a new set of basis gates which circumvent or counterbalance the systematic errors of typical basis gatesets. This higher level of control of basis gates was achieved through Qiskit Pulse [48], which is an extension of IBM's Qiskit Software Development Kit (SDK). This programming package allows for the precise control and design of the characteristics of microwave pulses used to execute gate controls on the qubits in the quantum devices. The exact shape of the pulses

is a representation of the control Hamiltonian of the desired change in quantum state, and is typically used in the construction of unique quantum gates.

The machine learning model used in this work consists of three ingredients: states, actions, and rewards. The state is a snapshot of the environment of the state at any time, the action is how the environment is influenced, and the reward is a measure of feedback from the environment used to alter the next action. The algorithmic process of using this model to assist gate design consists of executing an initial set of basis gates and measuring the fidelity of the output state, and feeding this data into the DRL model to alter the gateset in a way that improves this fidelity and nullifies the presence of systematic errors. This optimisation process is achieved through a specialised model of gradient descent which finds the path of least error in the landscape of parameters, as is typical in machine learning algorithms.

The implementation of this model lead to a significant improvement over the calibrated basis gates used by default in the quantum devices, by achieving up to a factor of 3 greater state fidelity. This demonstrates another approach based on the classical computation enhancement of quantum device performance, which can be easily deployed and implemented without the need of any engineering improvement of the actual quantum devices. This method is highly effective as it is an autonomous system which does not depend on any hardware parameters but rather the output data and level of control of the qubits themselves.

To approach the process of tomographically characterising quantum device performance from an OQS perspective, the work of Samach et al. (2021) [49] demonstrates the development and application of a hardware-agnostic protocol to reconstruct the Lindblad and Hamiltonian quantum channel operators to be used in Master Equation descriptions of quantum dynamics. This process is named Lindblad Tomography (LT) by the authors. They highlight the failures of current industry-standard tomography techniques, such as randomised benchmarking, in accurately describing noise processes and detailed quantum dynamics as those methods focus primarily on output fidelity. Similarly, they note that despite the success of techniques based on Maximum Likelihood Estimation (MLE) and self-consistent tomography, those methods only offer snapshots of the discrete moments of qubit evolution, which is not sufficient for observation of phenomena such as dynamical noise and qubit crosstalk.

The LT method presented in this work remedies these shortcomings by altering the tomography logic to extract parameters used in Markovian modelling of open system qubit dynamics, through the tomographic tools of MLE and analysis of SPAM errors. This method requires the assumptions that the quantum evolution is Markovian and can be modelled by a time-independent master equation, and that the SPAM errors do not vary in time. The process consists of applying a series of six single-qubit gates, $\{\mathbb{I}, X, R_Y(\pm\pi/2), R_X(\pm\pi/2)\}$, as in SQPT, after which the qubits undergo unhindered decay through an idling channel, followed by an application of one of three single-qubit gates, $\{\mathbb{I}, R_Y(-\pi/2), R_X(\pi/2)\}$, prior to measurement in the respective Pauli basis. This procedure is repeated for all combinations of the first and second set of gates as well as the measurement bases for a complete profile of the tomography. These results are then fed into an MLE routine to characterise the system and reconstruct the quantum loss channel.

This process allows for the extraction of the Kraus operators which describe the evolution of the qubit density matrix, which allow for the thorough investigation of the measure of Markovianity and the form of noise which most heavily influences the evolution of the system. The Markovianity of the system is measured through a simple characterisation of how well the Markovian GKSL master equation fits to the data, without requiring more intricate descriptions of non-Markovianity. This description is formally expressed by noting that for a time-dependent master equation,

$$\frac{\mathrm{d}}{\mathrm{d}t}\rho(t) = -i\left[\mathscr{H}(t), \rho(t)\right] + \sum_i \gamma_i(t)\left(L_i(t)\rho(t)L_i^\dagger(t) - \frac{1}{2}\left\{L_i^\dagger(t)L_i(t), \rho(t)\right\}\right), \tag{133}$$

with positive decay rates, $\gamma_i(t) > 0$, the trace distance between two initial states can only decrease for it to remain Markovian, and any increase in this trace distance contributes to the measure of non-Markovianity.

Applying this method to a superconducting quantum device allowed the authors to extract reliable experimental data which led to the numerical description of all the extracted parameters, such as the Hamiltonian, Lindbladians, and Kraus operators which gave more insight into which gate combinations, or decoherence channels, gave rise to the most significant non-Markovianity and allowed for a more accurate description of the noise environment influencing the evolution of the qubits.

The distinctions between Markovian and non-Markovian evolution of quantum devices has been a thoroughly researched area in its own, investigating the mechanisms which give rise to the regimes, as well as how to accurately describe them and model systems based on the memory of the systems. The next section will focus on the recent research performed on this topic.

5.3 Markovianity and Non-Markovianity

The work of Rivas, Huelga, Plenio (2014) [50] provides an introductory survey of the state of research in quantum non-Markovianity as well as a discussion of the most important aspects of the Markovian regime. They note that the topic of non-Markovianity can essentially be split into two categories: characterisation and quantification. The characterisation problem deals with the definitions and formal theories describing what constitutes a process as being Markovian and what the limits are. The quantification problem elaborates further on when a process is non-Markovian to describe exactly how much it deviates from the Markovian qualification, which becomes a measure of how well a Markovian model will approximate the system.

The characterisation problem discussed in this paper is primarily based on the *divisibility property* definition of Markovianity, although the authors recognise and discuss some of the other definitions as there are many approaches to this property. As for the quantification problem, the authors discuss most of the approaches used in current literature to classify them into the categories of measures and witnesses of non-Markovianity.

The details of these discussions are omitted from the present discussion as they are not of significant consequence to the current review, and so the only notable concept which will be included in the discussion ahead is the idea of a process being effectively non-Markovian based upon how much it deviates from a Markovian master equation model.

While this work discussed the concepts mostly in the form of theorems and proofs from a probability theory point of view, a similar discussion from the point of view of the subcategories of open quantum systems is discussed in a colloquium by Breuer, Laine, Piilo, and Vacchini (2016) [51]. The scope of these works demonstrates how thoroughly and attentively the preliminary concepts of Markovianity and non-Markovianity have been studied, outside and inside the quantum regime.

The work of Cerrillo and Cao (2014) [52] demonstrates a model of applying these concepts of non-Markovianity, specifically in a newly proposed approach of using non-Markovian dynamical maps to extract the information of the dynamics of the system based on the initial trajectories. These maps are then formulated into non-Markovian transfer tensors which are used to propagate the state of the system to predict the dynamics at arbitrary times. This method is coined as the non-Markovian transfer tensor method (TTM). The authors state that this method is equivalent to a solution of the Nakajima-Zwanzig (NZ) equation [53, 54], which is an extension to Markovian master equations to include a memory kernel of the system-bath interaction, $\mathscr{K}(t,t')$, and is expressed as

$$\frac{\mathrm{d}}{\mathrm{d}t}\rho(t) = -i\mathscr{L}_S\rho(t) + \int_0^t \mathrm{d}t'\,\mathscr{K}(t,t')\rho(t'). \tag{134}$$

This equation is typically very difficult to solve depending on the system it is applied to, which is why assumptions allowing for the Born-Markov approximation are more common, however as the TTM succeeds in this use case it allows for the reconstruction of the dynamical operators of (134) from the quantum trajectories of the system of interest.

The process of extracting the dynamical maps is based on tomographical methods of black-box engineering, which consists of initialising the dynamics of the system with a set of basis gates and performing "input-output" analysis on the propagation for each channel constructed. The dynamical maps here are generated for discretised times $t_k = k\delta t$ for δt time step sizes, such that the density operator evolves as

$$\rho(t_k) = \mathscr{E}_k \rho(0), \tag{135}$$

were the initial condition is the identity channel, $\mathscr{E}_0 = \mathbb{I}$.

In this work, the authors use the non-Markovianity definition of a system violating the semi-group property, as a Markovian system can be propagated through using the same map multiplicatively, whereas in non-Markovian processes, the dynamical maps need to be found independently. To avoid the inefficiency of this process, this framework transforms the set of dynamical maps into a set of transfer tensors, T, which can always be propagated forward multiplicatively, as

$$T_{n,0} = \mathscr{E}_n - \sum_{m=1}^{n-1} T_{n,m} \mathscr{E}_m. \tag{136}$$

This allows for the transformation of (135) to an expression of dynamical propagation,

$$\rho(t_n) = \sum_{k=0}^{n-1} T_{n,k} \rho(t_k). \tag{137}$$

The Nakajima-Zwanzig equation can be extracted through this method by identifying (134) as the continuous limit of (137) above, allowing for the identification of

$$T_{k,n} = (1 - i\mathscr{L}_S \delta t)\, \delta_{k,n+1} + \mathscr{K}_{k,n} \delta t^2, \tag{138}$$

for $\mathscr{K}_{a,b} = \mathscr{K}(t_a, t_b)$ and $\delta_{a,b}$ being the Kronecker delta. This shows why the transfer tensor formalism is a natural fit to the non-Markovian mapping of dynamical maps, and the authors go on to demonstrate the effectiveness of this model on non-Markovian data.

To demonstrate the prowess of this method, the work of Chen et al. (2020) [55] illustrates the practicality of this method through the IBM Quantum Experience platform, which hosts the IBM cloud-based quantum computers, to demonstrate the mild non-Markovian dissipation of these devices with spatial correlations. The authors also apply the TTM spectroscopy method to theoretical models, through which they demonstrate an efficient non-Markovian assessment scheme of the quantum process which reconstructs the noise correlation functions for two-qubit circuits where the noise influences are most prevalent.

When applying the TTM spectroscopy framework to the IBMQ hardware, the predictive power of the method is clearly shown to accurately match the observed behaviour of the qubit dynamics, demonstrating that the methodology encodes realistic decoherence effects on the qubits which are not accessible through the typical frameworks of Markovian models. The authors characterise this collective decoherence observed in the IBMQ devices as being due to the present of crosstalk between qubits and the presence of spatially correlated noise sources.

For a different approach to the characterisation of non-Markovian processes, the work of Pollock et al. (2018) [56, 57] develops a universal framework for the characterisation of arbitrary non-Markovian processes, without the need of solving the Nakajima-Zwanzig equation,

but rather experimentally reconstructing the quantum process through a mapping which the authors call a *process tensor*, which is formally expressed as a mapping from the sequence of quantum operations, $\mathbf{A}_{k-1;0} := \{\mathscr{A}_{k-1}; \ldots; \mathscr{A}_1, \mathscr{A}_0\}$, which are *control operations* representing all possible manipulations of the system, for any time step, $0 \leq k < K$ (for K total time steps in the quantum process), to the state ρ_k, as

$$\rho_k := \mathscr{T}_{k:0} \left[\mathbf{A}_{k-1:0}\right], \tag{139}$$

which fully characterises the quantum process through the process tensor $\mathscr{T}_{k:0}$.

The process tensor is a mapping from a set of control operations to a set of output states, which is universal in that it describes all quantum process as well simulated on a quantum circuit. The framework is agnostic of any underlying open system dynamics, and naturally accounts for multi-time correlations.

Furthermore, the authors represent the process tensor as a multi-body state that can be constructed through a set of entangled states, which encodes temporal correlations as spatial correlations, leading to a natural multiplicative operator representation. It can thus be seen that this framework is a natural extension to the transfer tensor method analogously to the extension of state tomography to process tomography. The authors rigorously develop the mathematical framework of the process tensor, to demonstrate that it is compatible with the broader formalism of non-Markovian processes, and opens an avenue for much broader process characterisation of quantum dynamics.

The progenitors of this work went on to collaborate with another group to demonstrate this method of non-Markovian process characterisation and control on real quantum devices [58], namely those hosted by IBM, although they note that the framework is applicable to any controlled quantum device. Through the experimental procedure executed across multiple devices, the authors demonstrate a significant improvement in reconstruction fidelity of the quantum states compared to other tomographical methods, reaffirming the prowess and necessity for this framework in devices and gate sequences which deviate from the Markovian regime by invoking environmental memory effects which need to be accounted for.

The authors note that the tomographically complete estimation required for this procedure is often impractical to obtain in experimental settings, providing a bottleneck in applying this framework. They go on to provide a new iterative work [59] to present methods to bound any facet of the multi-time processes with limited data to a satisfactory level of accuracy. These methods include procedures such as making use of smaller tomography bases coupled with typical error-mitigation techniques, optimising over the consistent space to allow for a more compatible fit of the process tensor framework to the constrained space which is within reach of the available data, and making use of a recent MLE projection routine developed by the same authors [60].

In the experimental application of the new methods, the results demonstrate the desired iterative improvements consistent with the claims of the authors, and highlight that the non-Markovian correlations continue to develop in the data with deeper quantum circuits, which indicates the need for more iterative methods to extend the success of this framework in predicting broader and deeper quantum circuits in NISQ devices.

With a survey of the current standing of the research in the field of quantum computing and open quantum systems now elaborated upon, the gaps in research in recent literature highlight the need for more investigation and experimental application of new methods to fully understand, characterise, and improve low-qubit devices. This provides the opportunity for this present work to contribute to these areas through a new perspective and experimental demonstration of processes and methods hitherto unconsidered. The work presented in the following section provides a full discussion of these new methods and results which may open paths to further conduits of research to understand the operation of superconducting quantum devices better and aid in the advancement of these NISQ devices.

6 Process of Findings

Now that the background has been laid out, in the discussion of underlying theoretical concepts and their applications in recent literature, the gaps in current research can more clearly be seen and contributed towards in this section of the thesis wherein the novel research will be discussed in detail. One such gap is the thorough demonstration of the dynamics of qubit evolution in conventional decay experiments to extract characteristic times and the accompanying description from the perspective of OQS. While there has been substantial research done on these topics separately, there is a void in the topic of their overlap, especially in the regime of performing this analysis on cloud-accessible quantum devices which are open to public use and research, rather than proprietary technology only accessible by the researchers presenting the data.

This playing field of open-access cloud-based experimentation allows for the additional scrutiny of independent validation of the results demonstrated in this work, as well as the ability to modify the procedures which will be presented in forthcoming sections to the researcher's needs. This accessibility will support the opportunity for this work to open new paths of investigation to understand and advance the performance of NISQ devices.

Additionally, the present work investigates the research gap of independently verifying the claimed performance parameters of open-access cloud-based quantum devices, as it offers a novel method of extracting hardware information which is not accounted for in the routine calibration of the backend devices. This new approach highlights some flaws in the modelling of the device function by the hosts, as it demonstrates numerically that there are unaccounted phenomena present in the operation of the quantum computers.

This work also makes use of methods typically seen mostly in the realm of machine learning, despite the versatility and efficiency which they offer. This highlights a current trend in research, as highlighted in Section 5.2, of machine learning methods being increasingly coupled to conventional methods of evaluating the performance of quantum technology. This trend is becoming increasingly popular as more of the component fields in these research topics are being shown to not be strictly rigid in their procedure and use cases, as the present work will demonstrate by making use of multiple components of neighbouring fields to provide new perspectives of performance evaluation.

6.1 Methodology

The focus of this work is based on investigating the hardware provided by IBM through their Quantum Experience [61], which is a cloud-based open-access interface to run quantum circuits on a selection of available devices. The interface is used through Qiskit [62], which is an open-source SDK for the Python programming language, equipped with tools to interact with and design quantum programs specifically for the IBMQ backend devices. This development framework of quantum programs has seen a lot of successful use cases in the compatibility with quantum simulations, through many of the research papers discussed previously [13, 33, 49], as well as a specialised demonstration of OQS simulations by García-Pérez, Rossi, and Maniscalco (2020) [63], which the present work takes inspiration from.

The IBMQ devices are consistently being improved upon and have new iterations of devices added to the ensemble regularly, while maintaining older architectures. Additionally, there are several devices which are essentially identical other than minor details and being located in various cities. This leads to a broad assortment of devices available for different use cases. This collection has a sizeable range of the different devices architectures used by IBM in their development journey, ranging from single-qubit to 127-qubit devices. Despite this range in architectures, including various qubit topologies and features, the qubits are all modelled through the same transmon qubit framework. This leads to the devices all having the same form of Hamiltonian.

This Hamiltonian is a variation of the conventional transmon modelling, the Duffing oscillator (27), with parameters specific to the hardware leading to some variations to the expression. For example, for a single-qubit device, the Hamiltonian in terms of qubit frequency, $\omega_{q,i}$, and anharmonicity, Δ_i, is

$$\mathscr{H} = \frac{\omega_q}{2}(\mathbb{I} - \sigma^z) + \frac{\Delta_i}{2}(O^2 - O) + \Omega_d D(t)\sigma^x, \tag{140}$$

where $O_i = b_i^\dagger b_i$, $\sigma_+ = b^\dagger$, $\sigma_- = b$, $\sigma_i^x = b_i^\dagger + b_i$ are the operator transformations used and $\Omega_{d,i}, D_i(t)$ being qubit-drive parameters. Similarly, but with more detailed structure with included coupling, the 2-qubit Hamiltonian as defined by the IBMQ backend is[12]

$$\begin{aligned}\mathscr{H} = &\sum_{i=0}^{1}\left(\frac{\omega_{q,i}}{2}(\mathbb{I} - \sigma_i^z) + \frac{\Delta_i}{2}(O_i^2 - O_i) + \Omega_{d,i}D_i(t)\sigma_i^x\right)\\ &+ J_{0,1}(\sigma_0^+\sigma_1^- + \sigma_0^-\sigma_1^+)\\ &+ \Omega_{d,0}(U_0^{(0,1)}(t))\sigma_0^x + \Omega_{d,1}(U_1^{(1,0)}(t))\sigma_1^x.\end{aligned} \tag{141}$$

It is important to note that these are approximate forms of qubit Hamiltonians, which are claimed by the hosts of the devices under the assumption that they describe the dynamics accurately enough for the operation of the device. This is an important factor which the present work focusses on, to evaluate the validity of this approximation in accurately describing qubit dynamics.

Furthermore, through the use of conventional experiments described in previous sections, the devices are regularly calibrated to present the most recent parameters of the devices for each qubit, including values of each qubit frequency, anharmonicity, gate error, readout error, and T_1 & T_2 relaxation and decoherence times. The devices are also kept in dilution refrigerators to maintain the superconducting temperature requirements of the devices, at a claimed temperature of approximately 15 mK, although this is not included in the calibration procedures. These are meant as indicators of device performance, with the coherence times and errors being optimised with each new device introduced to the ensemble. These parameters are extracted through simple experiments, such as T_1 and T_2 measurements, which do not typically account for all of the external sources of noise influencing these dynamics.

The present work goes into detailed investigation of the accuracy of these calibrations, as well as probing extra factors which are not included in the approximate forms of the parameter extractions used in the device calibration. The investigations included here are performed on multiple backend devices across multiple architecture iterations, to investigate which behaviours are not being accounted for in the advancement of the IBMQ family of quantum computers.

The Hamiltonians in (140) and (141) can be simplified to

$$\mathscr{H} = \frac{\omega_0}{2}\sigma^z, \tag{142}$$

$$\mathscr{H} = \frac{\omega_0}{2}\sigma_0^z + \frac{\omega_1}{2}\sigma_1^z + J_{0,1}\left(\sigma_0^+\sigma_1^- + \sigma_0^-\sigma_1^+\right), \tag{143}$$

for shallow quantum circuits where the anharmonicity and driving parameters do not have the opportunity to make any significant difference. These Hamiltonians have a clear assumption concerning the axes involved in the definitions of the parameters, in that they are rigid along each axis involved, meaning that the qubit frequency is assumed to only have a component along the z-axis, and the jump operators of the coupling are assumed to flip the qubit Bloch-orientations perfectly and only along one direct axis of coupling.

[12] In this example, the i index is dropped as the equation is referring to a single qubit so indices aren't necessary.

A more generalised form of these Hamiltonians needs to be investigated to uncover any underlying deviations from the initial assumptions. For the single-qubit case, this generalised Hamiltonian has the following form,

$$\mathscr{H} = \frac{1}{2}\left(\vec{\omega}\cdot\vec{\sigma}\right), \qquad \text{where} \qquad \vec{\omega} = \begin{pmatrix}\omega_x\\ \omega_y\\ \omega_z\end{pmatrix} \quad \& \quad \vec{\sigma} = \begin{pmatrix}\sigma^x\\ \sigma^y\\ \sigma^z\end{pmatrix}. \tag{144}$$

Similarly, for the two-qubit case, there are terms for each qubit, denoted by subscripts, and can be expressed as

$$\mathscr{H} = \frac{1}{2}\left(\vec{\omega}_0\cdot\vec{\sigma}_0\right) + \frac{1}{2}\left(\vec{\omega}_1\cdot\vec{\sigma}_1\right) + \vec{\sigma}_0\mathbf{J}\vec{\sigma}_1, \tag{145}$$

where the new *coupling matrix* term is defined as

$$\vec{\sigma}_0\mathbf{J}\vec{\sigma}_1 = \begin{pmatrix}\sigma_0^x & \sigma_0^y & \sigma_0^z\end{pmatrix}\begin{pmatrix}J_{xx} & J_{xy} & J_{xz}\\ J_{yx} & J_{yy} & J_{yz}\\ J_{zx} & J_{zy} & J_{zz}\end{pmatrix}\begin{pmatrix}\sigma_1^x\\ \sigma_1^y\\ \sigma_1^z\end{pmatrix}. \tag{146}$$

This is a far more inclusive description of the qubit Hamiltonian as it will give insight into the behaviour of the qubits which is not limited to the ideal axes, but rather includes external influences which can give insight into possible noise sources which are not accounted for. The Hamiltonian is worth this much focus and investigation as it plays a crucial role in the modelling of the qubit dynamics for this investigation. The framework used here is that of Markovian master equations in open quantum systems, to investigate the claims of the device operations being intrinsically Markovian despite the findings of recent literature, as in Section 5.3, demonstrating the opposite.

This framework additionally allows for the extraction and verification of more claimed qubit parameters from the calibration metrics, such as the relaxation and decoherence times, as well as an extraction of information not included in the calibration, such as the qubit temperatures. These capabilities are all included in the GKSL master equation, which for this application is expressed, for a single-qubit, as

$$\begin{aligned}\frac{\mathrm{d}}{\mathrm{d}t}\rho = &-i\left[\mathscr{H},\rho\right] + \gamma\left(\langle n\rangle + 1\right)\left(\sigma^-\rho\sigma^+ - \frac{1}{2}\left\{\sigma^+\sigma^-,\rho\right\}\right)\\ &+ \gamma\langle n\rangle\left(\sigma^+\rho\sigma^- - \frac{1}{2}\left\{\sigma^-\sigma^+,\rho\right\}\right) + \gamma_z\left(\sigma^z\rho\sigma^z - \rho\right),\end{aligned} \tag{147}$$

where γ is the emission coefficient, and acts as an inverse of the relaxation and decoherence times, and $\langle n\rangle$ represents the average number of photons emitted as the density matrix evolves, which is represented by

$$\langle n\rangle = \frac{1}{e^{\hbar\omega/k_BT} - 1}. \tag{148}$$

This encapsulates the ideal Markovian dynamics of the system, even at absolute zero, and allows for the extraction of decay times through the emission coefficient and temperature through the photon number. For the N-qubit case, the expression is extended to include the density matrix evolution for each qubit, expressed as

$$\begin{aligned}\frac{\mathrm{d}}{\mathrm{d}t}\rho = -i\left[\mathscr{H},\rho\right] + \sum_{i=0}^{N-1}\Bigg[&\gamma_i\left(\langle n_i\rangle + 1\right)\left(\sigma_i^-\rho\sigma_i^+ - \frac{1}{2}\left\{\sigma_i^+\sigma_i^-,\rho\right\}\right)\\ &+ \gamma_i\langle n_i\rangle\left(\sigma_i^+\rho\sigma_i^- - \frac{1}{2}\left\{\sigma_i^-\sigma_i^+,\rho\right\}\right)\\ &+ \gamma_{z,i}\left(\sigma_i^z\rho\sigma_i^z - \rho\right)\Bigg].\end{aligned} \tag{149}$$

The emission coefficient γ_z represents the process of pure dephasing (Figure 5b). For these multi-qubit descriptions, it is worth reiterating the process of extending to larger qubit operators, such as the Pauli matrices, σ_i, as the action of an operator, $\hat{O}$, on a specific qubit is expressed as the tensor product,

$$\hat{O}_i = \underbrace{\mathbb{I}}_{0} \otimes \underbrace{\mathbb{I}}_{1} \otimes \cdots \otimes \underbrace{\hat{O}}_{i} \otimes \cdots \otimes \underbrace{\mathbb{I}}_{N-1}, \tag{150}$$

where the qubit index, i, represents the placement of the operator in the chain of tensor products.

Now that the framework for describing qubit evolution has been established, the actual channels of evolution can be described. The present work focusses on a handful of simple conventional quantum noise channels, as well as modifications to these, typically used to describe the T_1, T_2, and T_2^* decay times. The act of measurement is indicated by the final gate in each circuit, which converts the quantum state to a classical register indicated by the double line at the bottom of the circuit.

The T_1 relaxation time is the simplest of the sequences, as depicted in (QC1), and consists in this case of a qubit, or set of n qubits, being initialised in the $|0\rangle^n$ state, after which a set of X^n gates is applied to excite the qubits to the $|1\rangle^n$ state. After this excitation, the qubits are left to decay for a variable time, here set to be a period of 296 µs, after which the states are measured in the computational basis and the state distribution calculated.

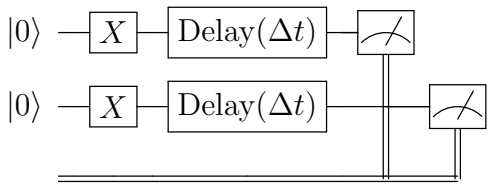

(QC1)

For the T_2 procedure, the Hahn echo sequence [64] is used, depicted in (QC2), which consists of a set of n qubits being initialised in the $|0\rangle^n$ state, after which a set of $\pi/2$ rotations is applied, around the x- or y-axis. Succeeding this is a delay period of variable time followed by a π rotation around the same axis as the first rotation, and then another delay time of the same period, and a final $\pi/2$ rotation in the same direction to return the state to $|0\rangle^n$ where it can be measured.

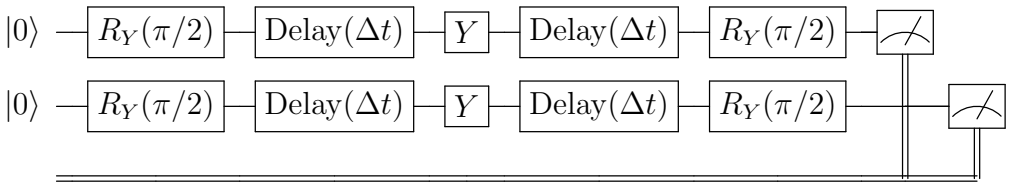

(QC2)

The T_2^* procedure, shown in (QC3), consists of the qubit set again being initialised as $|0\rangle^n$, after which a $\pi/2$ rotation is applied, in this case through the Hadamard gate, H, to the $|+\rangle$ state. After this the state is left to undergo pure dephasing for a variable time period, after which another Hadamard operator is applied to return the qubits to the $|0\rangle$ state where they can be measured. It should be noted that a Hadamard operation is hermitian, $H = H^\dagger$, meaning that the second Hadamard gate completes the rotation around the $x + z$ axis to reorient the dephased qubit, rather than rotating it to the $|1\rangle$ state, which would occur with two sequences of other rotation gates, such as $R_X(\pi/2)$.

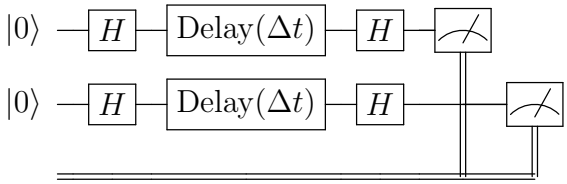

(QC3)

These procedures are extended uniformly across the various qubit sizes involved in the experiments, namely ensembles of 1, 2, and 3 neighbouring qubits. The fact that the investigated qubits are neighbours means that their direct coupling strength may lead to stronger interference between them. Though this phenomenon is necessary for multi-qubit gates, which is a reason why they are coupled at all, there may be inadvertent effects of this coupling creeping into isolated channels of individual qubits. To investigate this possibility further, the following two-qubit sequences are adapted from the original procedures described above.

The first modified sequences are made through changes to the T_1 experiment, which was initialised as $|00\rangle$, and excited by simultaneous X gates before the relaxation period. This procedure has the qubits mimic each others effects, which makes it difficult to detect the presence of coupling phenomena between them as their behaviour is indistinguishable from a scenario wherein they are coupled. This is circumvented by performing the experiments not only with the simultaneous excitation, but also with quantum circuits wherein only one of the qubits is excited through an X gate and the other is left to evolve from the $|0\rangle$ state, as in (QC4).

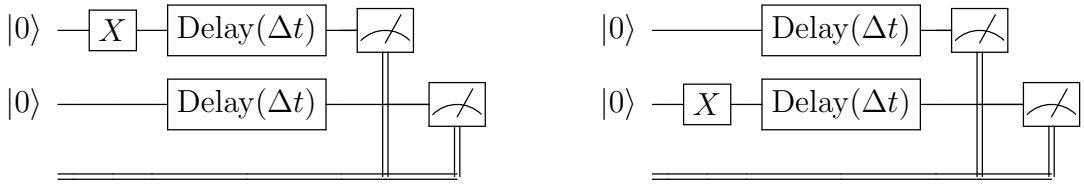

(QC4)

If the coupling is strong enough and not shielded in some way, then the decay of the excited qubit will directly influence the stationarity of the other. By performing the experiment with the exclusion of excitation operators entirely, shown in (QC5), the qubits are left in the ground state to idle for the delay period to investigate if there are any external sources which unintentionally excite the subsystem of qubits.

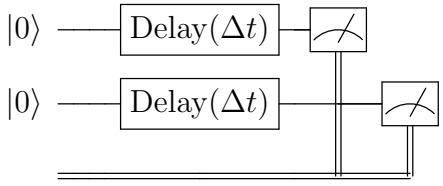

(QC5)

To provide further insight into the relaxation and decoherence mechanisms of the qubits, the procedures described before can be combined into new composite systems to show the dynamics between various decay mechanisms, and how the decay of one qubit in the system might influence its neighbours which are ideally excluded from the subsystem. To achieve these, the 2-qubit ensemble is modified into new quantum circuits, the first of which has one qubit undergoing a standard T_2^* experiment, while its neighbour undergoes a T_1 experiment, having the first H gate replaced by an X gate and the second H replaced by an identity gate, I, illustrated in (QC6).

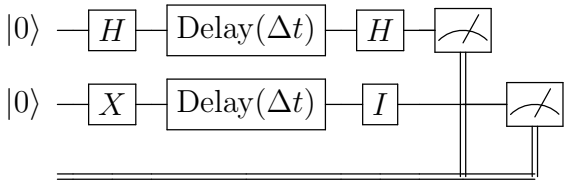

(QC6)

Similarly, the other modified circuit has the first qubit undergo a T_2^* sequence, while the neighbour qubit simply stays in its idle state from the $|0\rangle$ initial state, as shown in (QC7).

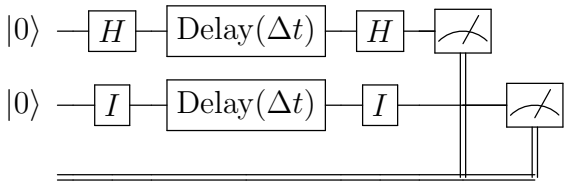

(QC7)

All of these circuits return a set of average state distributions for each time step and show how the states evolve through these different scenarios. To elucidate what should happen from the theoretical standpoint, it is necessary to return to the master Equation (149). This equation is very complicated to solve analytically, so numerical methods must be used to obtain useful information. The details will be discussed in the next section. A solution for this equation can be found for a set of parameters, $\vec{x}$, which is dependent on the form of the master equation and the Hamiltonian used. For example, the single-qubit master equation solution with the simple Hamiltonian (142) is a function of 5 parameters,

$$\vec{x} = (t, \omega, \gamma, \gamma_z, T)\,, \tag{151}$$

being time, qubit frequency, emission rate, and temperature. However for the general Hamiltonian (144), the solution is a function of 7 parameters,

$$\vec{x} = (t, \omega_x, \omega_y, \omega_z, \gamma, \gamma_z, T)\,. \tag{152}$$

The size of the parameter vector quickly grows for multi-qubit states, as in the example of a 2-qubit subsystem, the solution will require 10 parameters for the simple Hamiltonian (143), and 22 parameters for the generalised Hamiltonian (145). Nonetheless, these equations can be numerically solved as a function of these parameters and initial states from the qubits at the start of the delay period, to return a time-series of the evolution of the density matrix. The solution of the master equation can be expressed as the integral of

$$\frac{\mathrm{d}}{\mathrm{d}t}\rho(t) = \mathscr{L}(t)\rho(t) \qquad\qquad \rho_0 = \rho(t=0) = |1\rangle\langle 1|\,, \tag{153}$$

in the case of the single-qubit T_1 sequence, where the system starts in the state $|0\rangle$ and is excited to $|1\rangle$. This evolution through the delay periods in the quantum circuits can be combined with the quantum gates as operators in the construction of the quantum channels to describe the entire evolution of the system. For example, in the single-qubit T_1 experiment, the delay period will be described by a master equation solution $\rho_d(t)$, and the excitation gates are Pauli X-matrices, σ^x, so the quantum channel is described by

$$\mathscr{E}(\rho) = \sigma^x \rho_d(t) \sigma^x. \tag{154}$$

The full solution of the master equation for a set of parameters which is passed through the Kraus form of the quantum channel is then a set of values which are comparable to the experimental

results which are obtained through the respective quantum circuit. Through the use of the parameters provided by the periodic device calibration, the master equation solution can be compared directly to the experimental results to verify the accuracy of the calibration data. This verification process allows for all of the hardware parameters to be verified in conjunction with one another, rather than the independent experiments which were used to extract those values initially.

Furthermore, this method provides the capability to improve upon the parameter extraction in the case that the claimed parameters do not match the experimental observations. The parameters used in the master equation solution can be iteratively varied to provide different results, until a parameter set is found which accurately matches the experimental data. This means that the parameter set can be optimised for the smallest difference between the numerical and experimental results.

This can be achieved very easily through conventional optimisation methods which have shown extreme success in achieving this form of outcome. For example, this method is used extensively in the field of machine learning, where the learning model needs to have its parameters varied to match the dataset which it is learning, thereby increasing its predictive accuracy. The optimisation method used to achieve this, and which is used in this work, is *gradient descent*. This is an iterative algorithm to find the minimum point of a differentiable function, through finding the steepest path towards this minimum through calculating the negative gradient of the function which finds the direction of the fastest change in the function, for a fixed step-size α,

$$f_{n+1} = f_n - \alpha \nabla f_n. \tag{155}$$

As the master equation solution is a function of multiple parameters, $\vec{x}$, the gradient operator has the form of a Jacobian vector, which partially differentiates the function with respect to each parameter for each vector component,

$$\nabla f(\vec{x}\,) = \left(\frac{\partial f}{\partial x_1}, \frac{\partial f}{\partial x_2}, \cdots, \frac{\partial f}{\partial x_n} \right). \tag{156}$$

The function which needs to be minimised in this procedure is a measure of how different the current master equation solution is from the experimental data, since the ideal solution will have the minimum difference of zero. A conventional measure of this is the *least-squares* function, which sums all of the squared values of the difference between each observed and estimated data point,

$$S = \sum_{i=1}^{n} \left(y_i - f_i(\vec{x}\,) \right)^2, \tag{157}$$

where y_i are the experimental values.

In this form, the method for optimising this function is very inefficient and prone to error due to the complicated solution landscape created by the many parameters. This means that there are many local maxima and minima for the algorithm to misidentify as the global maxima and minima. In this work, the more sophisticated and accurate gradient-descent method of the Adaptive Moment Estimation (Adam) optimiser [65] is used. The details of this algorithm are elucidated in Appendix A.1, but the principal idea is to have an adaptive step-size through momentum, so that the initial descent is fast and slows down to be more accurate as the function minimum is approached.

Using this method to find the minimum difference between the numerical and experimental results yields a set of parameters which more accurately describe the properties of the qubits being operated on. The extraction of these parameters not only allows for a new method of calibrating the device, but also gives insight into the way that they are influenced by different experiments and quantum circuits.

Now that the tools used in this work have been introduced and described, the next section will discuss how they are applied experimentally and demonstrate the results obtained through this application.

6.2 Experimental Procedure and Results

Communication with the quantum devices is done through the Qiskit SDK, which allows for the extraction of backed configuration information, as well as the construction of quantum circuits which are converted to basis gate circuits to perform the experiments. Once these circuits are run, the data can be extracted and used as desired. Qiskit also offers many built-in functionality such as readout error mitigation and state tomography procedures.

Qiskit allows for a selection of several backend devices to be worked with, and for each offers a set of calibration data as well as device properties such as the qubit topology. This information was used in this work as the parameters of the numerical solutions to verify the accuracy of the calibrations performed on the backend side. This information also provided scales of extra errors, such as readout and gate errors, which could be accounted for in analysing the data.

This work made extensive use of the *ibmq_armonk* v2.4.23 device for single-qubit experiments, as well as the *ibmq_santiago* v1.3.40 and *ibmq_manila* v1.0.19 devices for multi-qubit circuits as these devices have 5 qubits each. These devices are examples of IBM's Canary and Falcon architectures, respectively. The topology of these devices is a simple linear structure, as in Figure 6, and allows for the investigation of coupling effects between neighbours.

Once the backend was selected the circuits could be constructed. The circuits introduced in the last section needed to be modified slightly to obtain useful data. Due to the nature of quantum measurement, the state distribution could not be continuously measured, otherwise the Quantum Zeno Effect [66] would alter the data completely by not allowing the system to undergo the desired decay. This means that running the circuits as presented, (QC1) for example, would return only one time-slice of the data and the bit-string probability distribution at that snapshot in time. To avoid this, a series of circuits needed to be constructed and run with the delay time being varied to allow for each time step to be a new point in the dataset. For this experiment, the delay time was varied through a period of 0 s to 296 µs in steps of 4 µs for a total of 75 quantum circuits corresponding to as many data points.

In the execution of these experiments there are unavoidable errors in the process which detract from the fidelity of the desired experimental results. These errors are primarily SPAM errors of readout and gate execution, which are not important in the present investigation but plague the data nonetheless. These errors must be accounted for to obtain meaningful data. The gate errors are avoided by using time-scales small enough for the gate execution times to be insignificant, and the actual errors are combatted by statistical rigour. As mentioned in previous sections, the probabilistic nature of quantum systems demands that experiments and measurements be made multiple times to create an ensemble with a reliable probability distribution from which average values can be extracted. In this experiment each experiment was run for 8 192 iterations, which is the maximum number allowed by IBMQ, which ensures that the variance between experiments is reduced enough to avoid the influence of outlier gate

Figure 6: Qubit topology of 5-qubit *ibmq_santiago* v1.3.40 and *ibmq_manila* v1.0.19 devices. The colours of the qubits represent the frequency, with darker meaning a lower frequency and lighter meaning a higher value.

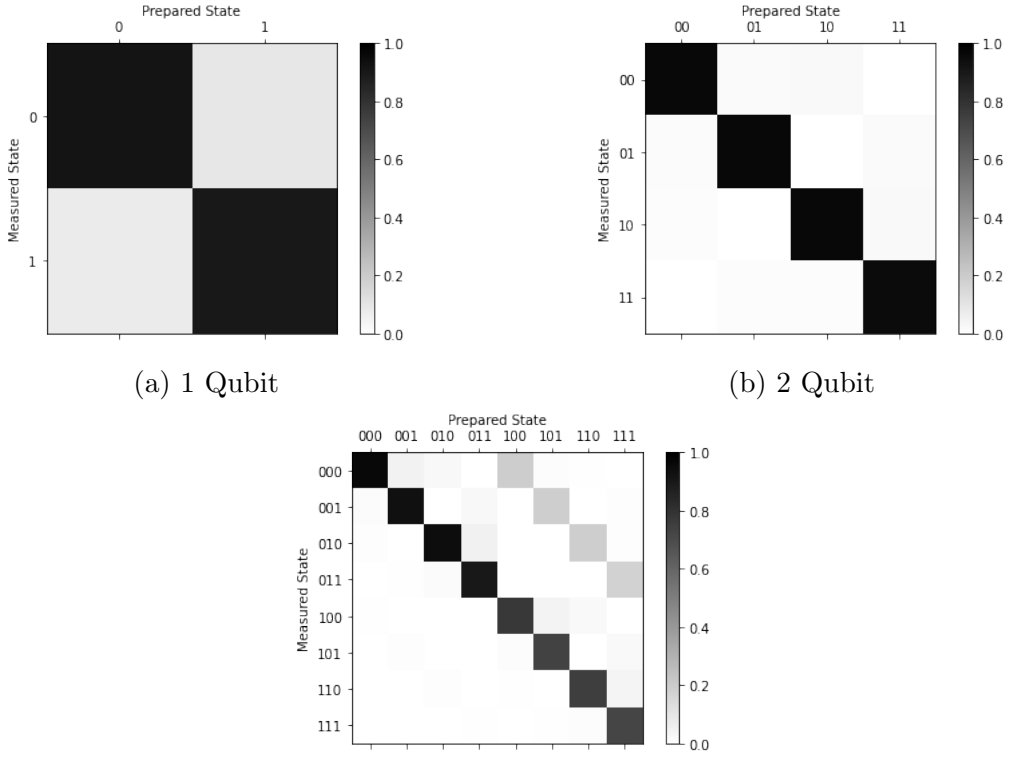

(a) 1 Qubit

(b) 2 Qubit

(c) 3 Qubit

Figure 7: Calibration matrices for readout errors. The single-qubit calibration produced a fidelity of 0.912 (a). The 2-qubit calibration produced a fidelity of 0.965 (b). The 3-qubit calibration produced a fidelity of 0.843 (c).

errors.

The readout errors, however, are present throughout the device and cannot be avoided through collecting more data for each experiment, but rather need to be calibrated for within the experimental run of executing all of the circuits. The measurement calibration functionality built into Qiskit follows a procedure of preparing all of the qubits in the system, or a defined subsystem, in a certain state, which in this case is similar to tomographic methods in that it produces all possible states, and measuring immediately afterwards. This produces a state distribution demonstrating the accuracy of the readout, which can be compared to the ideal case where the outcome from such an experiment is known analytically. Combining all of the ideal states into a measure of fidelity would produce a 2^n-dimensional identity matrix for n qubits, representing the baseline of the readout accuracy. The measurement of the experimental tomography results in a matrix close to the identity but with off-diagonal contributions where the incorrect state was measured, as in Figure 7.

All of these fidelity measures and measurement values allow for the construction of a transition matrix, M, which can compare the measured and ideal state distribution vectors, V, such that

$$V_{\text{noisy}} = MV_{\text{ideal}}. \tag{158}$$

With this transition matrix calculated, the system can be calibrated to counter the readout errors through the application of this matrix to all of the state distributions measured. For example, in the case of the T_1 experiments, the error mitigation changes in Figure 8 were made for the initial value. Now that the procedure for extracting accurate experimental results has been discussed, the stage has been set for the other half of the experiment where the numerical results are calculated and can be compared to measured data.

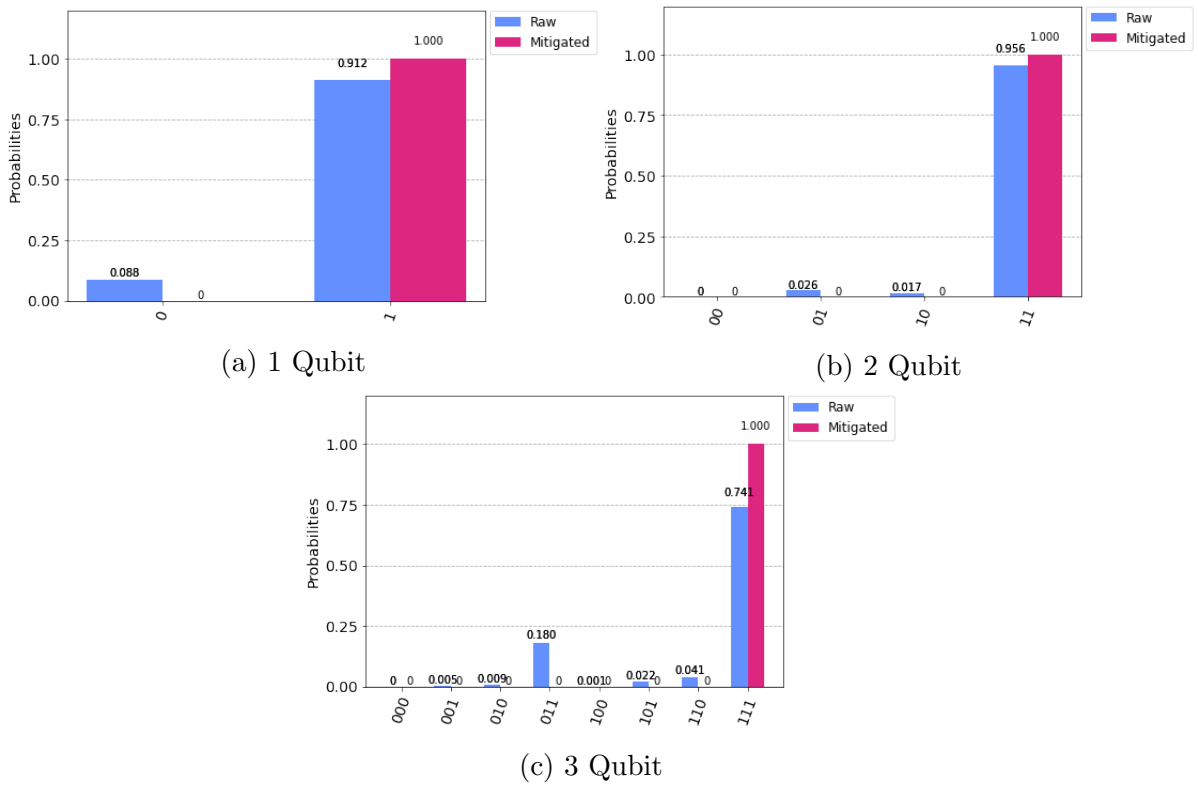

(a) 1 Qubit

(b) 2 Qubit

(c) 3 Qubit

Figure 8: Error mitigation for readout errors. The results of applying the error mitigation scheme are shown for the 1-qubit (a), 2-qubit (b), and 3-qubit (c) cases, where the blue bars show the initial fidelity from experimental measurements and the pink bars show the corrected measurements where readout errors have been accounted for.

As the numerical procedure of calculating the master equation solution and optimisation algorithm is heavily based on calculus, the JAX SDK [67, 68] was used as it provides substantial increases in numerical performance particularly through its auto-differentiation and Just-In-Time (JIT) Compiler features which assist in calculus based and iterative calculations.

The first numerical procedure is that of solving the master equation (153), which is performed through the built-in JAX function "ODEint" designed to integrate ordinary differential equations (ODEs), through an algorithm further explained in Appendix A.2. This method takes in an initial state density matrix which describes the $|0\rangle^n$ state and all of the operations performed on it before the delay period begins which is the time evolution that the master equation describes. The method returns a $75 \times 2^n \times 2^n$ array containing the 75 snapshots of the density matrix, of which the diagonal elements represent the observed states which can be measured experimentally. The parameters for the master equation solution were taken directly from the hardware configuration data from Qiskit for the most accurate comparison.

From these results, it can be seen that the claimed hardware parameters do not typically produce the same qubit dynamics as what is experimentally observed, although they are quite similar hinting at the model being correct but the parameters being inaccurate. This demonstration of inaccurate configuration claims further reinforces the need for a method to find the correct values which match the observed behaviours.

To apply the optimisation algorithm to find the correct parameters, the Adam optimiser was used based on the Jacobian vector of parameters and a least-squares function created to find the difference between each data point from the experimental dataset and the numerical calculations. The optimiser was run typically with an initial step-size of $\alpha = (0.01, 0.1, 1)$, depending on the initial conditions of how different the functions were from each other. Similarly, the algorithm was run for a total number of iterations ranging from 200 to 500 depending on

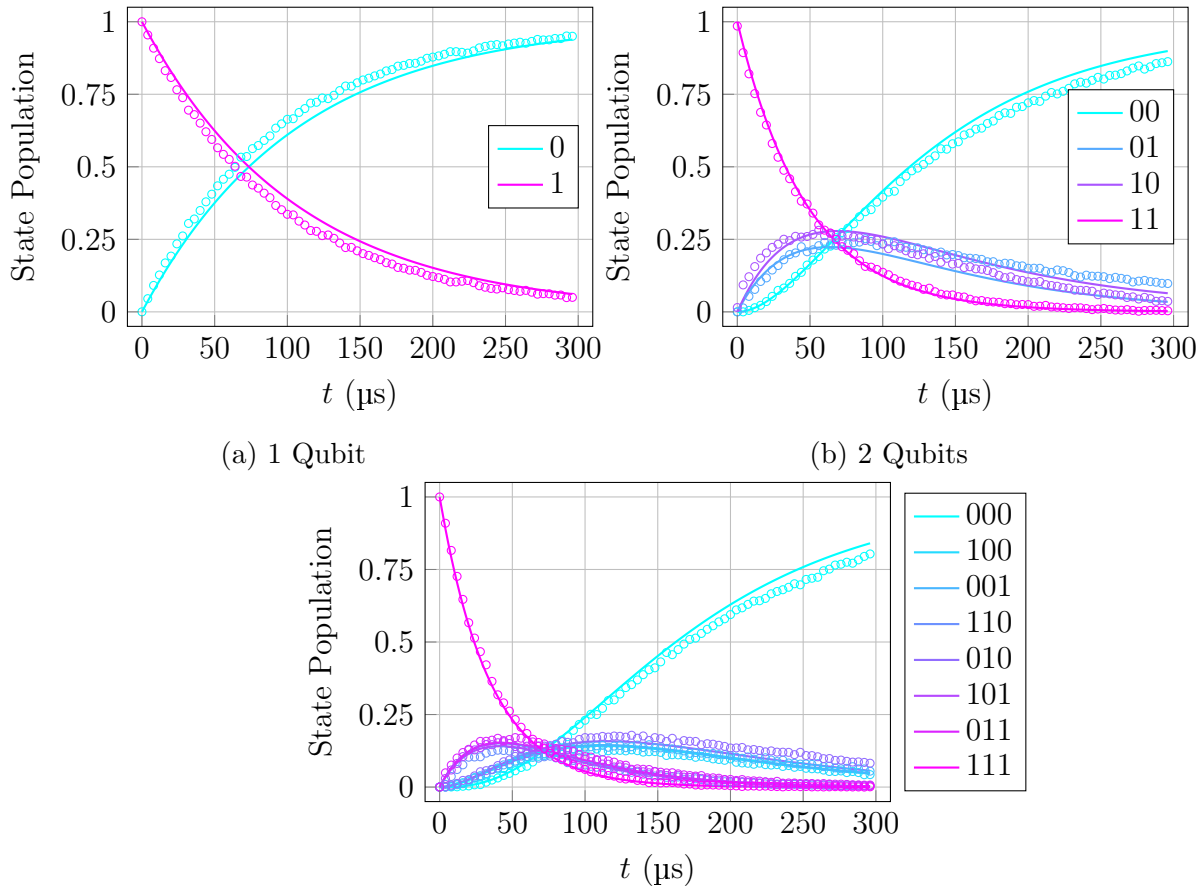

(a) 1 Qubit

(b) 2 Qubits

(c) 3 Qubits

Figure 9: T_1 relaxation density matrix evolution. Experimental data represented by dots and numerical data for claimed hardware parameters represented by solid lines. Results shown for 1-qubit (a), 2-qubit (b), and 3-qubit (c) cases.

the case. The initial parameter set for the optimisation was usually the claimed hardware parameters. However, in the cases where the initial datasets were too different, the Adam optimiser could not obtain the optimal result in one application, and so was run multiple times in some cases, using each previous attempt's optimal parameters as the initial set.

In the application of the optimisation algorithm, there was a notable discrepancy in its effectiveness depending on the quantum channel it was applied to. For example, across all of the T_1 sequences, irrespective of the system size, the optimisation always found excellent fits, with least-squares errors being minimised to values on the order of $\sim 10^{-3}$. This indicates as good of a fit as could be desired with the only differences between the numerical and experimental results being random fluctuations due to the nature of the experimental procedure measuring 75 sequential sub-experiments rather than a single sequence. A demonstration of these optimised results is depicted in Figure 10.

In order to further investigate the behaviour of the T_1 sequence, particularly in terms of the coupling between multiple neighbouring qubits, the modifications of the sequence using different initial states, as in the circuits (QC4), the same process of circuit compilation, execution, and fitting was followed. The results obtained by these verified the stability and isolated nature of this simple relaxation sequence, as can be seen in Figure 11. The data show an expected behaviour of the inter-qubit coupling not influencing the Markovianity of the system evolution, which is seen in the ground-state qubits staying in the ground state through the full period, while the excited state population follows a simple exponential path to equilibrium.

Although the T_1 sequences for all of the qubit sizes and initial states proved to be very

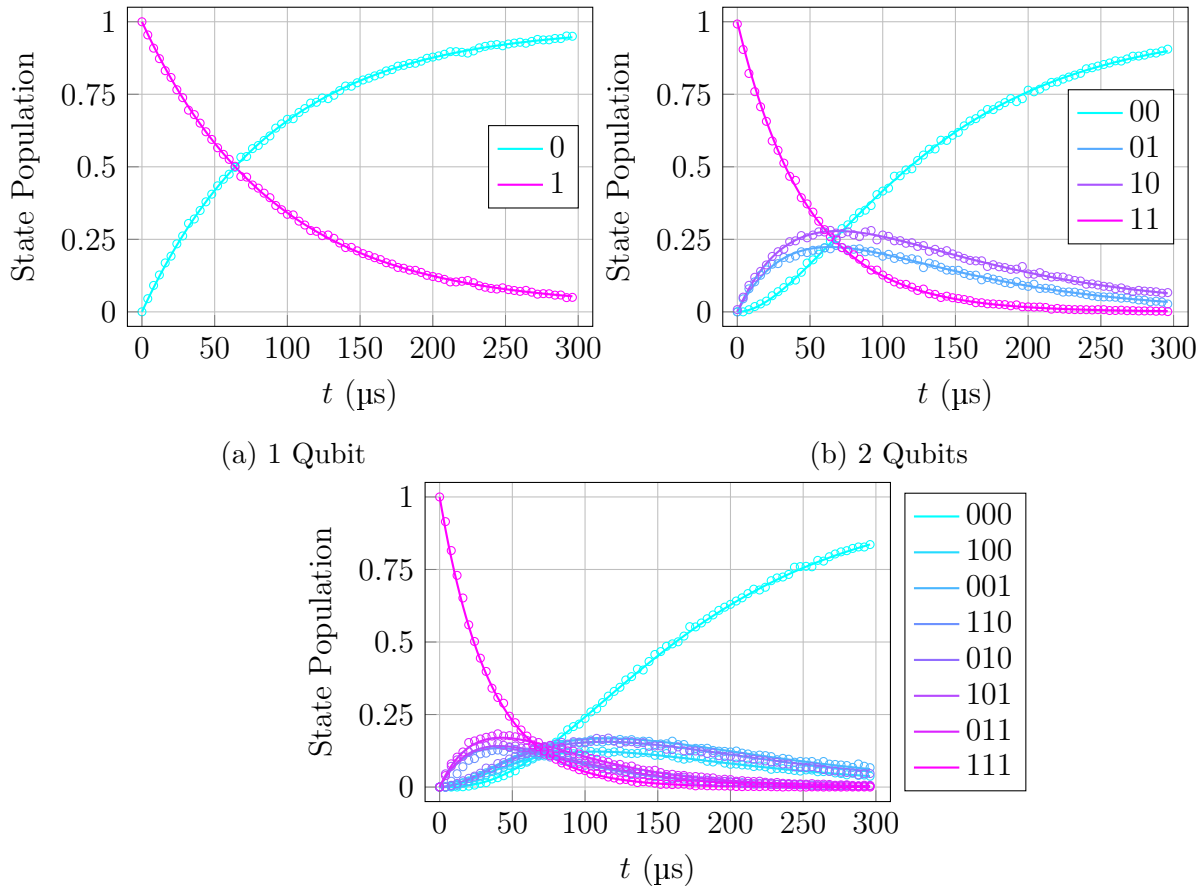

(a) 1 Qubit

(b) 2 Qubits

(c) 3 Qubits

Figure 10: Optimised T_1 relaxation density matrix evolution. Experimental data represented by dots and numerical data for optimised parameters represented by solid lines. Results shown for 1-qubit (a), 2-qubit (b), and 3-qubit (c) cases.

stable and reliable, the rest of the experiments provided more intricate results. For a first example, the T_2 sequence for a single-qubit proved to be a significantly more difficult numerical procedure, taking far longer to calculate the results despite the simple appearance of exponential decay, as seen in Figure 12a. Despite the difficulty in extracting numerical solutions and finding optimal parameters, the procedure still found great success in achieving these goals. The optimal parameters provided a very accurate fit, similarly to the T_1 outcome, having a least-square error on the level of $\sim 10^{-2}$ consistently.

In the 2-qubit case of the T_2 sequence, the results obtained show a more intricate behaviour, particularly in the combined forms of exponential decay and oscillatory forms, which offer more room for error to be identified in noisy systems. Despite this, the numerical results closely match the experimental outcome and display only a slight deviation from the claimed parameters which makes for a relatively simple optimisation procedure to offset the computational demand of the optimisation itself. This particular part of the project highlighted a slight unforeseen error in the execution of the quantum circuits, as the time-scale and component time steps exhibit a constant scaling factor of 1.3, meaning that rather than the ideal 592 µs period the procedure amounted to ≈ 769.6 µs overall. Each time step had this scaling phenomenon and it occurred consistently throughout every attempt at the experiment, which leads to the suspected phenomenon of an error in the compilation of the circuit when converting the gate-based formalism to pulse sequences and ensuring compatible scheduling. With this being the source of the behaviour, there is no significant impact on the results obtained as the numerical results simply need to be scaled to match this time scaling, as is confirmed by the accuracy of the results obtained by the

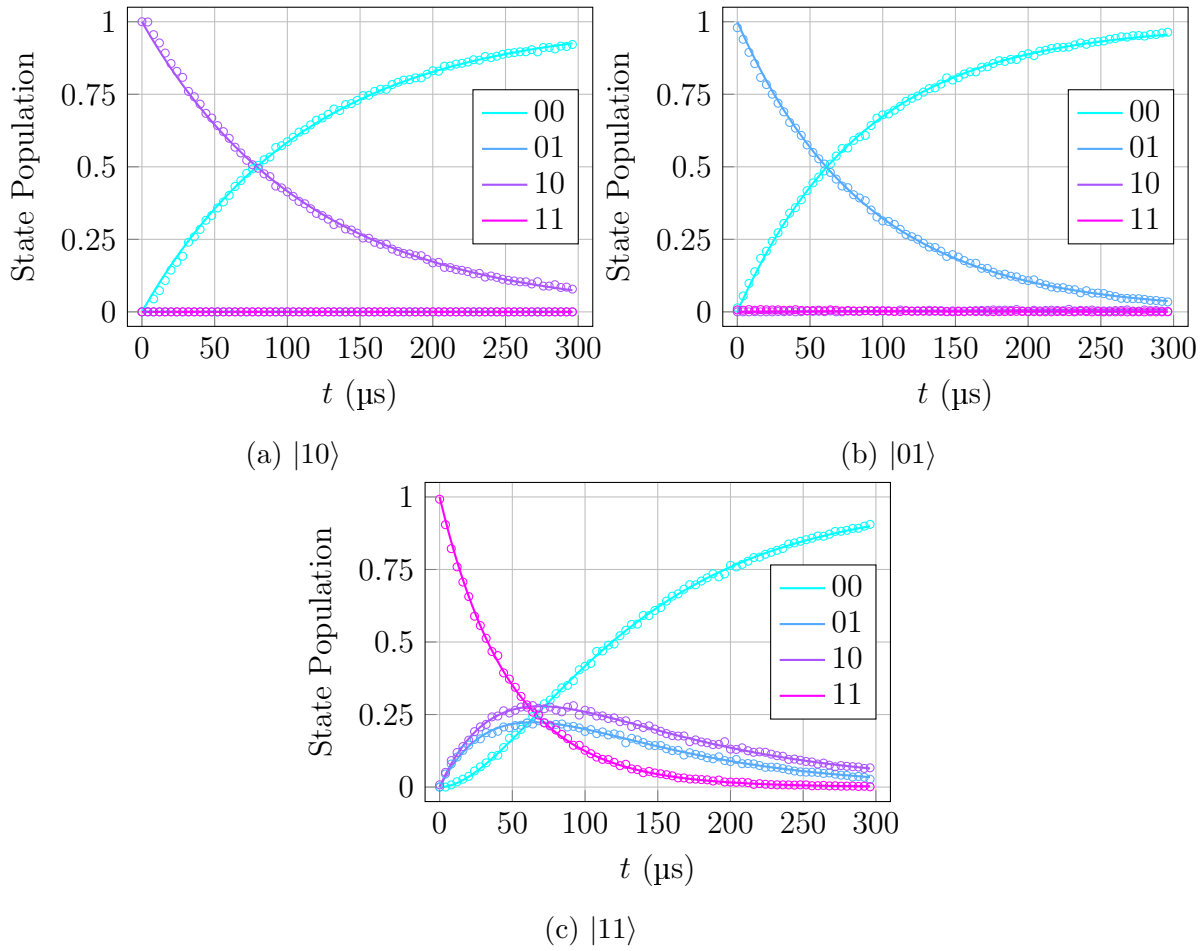

(a) $|10\rangle$ (b) $|01\rangle$

(c) $|11\rangle$

Figure 11: Optimised T_1 relaxation density matrix evolution for varied initial conditions. Experimental data represented by dots and numerical data for optimised parameters represented by solid lines. Results shown for initial states $|10\rangle$ (a), $|01\rangle$ (b), and $|11\rangle$ (c).

optimisation sequence, seen in Figure 12b.

A similar pattern is present in the 3-qubit case of the T_2 sequence, with a similar style to the 2-qubit case in having damped oscillations as well as gentle exponential curves to the asymptotic equilibrium state. The attempts of this experiment did suffer the general difficulty in extracting high-fidelity results from 3-qubit experiments. However, in the cases where the data were well behaved and reliable the results fitted the expected dynamics from which optimised parameters could be extracted. The nature of 3-qubit sequences being more difficult to reproduce in repeated attempts of the experiment further emphasises the versatility and usefulness of the single-qubit dynamics which can be used to predict larger subsystem dynamics as well, as will be seen later.

The results of the T_2^* sequences proved to be the least reliable results of the ensemble, exhibiting a lot of stochastic errors throughout the experiments which could not be described by the numerical modelling. This is not to say that the results are necessarily non-Markovian, but rather that the sequences themselves were subject to errors and deviations between each time step, as the experimental procedure could not observe the evolution of one state from start to finish as the measurement of the quantum state collapses its wave-function, but rather comprising 75 experiments, each providing a snapshot of the time step of interest. This procedure relies heavily on the assumption that each replication of the experiment undergoes the same behaviour, which holds well for all of the previously mentioned sequences, however not here. This can be seen in Figure 12c, where the optimal numerical modelling of the procedure with the best parameters still only roughly mimics the experimental results, with the fit becoming worse for later time steps where more random errors are prevalent, creating unpredictable jumps

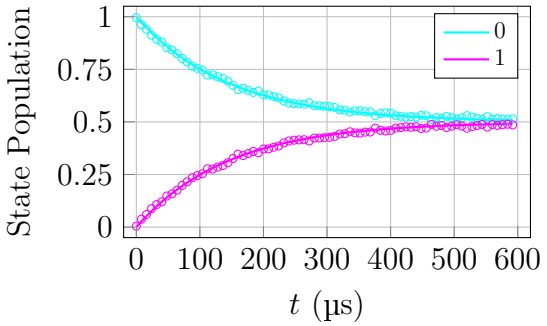

(a) single-qubit T_2 sequence.

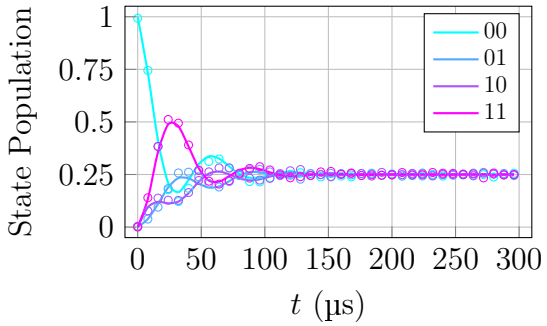

(b) Optimised T_2 sequence for 2 qubits.

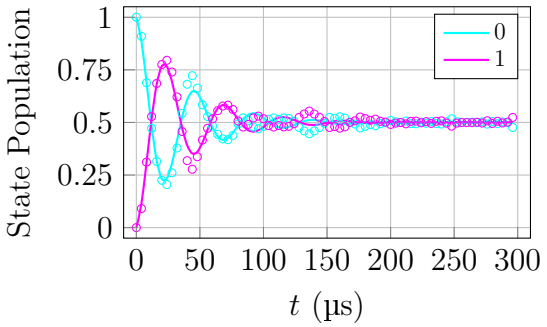

(c) Optimised T_2^* sequence for 1 qubit.

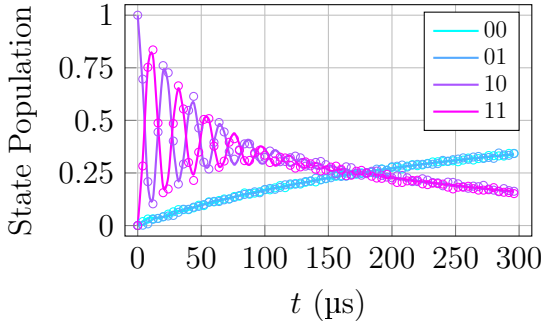

(d) Optimised combination of T_2^* and T_1 sequences for 2 qubits.

Figure 12: Optimised results for additional experimental circuits, including T_2, T_2^*, and combined procedures. Experimental data represented by dots and numerical data for optimised parameters represented by solid lines. Results shown for single-qubit T_2 sequence (a), 2-qubit T_2 sequence (b), single-qubit T_2^* sequence (c), and 2-qubit combination of T_2^* and T_1 sequences (d).

in the curves. In some evaluations of the experiment the results were well behaved as expected, as in the figures displayed here, while in others the results are speculated to be scaled by some sinusoidal function of a constant angle scaled by time. This leads to the speculation that in some part of the calibration or measurement of the quantum devices, there is some slight offset which is not accounted for in the error mitigation schemes.

This erratic behaviour is seen throughout the modifications to the T_2^* sequence, but most clearly in the single-qubit case where the experiments were run on a device with only one qubit, so any external factors could be explicitly seen. The influence of this suspected SPAM error seems to manifest in providing some oscillatory factor while also exaggerating the peaks and troughs of existing oscillations, which can be seen, albeit in a less evident form, throughout the 2-qubit examples. In the case of a 3-qubit version of this sequence, the results are far less reliable, as the fluctuations in the trajectories of each of the 8 states quickly overwhelm any expected behaviour and blend into being all within the same range. This poses a problem as this equilibrium state is reached too rapidly for there to be any clear indication of which results are fluctuations and which are following the correct path, especially considering that the readouts of the values over a set of 8 192 iterations of the sequence means that the fluctuations are still on the scale of the variance between iterations.

This is fortunately not the case for other sequences on the 3-qubit scale, but still limits the focus of the results to the 1- and 2-qubit cases. Furthermore, in the case of the T_2^* sequences and modifications thereof, there were not any claimed parameters of the T_2^* time for the qubits accessible through calibration data, as only T_1 and T_2 times were included there, which typically matched fairly well to the experimental results but still warranted the optimisation process. Thus, in the optimisation of the T_2^* numerical results, the T_2 parameters were used as initial

conditions, but lead to unexpected optimal parameters which do not reflect the standard hardware parameters but are rather unexpectedly scaled to match the sequences where gates such as the Hadamard are involved. For further elucidation of this, the next section will go into a thorough analysis and discussion of the obtained results.

6.3 Analysis and Discussion

Apart from the T_2^* sequences, which provided lower fidelity data, all of the experimental procedures proved to attain successful and reliable data which in turn provided valuable insight. The data allowed for very efficient optimisation of hardware parameters, allowing for the probing of these values without direct access to their measurements from a relatively simple theoretical model. This section will focus on the detailed analysis of these results and the numerical accuracy of all the data obtained.

In the case of single-qubit experiments, all of the sequences proved to be highly successful and reliable to extract information, mostly due to the simple forms of the qubit dynamics. These results didn't have any surprising features, as the experimental results had high fidelity and consistency through iterations, while the numerical results were based on a simple form of the GKSL Master Equation which made the computation very quick and easy, especially in the optimisation process which thereby allowed for more iterations to be run and higher accuracy to be achieved. The set of hardware parameters which were extracted was the smallest of all the subsystems, due to the simple Hamiltonian form, which did provide useful insight despite the simplicity. The Hamiltonian parameters extracted, being the qubit frequencies along each Bloch sphere axis $(\omega_x, \omega_y, \omega_z)$, showed that the simplifying assumption given by the backend providers of there only being a z-component is not entirely accurate. This was shown by there being small, but significant, contributions to the qubit frequency along the x- and y-axes, with the vector norm of these being roughly equivalent to the claimed hardware parameter, within $\sim 10\,\text{MHz}$. This would ordinarily not pose any issue for the function of the devices, so the backend claim of the simplified model is effectively correct in most use cases, however this general form should not be ignored as it can prove to be a significant factor in the scalability of larger devices with potential resonance with neighbouring qubits.

In the case of the 2-qubit subsystems, the data showed a similar pattern, in that the simple T_1 sequence provided the most accurate results which gave rise to insightful optimised parameters. These parameters showed once more that the simple effective Hamiltonian claimed by the backend provider does not show the full picture, but rather each qubit has contributions to the frequency from the transverse Bloch sphere axes, and a similar pattern is observed in the qubit coupling parameters which are not the simplified scalar values claimed to act only upon the x- and y- axes, but rather a 3×3 matrix of coupling along all axes. This discrepancy does not pose any significant influence on the relaxation and decoherence dynamics investigated here, but once more should be accounted for in considering the scalability of the quantum devices to avoid unwanted noise from resonances. Significantly, in terms of the temperatures of the devices, which did not have claimed calibration values but rather a general order of magnitude claim, the average photon number of the Markovian dynamics demonstrated that these claims are accurate to within $\pm 10\,\text{mK}$, proving that this method is a viable approach to calibrating the device and individual qubit temperatures. It should be noted, however, that this temperature measure does have the disadvantage of being an inferred value from the photon emission contribution to state decay, and as such does carry inherent inaccuracy compared to a direct measurement.

The T_2 sequence for 2-qubit subsystems demonstrated interesting and well behaved dynamics, including forms of a damped oscillator as well as exponential evolution to equilibrium states, which allowed for a direct demonstration of the Markovianity assumption with a more complicated architecture. This sequence yielded similar results to the T_1 sequences, in terms of the hardware parameters which could be extracted, as they were consistent with expectations as well as the claimed parameters and optimised values from the T_1 sequences. The T_2^* sequences proved to be slightly less reliable due to some off-resonance SPAM error, as discussed before, which would quickly lead to the results deteriorating in most cases and enforce the requirement of multiple attempts at the experiment to obtain accurate results. When these more accurate results were obtained, however, the optimisation process could work with great proficiency and

	Claimed		Experimental		
	ω (GHz)	T_1 (µs)	ω (GHz)	T_1 (µs)	T (mK)
q_0	31.42	100.24	31.42	101.23	47.96
q_1	30.47	106.95	30.47	108.31	54.20
q_2	30.05	101.45	30.05	105.92	50.30

Table 1: Claimed and experimental results for the single-qubit experiments to measure the qubit frequency, ω, relaxation time, T_1, and qubit temperature, T. The q_i labels represent the qubits of the device.

give accurate fits to the experimental data. The hardware parameters which this optimisation led to were not as would be expected by the trends set by previous sequences. Rather, all of the hardware parameters underwent a significant scaling phenomenon, shifting them all away from claimed parameters given by the backend providers. For example, the qubit frequencies underwent a dramatic shift by up to a factor of 2, which is characteristic of the dephasing of the system, while also having average photon number contributions to the decay rates reflecting qubit temperatures on the scale of $\approx 1\,\mathrm{K}$ rather than the expected $\approx 15\,\mathrm{mK}$. Additionally, the actual decoherence time in the form of the decay rate γ was much larger than the claimed parameters, which does not necessarily indicate a successful increase in qubit coherence, but is likely rather a relic of the sequence possessing a more complicated form which would require more careful analysis to extract hardware information.

To assist in the associated difficulties of the T_2^* sequence, the modified sequences of (QC6) and (QC7), representing one qubit undergoing the T_2^* sequence with its neighbour undergoing the T_1 and idle sequences, respectively. These modifications allowed for the damping of the resonant noise of 2 qubits being susceptible to SPAM errors, and provided a more granular look at the qubit dynamics. In the case of (QC7), this problem of resonant external noise remained persistent, though showing a scaled intensity of the errors, reinforcing the suspicion that the H gates in particular are more difficult to implement effectively. In the case of (QC6), however, a new and interesting form of the qubit dynamics was seen, in Figure 12d, which coupled the simple exponential decay of the T_1 sequence with the damped oscillator form of the T_2^* sequence, which allowed for proficient optimisation and extraction of hardware parameters which were consistent with the results from the separate sequences showing that the mixing of these experiments does not produce any phenomena greater than the combination of its parts.

As another example of subsystems combining in a linear and separable manner, the T_1 sequence is worth returning to for a focussed analysis of the predictions made by different subsystems of overlapping qubits. For this case, the single-qubit results for individual neighbouring qubits, which provided very accurate and reliable behaviours, can be compared to the results obtained by 2-qubit subsystems comprising those individual neighbours, as well as separate 2-qubit subsystems which overlap. This analysis goes one step larger to the 3-qubit system as well for an additional comparison point of the predicted hardware parameters and behaviours. For an example of the specifics of this kind of procedure, the first 3 qubits (indexed as 0, 1, and 2) of a 5-qubit system were analysed and optimised to extract parameters which agreed accurately with the claimed values, within a small margin of error which justifies the use of optimisation. Then two sets of 2-qubit subsystems, focussed on qubits 0 & 1 and 1 & 2 respectively, went through the optimisation process to produce values comparable with the single-qubit case as well as the doubly predicted qubit 1 parameters. These 3 qubits comprised the final overall system to investigate the scalability of this method.

The results which this procedure produced, as seen in Tables 1, 2 and 3, were very promising in that the single-qubit results demonstrated excellent accuracy when compared to the experimental data, while having these results replicated by the 2-qubit subsystems which were inter-

	Claimed			Experimental			
	ω (GHz)	T_1 (µs)	J (GHz)	ω (GHz)	T_1 (µs)	J (GHz)	T (mK)
$q_{01,0}$	31.42	100.24	8.31×10^{-3}	31.42	96.49	5.87×10^{-3}	6.62
$q_{01,1}$	30.47	106.95		30.47	109.62		65.55
$q_{12,1}$	30.47	106.95	7.42×10^{-3}	30.47	109.26	5.25×10^{-3}	73.63
$q_{12,2}$	30.05	101.45		30.05	108.31		6.42

Table 2: Claimed and experimental results for the 2-qubit experiments to measure the qubit frequency, ω, relaxation time, T_1, inter-qubit coupling, J, and qubit temperature, T. The $q_{i,j}$ labels represent the 2-qubit pairings, and the specific qubits of the device, respectively.

nally consistent, and finally the 3-qubit system to confirm this accurate extraction. These results not only reflect the findings of the T_1 sequences discussed previously, about the generalised form of the Hamiltonian and more accurate decay parameters, but also confirm the viability of this method to predict larger systems of qubits. This means that multiple 2-qubit systems can be run and analysed, similarly to tomography procedures, and then be used to extract parameters and act as a form of calibration. The 2-qubit results can also be combined through tensor products to obtain a tomography of a larger system which would ordinarily grow exponentially in difficulty.

This method is, however, fairly unreliable as a self-contained single-run tomography procedure which is mostly the fault of the backend rather than the method. The backend is hindered by the amount of traffic it faces with it being a cloud-based open-access service which occasionally leads to queue times lasting longer than several calibrations which occur hourly. This leads to some experiments being run on different calibration profiles and after different reset periods which affect the hardware parameters dictating the qubit dynamics which finally leads to inconsistencies in the extracted optimal data which destroys the integrity of the tomography. Additionally, as the backend is open-access, the attainable information is fairly limited, for example with the device temperatures which would be able to be monitored more efficiently with direct access to the devices. Although this method is meant to be useful especially in such cases to extract information which is not being actively monitored, there is a significant improvement to be made in the feedback from the devices which are ultimately controlled by the backend compilation which provides a larger margin for error between the gate composition and the execution of the quantum circuits.

It is important to note that the explicit inclusion of a pure dephasing contribution to the density operator evolution was considered in additional experiments to quantify its influence. These additional experiments revealed that the presence of pure dephasing was insignificant in the modelling of the qubit systems. This is, however, not enough evidence to suggest that the process of pure dephasing is entirely irrelevant to these quantum devices, rather that it is inconsequential in this method of modelling the qubit evolution and extracting hardware parameters. As such, the quantitative mention of this parameter is omitted from the present discussion.

Despite the difficulties faced in this setting of the experimental process, the data show very promising results for the viability of this as a form of tomography to probe the dynamics of larger systems of connected qubits in NISQ devices. For isolated devices with direct control within a lab this method could provide significant insight into unaccounted for noise sources deteriorating the qubit coherence, and for open-access devices this method can serve as an additional calibration method to obtain the most current hardware parameters for higher precision in the simulation of experiments such as quantum chemistry or open quantum systems.

	Claimed			Experimental			
	ω (GHz)	T_1 (µs)	J (GHz)	ω (GHz)	T_1 (µs)	J (GHz)	T (mK)
q_0	31.42	100.24	8.31×10^{-3}	31.42	98.16	8.31×10^{-3}	50.59
q_1	30.47	106.95	–	30.47	117.77	–	67.92
q_2	30.05	101.45	7.42×10^{-3}	30.05	108.08	7.42×10^{-3}	6.37

Table 3: Claimed and experimental results for the 3-qubit experiments to measure the qubit frequency, ω, relaxation time, T_1, inter-qubit coupling, J, and qubit temperature, T.

7 Conclusion

In this work the fundamentals of several fields of research, such as quantum computing, superconducting qubit hardware, and open quantum systems, were introduced and discussed to lay a foundation for the understanding of the topics and their relevance to each other. This relevance was leveraged into a discussion of the overlap of these topics in the realm of quantum noise and error mitigation, which is covered primarily by current research. The most recent and relevant research in this field was discussed and used to create a map of the current state of investigation in this topic, which showed a gap in research of a simple method to probe hardware parameters of a NISQ open-access cloud-based quantum computing service such as that offered by IBM.

The filling of this research gap was the motive of this project, which provided a simple method of using basic experimental procedures typically used to measure the relaxation and decoherence times, T_1 and T_2, of quantum states, and numerically replicated through a Markovian quantum master equation to measure how well the claimed hardware parameters fit the experimental observations. This process was expanded to use optimisation techniques to improve the agreement between numerical results and experimental data to find more accurate values of the hardware parameters which dictate the dynamics of the system.

This gave rise to interesting phenomena, such as more generalised Hamiltonians containing broader descriptions of qubit frequency and coupling, as well as proving the proficiency of this method to extract all of the hardware parameters without needing to revert to various specialised experiments which measure the parameters individually. The consistency of this method was verified through using various sizes of qubit subsystems which each produced values for hardware parameters for individual qubits, which were congruent to a reliable degree of accuracy that the process could be considered successful.

There are several hindrances which detract from the accuracy of this method, such as the queue system of the quantum devices from their open-access platform as well as the lack of direct control over the compilation of the quantum circuits to executable qubit control. The method is also susceptible to external influences such as stochastic noise and hardware impurities, which are a fault of NISQ devices in general, which also detracts from the reliability in scenarios which require high accuracy. Despite these shortcomings, this method serves as a proof of concept of subsystem Markovian tomography which can be stitched together to provide a mapping of qubit dynamics in larger systems without the exponential growth in difficulty associated with full quantum tomography.

Many more improvements can be made to this method, such as assisting the performance with machine learning methods, and performing more accurate calibration and tomography to mitigate any external errors which are unavoidable in open-access NISQ devices, or finding mechanisms to improve qubit coherence times. This work also opens a new path for further investigation into more generalised models which can uncover finer details which are typically suppressed in approximation, such as qubit frequency vectors and coupling tensors, but could prove crucial in further quantum engineering in the path to fault-tolerance.

A Numerical Algorithms

Throughout the work presented in this thesis, many numerical methods were used. In the main body of this work, the details of these numerical methods was excluded from the discussion for concision of the discourse. The details of these numerical methods is presented in this section of the appendix.

A.1 Adam Optimiser

The Adam optimiser is a method conventionally used in machine learning of deep neural networks, and is powerful because of its adaptive learning rate control. This method makes use of exponentially decaying averages of previous gradients, denoted g_t, as well as exponentially decaying averages of previous squared gradients, g_t^2, which are involved in the following expressions,

$$\begin{aligned} m_t &= \beta_1 m_{t-1} + (1-\beta_1)\, g_t, \\ v_t &= \beta_2 v_{t-1} + (1-\beta_2)\, g_t^2. \end{aligned} \tag{159}$$

The variables m_t and v_t are the mean and uncentred variance (or first and second moments) of the gradients, respectively, and are initialised as empty vectors. The values β_1 and β_2 are decay rates to control the acceleration of the learning rates, however while these values are near unity and the accelerations are small, the bias of the moments being zero slow the entire process. This bias towards staying near zero is corrected for to provide more accurate trajectories by the following bias-corrected estimates,

$$\begin{aligned} \hat{m}_t &= \frac{m_t}{1-\beta_1^t}, \\ \hat{v}_t &= \frac{v_t}{1-\beta_2^t}. \end{aligned} \tag{160}$$

These parameters are then used in the actual gradient descent iterative expression where the set of parameters, $\vec{x}$, is updated according to

$$\vec{x}_{t+1} = \vec{x}_t - \frac{\alpha}{\sqrt{\hat{v}_t} + \epsilon}\hat{m}_t, \tag{161}$$

where α is the initial learning rate, usually set to 0.1 depending on the order of magnitude of parameters involved, and ϵ is a small correction value to avoid dividing by ∞, and is typically set to $\epsilon = 10^{-8}$, while the decay rates are conventionally set to $\beta_1 = 0.8$ and $\beta_2 = 0.999$. This method either calculates for a set number of iterations or until a convergence criterion is met. It has been shown to be very successful in the field of machine learning over other modifications of the gradient descent algorithm. As an example, Figure 13 shows a typical error curve for optimisation with this method.

A.2 Numerical Integration

In the solution of the master equation to obtain the density matrix for each quantum channel, the equation was integrated as an ODE using a function of JAX's SciPy [69] extension which is uses the FORTRAN implementation of the LSODA method [70], which automatically decides between using a non-stiff (Adams) or stiff (BDF) method, starting with the former and monitoring the data dynamically to make the decision to switch.

The Adams method which it uses a multi-step general method, which makes use of past function values, f, in the iterative solution expressed as

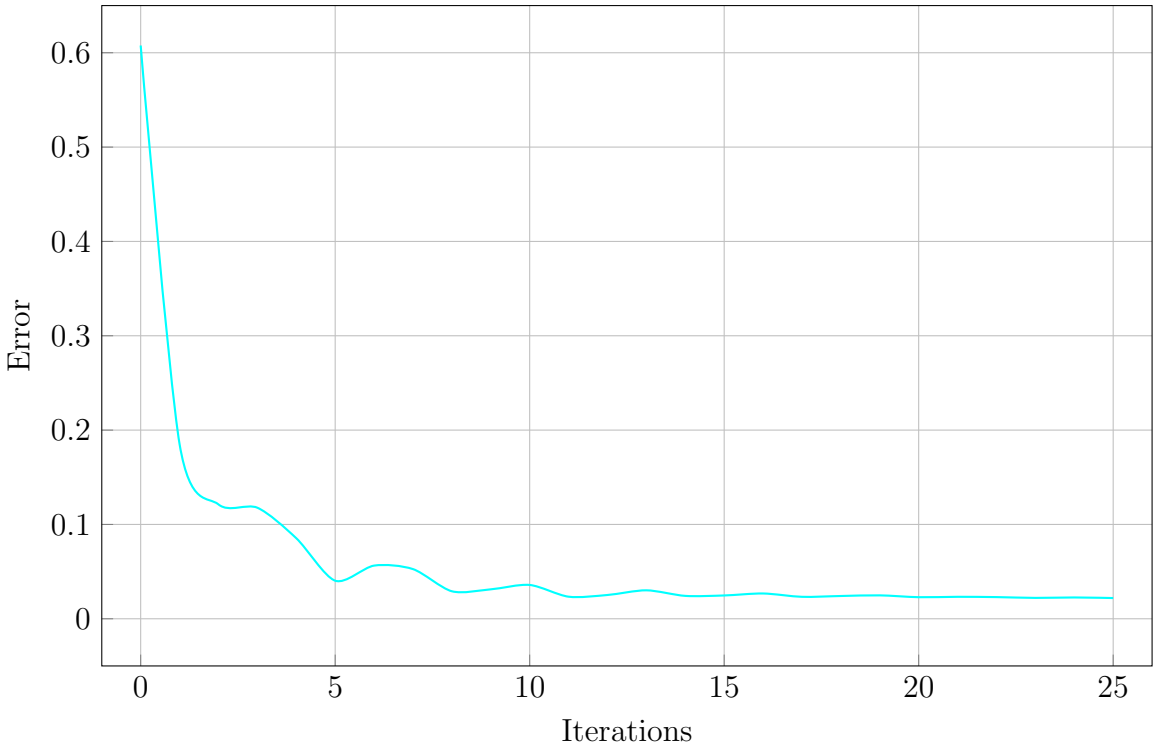

Figure 13: Error curve of the Adam optimiser performing gradient descent to optimise the parameters of a 2-qubit T_1 sequence to minimise the difference between the numerical solution and the experimental data. Parameters used in this optimisation are as follows, $\alpha = 0.1, \beta_1 = 0.8, \beta_1 = 0.999, n_{\text{iterations}} = 25$. The minimum least-squares error obtained in this example was 0.02197117.

$$y_n = y_{n-1} + h \sum_{j=0}^{k} \beta_j f_{n-j}, \tag{162}$$

which is a modification of the Euler method, which is the simplest method in the Runge-Kutta family of numerical integration, requiring the initial values of f and f', being the function point and its first derivative. In the Adams method, every step requires the solution of a non-linear system, for past history terms a_n,

$$y_n = a_n + h\beta_0 f\left(t_n, y_n\right). \tag{163}$$

The Backward Differentiation Formula (BDF) method operates similarly, but makes use of previous derivatives, y_n, to advance the iteration, as

$$y_n = \sum_{i=1}^{k} \alpha_i y_{n-i} + h\beta_0 f_n. \tag{164}$$

The dynamic switching between these methods coupled with the accuracy provided by the Euler method, upon which both are based, the solutions provided by this numerical function are highly accurate as well as providing excellent compatibility with the auto-differentiation and JIT compiler functionalities of JAX, which work well in the optimisation procedure where the parameters of this integration can be iteratively modified to plot a solution landscape for the gradient descent algorithm.

References

[1] G. E. Moore, "Cramming More Components onto Integrated Circuits," *Proceedings of the IEEE* **86** no. 1, (1998) 82–85. 1

[2] R. P. Feynman, "Simulating Physics with Computers," *International Journal of Theoretical Physics* **21** no. 6, (1982) 467–488. 1

[3] D. Deutsch and R. Jozsa, "Rapid Solution of Problems by Quantum Computation," *Proceedings of the Royal Society of London* **439** no. 1907, (1992) 553–558. 1

[4] P. Shor, "Algorithms for Quantum Computation: Discrete Logarithms and Factoring," in *Proceedings 35th annual symposium on foundations of computer science*, pp. 124–134. Institute of Electrical and Electronics Engineers (IEEE), Dec., 2002.

[5] L. K. Grover, "A Fast Quantum Mechanical Algorithm for Database Search," in *Proceedings of the twenty-eighth annual ACM symposium on theory of computing*, pp. 212–219. 1996.

[6] I. M. Georgescu, S. Ashhab, and F. Nori, "Quantum Simulation," *Reviews of Modern Physics* **86** (Mar., 2014) 153.

[7] J. Biamonte *et al.*, "Quantum Machine Learning," *Nature* **549** (Sept., 2017) 195–202. 1

[8] J. Preskill, "Quantum Computing in the NISQ Era and Beyond," *Quantum* **2** (Aug., 2018) 79. 1

[9] P. Krantz *et al.*, "A Quantum Engineer's Guide to Superconducting Qubits," *Applied Physics Reviews* **6** (June, 2019) 021318. 7, 8, 10

[10] H.-L. Huang, D. Wu, D. Fan, and X. Zhu, "Superconducting Quantum Computing: A Review," *Science China Information Sciences* **63** no. 8, (2020) 1–32. 7

[11] N. A. Kudryashov, "The generalized Duffing oscillator," *Communications in Nonlinear Science and Numerical Simulation* **93** (2021) 105526. 9

[12] Y. Y. Gao, M. A. Rol, S. Touzard, and C. Wang, "Practical Guide for Building Superconducting Quantum Devices," *PRX Quantum* **2** no. 4, (2021) 040202.

[13] J. M. Gambetta, J. M. Chow, and M. Steffen, "Building Logical Qubits in a Superconducting Quantum Computing System," *npj Quantum Information* **3** (Dec., 2017) 1–7. 10, 42

[14] A. Asfaw *et al.*, "Learn Quantum Computation Using Qiskit," 2020. `http://community.qiskit.org/textbook`. 11

[15] H.-P. Breuer and F. Petruccione, *The Theory of Open Quantum Systems*. Oxford University Press, 2007. 14, 16, 18

[16] K. Kraus, A. Böhm, J. D. Dollard, and W. H. Wootters, *States, Effects, and Operations Fundamental Notions of Quantum Theory*. Springer Berlin Heidelberg, 1983. 15, 26

[17] V. Gorini, A. Kossakowski, and E. C. Sudarshan, "Completely Positive Dynamical Semigroups of N-level Systems," *Journal of Mathematical Physics* **17** (1975) 821–825. 19

[18] G. Lindblad, "On the Generators of Quantum Dynamical Semigroups," *Communications in Mathematical Physics* **48** no. 2, (1976) 119–130. 19

[19] A. G. Redfield, "On the theory of relaxation processes," *IBM Journal of Research and Development* **1** no. 1, (1957) 19–31. 25

[20] C. Cohen-Tannoudji, J. Dupont-Roc, and G. Grynberg, *Atom-photon Interactions: Basic Processes and Applications*. VCH PUBN, Mar., 1998. 25

[21] M. A. Nielsen and I. A. Chuang, *Quantum Computing and Quantum Information*. Cambridge University Press, 10th Anniversary ed., 2010. 26

[22] L. Tian, S. Lloyd, and T. P. Orlando, "Decoherence and Relaxation of a Superconducting Quantum Bit during Measurement," *Physical Review B* **65** (2002) 1–7. 27

[23] A. Y. Smirnov, "Decoherence and Relaxation of a Quantum Bit in the Presence of Rabi Oscillations," *Physical Review B* **67** (Apr., 2003) 155104. 28

[24] I. I. Rabi, "Space Quantization in a Gyrating Magnetic Field," *Physical Review* **51** no. 8, (1937) 652–654. 28

[25] F. Bloch, "Generalized Theory of Relaxation," *Physical Review* **105** no. 4, (Feb., 1957) 1206–1222. 28

[26] P. V. Klimov *et al.*, "Fluctuations of Energy-relaxation Times in Superconducting Qubits," *Physical Review Letters* **121** (Aug., 2018) 090502. 29, 30

[27] S. Schlör *et al.*, "Correlating Decoherence in Transmon Qubits: Low Frequency Noise by Single Fluctuators," *Physical Review Letters* **123** (Nov., 2019) 190502. 29

[28] J. J. Burnett *et al.*, "Decoherence Benchmarking of Superconducting Qubits," *npj Quantum Information* **5** (Dec., 2019) 1–8. 30

[29] M. Carroll *et al.*, "Dynamics of Superconducting Qubit Relaxation Times," `arXiv:2105.15201`. 31

[30] N. B. Delone and V. P. Krainov, "AC Stark Shift of Atomic Energy Levels," *Physics-Uspekhi* **42** no. 7, (July, 1999) 669–687. 31

[31] D. I. Schuster *et al.*, "AC Stark Shift and Dephasing of a Superconducting Qubit Strongly Coupled to a Cavity Field," *Physical Review Letters* **94** (Apr., 2005) 123602. 31

[32] A. Schneider *et al.*, "Local Sensing with the Multilevel AC Stark Effect," *Physical Review A* **97** (June, 2018) 062334. 31

[33] E. Magesan and J. M. Gambetta, "Effective Hamiltonian Models of the Cross-resonance Gate," *Physical Review A* **101** (May, 2020) 052308. 31, 42

[34] S. E. de Graaf *et al.*, "Two-level Systems in Superconducting Quantum Devices Due to Trapped Quasiparticles," *Science Advances* **6** (2020) 5055–5073. 32

[35] A. P. Vepsäläinen *et al.*, "Impact of Ionizing Radiation on Superconducting Qubit Coherence," *Nature* **584** (Aug., 2020) 551–556. 32

[36] C. Müller, J. H. Cole, and J. Lisenfeld, "Towards Understanding Two-level-systems in Amorphous Solids: Insights from Quantum Circuits," *Reports on Progress in Physics* **82** no. 12, (2019) 124501. 33

[37] C. R. H. McRae *et al.*, "Materials Loss Measurements Using Superconducting Microwave Resonators," *Review of Scientific Instruments* **91** (Sept., 2020) 091101. 33

[38] M. Mohseni, A. T. Rezakhani, and D. A. Lidar, "Quantum-process Tomography: Resource Analysis of Different Strategies," *Physical Review A* **77** no. 3, (Mar., 2008) 032322. 33

[39] S. T. Merkel *et al.*, "Self-consistent Quantum Process Tomography," *Physical Review A* **87** (June, 2013) 6. 34

[40] A. M. Brańczyk *et al.*, "Self-calibrating Quantum State Tomography," *New Journal of Physics* **14** no. 8, (2012) 085003. 35

[41] V. V. Dobrovitski, G. de Lange, D. Ristè, and R. Hanson, "Bootstrap Tomography of the Pulses for Quantum Control," *Physical Review Letters* **105** (2010) 077601. 35

[42] Y. Chen, M. Farahzad, S. Yoo, and T. C. Wei, "Detector Tomography on IBM Quantum Computers and Mitigation of an Imperfect Measurement," *Physical Review A* **100** (Nov., 2019) 052315. 35

[43] J. Fiurášek, "Maximum-likelihood Estimation of Quantum Measurement," *Physical Review A* **64** (July, 2001) 024102. 35

[44] F. B. Maciejewski, Z. Zimborás, and M. Oszmaniec, "Mitigation of Readout Noise in Near-term Quantum Devices by Classical Post-processing Based on Detector Tomography," *Quantum* **4** (Apr., 2020) 257. 36

[45] A. Kandala *et al.*, "Error Mitigation Extends the Computational Reach of a Noisy Quantum Processor," *Nature* **567** (Mar., 2019) 491–495. 36

[46] A. M. Palmieri *et al.*, "Experimental Neural Network Enhanced Quantum Tomography," *npj Quantum Information* **6** (Dec., 2020) 1–5. 37

[47] Y. Baum *et al.*, "Experimental Deep Reinforcement Learning for Error-robust Gate-set Design on a Superconducting Quantum Computer," *PRX Quantum* **2** no. 4, (2021) 040324. 37

[48] T. Alexander *et al.*, "Qiskit Pulse: Programming Quantum Computers through the Cloud with Pulses," *Quantum Science and Technology* **5** no. 4, (Aug., 2020) 044006. 37

[49] G. O. Samach *et al.*, "Lindblad Tomography of a Superconducting Quantum Processor," `arXiv:2105.02338`. 38, 42

[50] Ángel Rivas, S. F. Huelga, and M. B. Plenio, "Quantum Non-markovianity: Characterization, Quantification and Detection," *Reports on Progress in Physics* **77** (Sept., 2014) 094001. 39

[51] H. P. Breuer, E. M. Laine, J. Piilo, and B. Vacchini, "Colloquium: Non-markovian Dynamics in Open Quantum Systems," *Reviews of Modern Physics* **88** (Apr., 2016) 021002. 39

[52] J. Cerrillo and J. Cao, "Non-markovian Dynamical Maps: Numerical Processing of Open Quantum Trajectories," *Physical Review Letters* **112** (Mar., 2014) 110401. 39

[53] S. Nakajima, "On Quantum Theory of Transport Phenomena: Steady Diffusion," *Progress of Theoretical Physics* **20** no. 6, (1958) 948–959. 39

[54] R. Zwanzig, "Ensemble Method in the Theory of Irreversibility," *The Journal of Chemical Physics* **33** no. 5, (1960) 1338–1341. 39

[55] Y. Q. Chen *et al.*, "Non-markovian Noise Characterization with the Transfer Tensor Method," *Physical Review Applied* **13** (Feb., 2020) 034045. 40

[56] F. A. Pollock, C. Rodríguez-Rosario, T. Frauenheim, M. Paternostro, and K. Modi, "Non-markovian Quantum Processes: Complete Framework and Efficient Characterization," *Physical Review A* **97** (Jan., 2018) 012127. 40

[57] F. A. Pollock, C. Rodríguez-Rosario, T. Frauenheim, M. Paternostro, and K. Modi, "Operational Markov Condition for Quantum Processes," *Physical Review Letters* **120** (Jan., 2018) 040405. 40

[58] G. A. White, C. D. Hill, F. A. Pollock, L. C. Hollenberg, and K. Modi, "Demonstration of Non-markovian Process Characterisation and Control on a Quantum Processor," *Nature Communications* **11** (Dec., 2020) 1–10. 41

[59] G. A. White, C. D. Hill, F. A. Pollock, L. C. Hollenberg, and K. Modi, "Diagnosing Temporal Quantum Correlations: Compressed Non-markovian Calipers," arXiv:2107.13934. 41

[60] G. A. White, C. D. Hill, F. A. Pollock, L. C. Hollenberg, and K. Modi, "Non-markovian Quantum Process Tomography," arXiv:2106.11722. 41

[61] IBM Quantum, 2021. 42

[62] J. Gambetta *et al.*, "Qiskit: An Open-source Framework for Quantum Computing," Apr., 2022. 42

[63] G. García-Pérez, M. A. Rossi, and S. Maniscalco, "IBM Q Experience As a Versatile Experimental Testbed for Simulating Open Quantum Systems," *npj Quantum Information* **6** (Dec., 2020) 1–10. 42

[64] E. L. Hahn, "Spin Echoes," *Physical Review* **80** (Nov., 1950) 580–594. 45

[65] D. P. Kingma and J. Ba, "Adam: A Method for Stochastic Optimization," arXiv:1412.6980. 48

[66] B. Misra and E. C. G. Sudarshan, "The Zeno's paradox in quantum theory," *Journal of Mathematical Physics* **18** no. 4, (1977) 756–763. 49

[67] J. Bradbury *et al.*, "JAX: Composable transformations of Python+NumPy programs," 2018. http://github.com/google/jax. 51

[68] R. Frostig, M. J. Johnson, and C. Leary, "Compiling Machine Learning Programs Via High-level Tracing," *Systems for Machine Learning* (2018) 23–24. 51

[69] P. Virtanen *et al.*, "SciPy 1.0: Fundamental Algorithms for Scientific Computing in Python," *Nature Methods* **17** no. 3, (2020) 261–272. 61

[70] L. Petzold, "Automatic Selection of Methods for Solving Stiff and Nonstiff Systems of Ordinary Differential Equations," *SIAM Journal on Scientific and Statistical Computing* **4** no. 1, (1983) 136–148. 61